Photoelectron Spectroscopy at a Free–Electron Laser:
Investigation of Space–Charge Effects in Angle–Resolved and Core–Level Spectroscopy
and
Realization of a Time–Resolved Core–Level Photoemission Experiment

Dissertation
zur Erlangung des Doktorgrades
der Mathematisch-Naturwissenschaftlichen Fakultät
der Christian-Albrechts-Universität
zu Kiel

vorgelegt von

Martin Marczynski–Bühlow

Kiel 2011

Referent/in: Prof. Dr. L. Kipp

Korreferent/in: Prof. Dr. M. Bauer

Tag der mündlichen Prüfung: 30.01.2012

Zum Druck genehmigt: Kiel, den 30.01.2012

Prof. Dr. L. Kipp
Der Dekan

To So-Nyeo

Zusammenfassung

Der Freie–Elektronen–Laser (FEL) in Hamburg (FLASH) stellt mit seinen herausragenden Eigenschaften bezüglich Photonenpulsintensität (bis zu 100 μJ pro Puls), erreichbaren Photonenenergiebereichs (30 eV bis 1500 eV), seiner transversalen Kohärenz sowie kurzer Pulsdauern (einige zehn Femtosekunden) eine sehr interessante Lichtquelle für die Photoelektronenspektroskopie (PES) dar. Insbesondere Element–spezifische sowie zeitaufgelöste PES tiefer liegender Rumpfniveaus ist nun mit den hohen Photonenenergien bei akzeptabler Pulsintensität möglich.

In dieser Arbeit wurden unterschiedliche experimentelle Setups aufgebaut, um winkelaufgelöste PES (ARPES), Rumpfniveau–Spektroskopie (XPS) sowie zeitaufgelöste PES (TR-PES) Experimente an der Monochromator–Beamline PG2 am FLASH zu realisieren. Diese werden in dieser Arbeit dargestellt und deren Funktion gezeigt. Existierende sowie neu–entwickelte Systeme für das Online–Aufzeichnen der FEL–Pulseintensitäten und das Generieren eines räumlichen und zeitlichen Überlapps der FEL–Strahlung mit einem optischen Laser für zeitaufgelöste Experimente sind erfolgreich in die PES–Experimente integriert worden.

Weiterhin wurden in dieser Arbeit für das Verständnis von auftretenden Raumladungseffekten (SCE) in der PES bei der Verwendung von gepulsten Photonenquellen mit hohen Pulsintensitäten, die sich in energetischen Verbreiterungen und Verschiebungen im Photoemissionsspektrum widerspiegeln, mit Hilfe einer molekular–dynamischen N–Teilchen Simulation auf der Basis eines modifizierten "Treecode"–Algorithmus durchgeführt. Mit Hilfe dieses Algorithmus konnten die Simulationen ausreichend schnell und genau durchgeführt werden. Es stellte sich heraus, dass der einflussreichste Parameter für die Raumladungseffekte die "lineare Elektronendichte" – das Verhältnis von Anzahl der Photoelektronen zum Spotdurchmesser auf der Probe – ist. Desweiteren konnten die Simulationen die Beobachtungen aus in der Literatur beschrieben Experimenten gut wiedergeben, und ein paar Daumenregeln für zukünftige ARPES– und XPS–Experimente wurden abgeleitet.

Experimentell wurden in dieser Arbeit Raumladungseffekte bei ARPES sowie bei XPS als Funktion der FEL–Pulsintensität untersucht. Es stellte sich heraus, dass ARPES im Prinzip am FLASH möglich ist. Steigende Photoelektronendichten führten zu zunehmenden energetischen Verschiebungen und Verbreiterungen im Spektrum bis in den Bereich einiger Elektronenvolt. Intensitätsabhängige XPS an $1T$–TaS$_2$ konnte mit Hilfe von Simulationen mit dem Treecode–Algorithmus sehr gut reproduziert werden und ein linearer Zusammenhang der energetischen Verschiebungen und Verbreiterungen in Abhängigkeit zur Elektronenzahl gefunden werden. Dreieckig–strukturierte Strahlenschäden (entsprechend der krystallinen Struktur) wurden in den $1T$–TiTe$_2$–Proben nur unter Verwendung höchster Pulsintensitäten beobachtet.

Schließlich werden die ersten zeitaufgelösten Messungen der Ta4f–Rumpfniveaus von $1T$–TaS$_2$ in der isolierneden Ladungsdichtewellenphase präsentiert bei einer – für höhere harmonische Quellen – relativ hohen Photonenenergie von $\approx$ 175 eV. Eine zeitaufgelöste Entwicklung der niederenergetischen Ta4f–Kante konnte beobachtet werden. Dieser Effekt wurde mit großer Sicherheit Raumladungseffekten – hervorgerufen durch schwankende FEL–Intensitäten – zugeordnet. Nichtsdestotrotz konnte mit dem gleichen Aufbau von unserer Arbeitsgruppe bei Wiederholung des Experimentes bei signifikant besserer Zeitauflösung direkt die Ladungsordnungsdynamiken in dem komplexen Material $1T$–TaS$_2$ beobachtet werden.

Abstract

The free–electron laser (FEL) in Hamburg (FLASH) is a very interesting light source with which to perform photoelectron spectroscopy (PES) experiments. Its special characteristics include highly intense photon pulses (up to 100 J/pulse), a photon energy range of 30 eV to 1500 eV, transverse coherence as well as pulse durations of some ten femtoseconds. Especially in terms of time–resolved PES (TRPES), the deeper lying core levels can be reached with photon energies up to 1500 eV with acceptable intensity now and, therefore, element–specific, time–resolved core–level PES (XPS) is feasible at FLASH.

During the work of this thesis various experimental setups were constructed in order to realize angle–resolved (ARPES), core–level (XPS) as well as time–resolved PES experiments at the plane grating monochromator beamline PG2 at FLASH. Existing as well as newly developed systems for online monitoring of FEL pulse intensities and generating spatial and temporal overlap of FEL and optical laser pulses for time–resolved experiments are successfully integrated into the experimental setup for PES.

In order to understand space–charge effects (SCEs) in PES and, therefore, being able to handle those effects in future experiments using highly intense and pulsed photon sources, the origin of energetic broadenings and shifts in photoelectron spectra are studied by means of a molecular dynamic N–body simulation using a modified Treecode Algorithm for sufficiently fast and accurate calculations. It turned out that the most influencing parameter is the "linear electron density" – the ratio of the number of photoelectrons to the diameter of the illuminated spot on the sample. Furthermore, the simulations could reproduce the observations described in the literature fairly well. Some rules of thumb for XPS and ARPES measurements could be deduced from the simulations.

Experimentally, SCEs are investigated by means of ARPES as well as XPS measurements as a function of FEL pulse intensities using the transition metal dichalcogenides $1T$–$\mathrm{TiTe_2}$ and $1T$–$\mathrm{TaS_2}$ as reference systems. ARPES at FLASH is in principle feasible below the SCE limit and triangular structured radiation damages (in accordance with the crystal structure) occured only at highest FEL pulse intensities not usable for PES. With increasing photoelectron densities, increasing energetic shifts and broadenings in the range of several eV were observed. Intensity dependent XPS measurements on $1T$–$\mathrm{TaS_2}$ could be reproduced by the simulations with the Treecode Algorithm and a linear behavior of the energetic shift and broadening as a function of the electron number was found.

Finally, the results of first time–resolved XPS measurements on the Ta$4f$ core levels of $1T$–$\mathrm{TaS_2}$ in the CDW–insulating phase using a – in comparison with HHG sources – high photon energy of $\approx$ 175 eV are presented for the first time. A time–dependent evolution of the low binding energy edge of the Ta$4f$ core levels was observed. This effect could almost certainly be attributed to varying FEL intensities indicating that induced SCEs interfere with possible physical effects. However, with the same setup, our research group repeated the experiment with significantly better temporal resolution and succeeded in measuring directly the charge order dynamics in the complex material $1T$–$\mathrm{TaS_2}$ with a temporal resolution of 700 fs and atomic–site sensitivity for the first time.

Contents

1 Introduction

Angle–resolved-photoelectron spectroscopy (ARPES) is the most powerful method in order to investigate the occupied and momentum–resolved electronic structure of solids [1]. Here, monochromatic light in the UV to X–ray regime is illuminated onto the sample under investigation. With a distinct probability an incident photon is absorbed and an electron, the so–called photoelectron, is emitted from the sample surface. This electron is typically analyzed via a special electron analyzer with respect to its kinetic energy and emission angle. During the PES experiment the photocurrent is measured as a function of emission angle and kinetic energy imaging the occupied valence band structure $E(\vec{k})$, including the Fermi surface $E(\vec{k}) = E_F$ and characteristical signs for electron correlation effects such as band gaps due to phase transitions to superconductivity or the generation of charge–density waves. Furthermore, lineshape analysis of photoelectron spectra can deliver insight into many–body effects in the solid.

Especially, in combination with modern synchrotron radiation sources, delivering highly brilliant and narrow–band photon pulses with continuously tunable photon energies from the VUV to X–ray regime, ARPES allows to measure the electronic structure with very high precision.

Ultra fast processes such as chemical reactions at surfaces, induced phase transitions in correlated materials, catalytical processes and spin dynamics [2–5] can not be studied via conventional PES measuring the electronic structure in quasi–equilibrium. These processes typically take place on a femtosecond to picosecond time scale and, thus, one needs pulsed photon sources with pulse durations shorter than the dynamical process under investigation in order to measure these. Therefore, modern synchrotron radiation sources of the third generation, delivering photon pulses with pulse lengths of some 10 picoseconds are not able to measure those processes. In the 1980s, the development of Ti:Sapphire laser systems with pulse durations of some femtoseconds opened the field of time–resolved experiments and the investigation of ultrashort processes in the femtosecond regime. With the generation of higher harmonics [6–9] of the fundamental Ti:Sapphire wavelength, photon energies of several 10 eV with acceptable intensities can be reached and, thus, time–resolved PES (TRPES) of valence bands and partly of core levels with lowest binding energies is possible using a pump–probe technique. Within this pump–probe TRPES experiment, two photon pulses are used. One pulse excites the electronic system of the sample (pump pulse), while with the second pulse (probe pulse) the electronic system is probed as a function of temporal delay.

With the installation of the free–electron laser (FEL) in Hamburg (FLASH) [10–12], both, the advantage of modern synchrotron radiation sources with its continuously tunable photon energy in the VUV to X–ray regime as well as the advantages of a pulsed laser system with its ultra–short and coherent photon pulses, are combined in one photon source. Delivering highly intense (10–100 μJ/pulse), ultra short (10–70 fs) photon pulses ($h\nu$ = 30 to 300 eV of the fundamental mode) with nearly total transverse coherence, FLASH opens the path for studying physics, which were not possible with conventional radiation sources since then. Beside time–resolved experiments, the short wavelength, high intensities and coherence of the photon pulses make it possible to image tiny structures via diffraction experiments with one single shot [13, 14]. Furthermore, matter can be studied under extreme conditions due to the creation of high pressures and temperatures at surfaces, clusters, molecules or even atoms [15–18].

In terms of TRPES, the deeper lying core levels can be reached with photon energies up to 1500 eV (fifth harmonic) with acceptable intensity and, therefore, element–specific, time–resolved core–level PES (XPS) is feasible at FLASH. Furthermore, taking advantage of the outstanding peak brilliance and, thus, highly intense photon pulses, in combination with their transverse coherence, focusing the radiation down to the nano–scale by using diffraction optics like Fresnel zone plates [19] or photon sieves [20,21] delivers the possibility to perform spatially and angle–resolved PES. This will be essential in order to investigate surfaces with non periodical nano–structures interesting for micro/nano electronics. In a final stage, one can imagine an experiment were temporal resolution and spatially resolved ARPES are connected.
Though, the pulse characteristics of FLASH seem to be ideal for those PES experiments, several challenges have to be met first. These challenges have their origin on the one hand in FEL machine specific parameters, i.e., intensity (several orders of magnitude) as well as photon energy (1 % of the fundamental photon energy) and temporal ($\approx$ 500 fs) fluctuations from pulse to pulse, and on the other hand in the high photon pulse intensities resulting in the emission of a huge amount of photoelectrons influencing each other due to mutual Coulomb interactions. These interactions induce spectral shifts and broadening in the measured photoemission spectra and are known and often reported in the literature as space–charge effects (SCEs) [22–25].

The goal of this thesis was to establish PES at FLASH and being able to control its parameter. For this, different experimental setups have been built up in order to monitor and, therefore, control the mentioned parameters and to realize ARPES, core–level PES (XPS) as well as core–level TRPES (TRXPS). For photon pulse intensity measurements, two existing online monitoring systems, the gas–monitor detector (GMD) and the multi–channel plate (MCP) detector, were integrated into a typical PES setup. In addition to this, an own device for intensity measurements, the intensity tube (I–tube), was developed promising to be more precisely and universally applicable then the others. Furthermore, an equipment for TRXPS was developed and built up in close collaboration with the research group from Wurth *et al.* from the University in Hamburg. The Wurth group delivered the main experimental PES chamber and a so–called ”timing–tool” being able to measure the temporal as well as spatial overlap of FEL and pump laser pulse on the sample surface. A system for the collinear injection of the laser pulses into the trajectory of the FEL beam is one focus of this thesis.
Due to the importance of understanding SCEs in PES experiments using highly intense and short pulsed photon sources such as FLASH or even laser sources in the laboratory, an other focus of this thesis was to investigate their influence on the measured photoelectron spectra in order to give the researcher an orientation at which pulse parameters the spectral changes might exceed the experimental energy or angular resolution. To achieve this, a self–consistent N–body simulation based on the Barnes & Hut Treecode Algorithm [26], originally developed for gravitational N–body problems (stellar motions), was modified and tested. With this simulation program, the influence of all PES relevant parameters (number of emitted electrons, photon pulse length, spotsize, electron energy distribution, etc.) was investigated on a broad range, three chosen examples from the literature dealing with observed SCEs in PES using FLASH, an femtosecond–laboratory laser system and a modern synchrotron radiation source are compared to our simulations and, finally, our simulations are used to test two analytical models describing SCEs.

The experimental aspect of this thesis consists of two parts. In the first part, the fundamental question was investigated if PES at FLASH is generally feasible. For this, the transition metal dichalcogenide (TMDC) $1T$–$\mathrm{TiTe_2}$ was exposed to different maximum pulse energies and analyzed with regard to sample destructions afterwards. An approximation of a suddenly increasing surface temperature as a function of photon pulse energy is given and the heat dissipation in the crystal is followed in order to explain observed sample destruction at highest intensities. Furthermore, first ARPES measurements on the valence band structure of $1T$–$\mathrm{TiTe_2}$ as well as core–level PES on the Ta$4f$ levels of $1T$–$\mathrm{TaS_2}$ as a function of pulse intensity are performed. The core–level measurements are compared with simulations with the modified Treecode Algorithm in order to further test the applicability of the simulations to PES experiments at FLASH and to give a possibility to deal with occurring SCEs in PES. In the second part, the setup for TRPES was tested on the system $1T$–$\mathrm{TaS_2}$ in the charge–density wave (CDW) insulating phase. It was the first time that TRXPS was performed with such high photon energy (h$\nu \approx 175$ eV), typically not reachable with higher harmonic laser systems with regard to sufficient pulse intensities.

The outline of this thesis is as follows. In chapter 2 the basics of PES and TRPES are briefly described, followed by an introduction of TMDCs $1T$–$\mathrm{TiTe_2}$ and $1T$–$\mathrm{TaS_2}$ in chapter 3. The working principle of FELs and, particularly, the layout and parameters of FLASH, the plane grating monochromator beamline PG2, where the PES experiments were carried out, and the laser system for time–resolved pump–probe experiments is presented in chapter 4. An overview of existing and self–developed instrumentation for intensity dependent or time–resolved PES experiments is given in chapter 5 as well as their integration into three different experimental setups for ARPES, XPS and TRPES at FLASH. In chapter 6 the modified Treecode Algorithm for simulating SCEs is introduced, the influence of the different relevant parameters on the photoelectron spectra is analyzed and a comparison with examples from the literature as well as analytical models is presented. The question of sample destruction due to intense photon pulses is followed in chapter 7. Furthermore, the first ARPES test measurements at varying pulse intensities are presented, SCEs in XPS are studied and compared with own SCE simulations with the introduced simulation algorithm. Finally, in chapter 8 the first results of TRXPS with the newly developed setup is shown.
All experiments presented in this thesis were performed at beamline PG2 of FLASH at the Deutsche Elektronen–Synchrotron (DESY) in Hamburg (Germany).

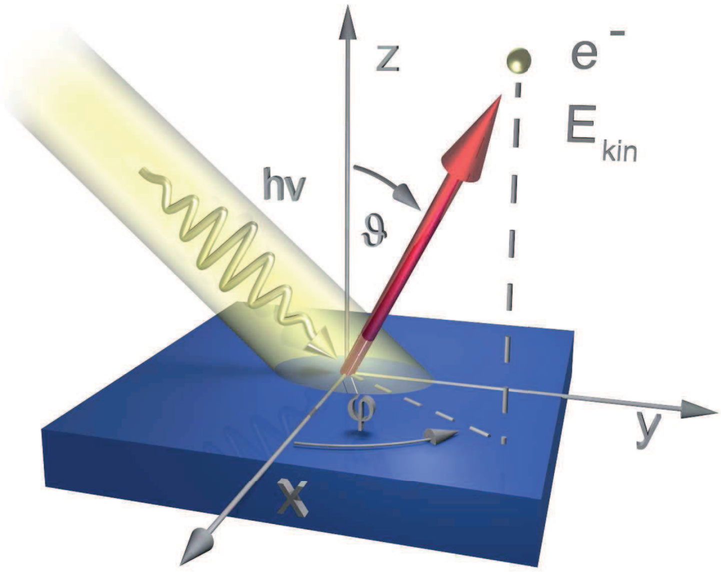

Figure 2.1: Illustration of the photoemission experiment (from [27]): a photoelectron with the kinetic energy E$_{kin}$ is created by absorption of an incident photon with the excitation energy hν. ϕ and ϑ denote the azimuthal and the polar angle of the emitting electron in the sample geometry, respectively.

2 Photoelectron Spectroscopy

Photoelectron spectroscopy (PES) plays an important role in the examination of the electronic structure of solids [1]. By measuring the electron binding energies in the solid with PES, one gets insight into the chemical composition of surfaces (ESCA: Electron Spectroscopy for Chemical Analysis) and the structural orientation of adsorbates. Furthermore, angle–resolved PES (ARPES) serves for the determination of the occupied electronic band structure E($\vec{k}$), including the Fermi surface E($\vec{k}$)=E$_F$ by measuring the emission angle in addition to the binding energy.

The discovery of the outer photoelectric effect and its photon energy dependence by Hertz and Hallwachs can be seen as the historical beginning of PES [28, 29]. Twenty years later, Einstein gave an explanation for the photoelectric effect and established the concept of photons [30]. Planck explained that the photon energy linearly depends on the frequency of the light. And Einstein showed that the energy of a photon must be at least as large as the work function of a solid in order to emit an electron. The kinetic energy of this photoemitted electron can be determined by

$$E_{kin} = h\nu - E_B - \Phi_W \qquad . \tag{2.1}$$

Here, h stands for the Planck's constant, ν for the frequency of the photon, E_B for the binding energy of the electron and Φ_W for the work function of the solid.

Using equation 2.1 the binding energy of an electron can be determined. Characteristical peaks in the photoemission spectrum provide, e.g., information about the chemical composition of the material. However, if the electronic structure such as, e.g., the electronic band structure is of major interest, additionally the momentum of the electron has to be taken into account. This can be measured with ARPES, the two electron emission angles φ (azimuthal angle) and ϑ (polar angle with respect to the surface normal) are measured as well as the kinetic energy of the photoelectrons. The measured photo current I of emitted photoelectrons is given by:

$$I = I(E_{kin}, h\nu, \phi, \vartheta) \quad . \tag{2.2}$$

2.1 Theoretical aspects of ARPES

For the better understanding of a photoemission experiment, it is necessary to follow the process from excitation to emission of an electron in more detail:
Modern theories are describing the direct photoemission process by means of many–body theories and take the whole N–electron system under specific assumptions and boundary conditions into account [31]. In these considerations, a focus lies on the transition of an N–electron system into an (N-1)–electron system during the photoemission process. This transition, including the absorption of a photon and the emission of an electron, is treated as one single event and, therefore, is generally called the "one–step–model".

A more convenient and simpler description of the photoemission process is the so called "three–step–model" [32, 33]. In contrast to the one–step–model, the photoemission process

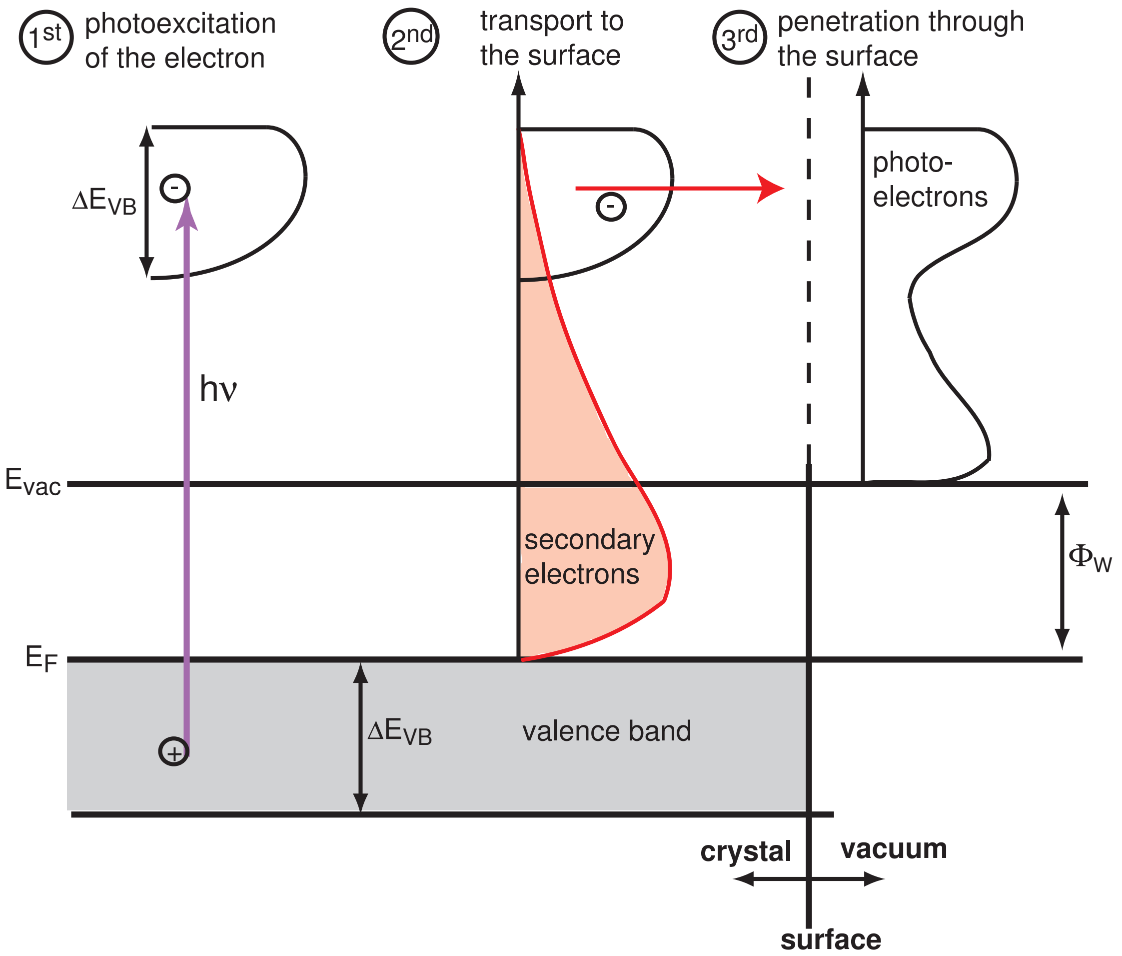

Figure 2.2: Illustration of the photoemission process within the "three–step–model" (after [1]): In the first step, incident photons excite electrons in the solid. In the second step, the electrons travel to the surface and are inelastically scattered producing secondary electrons. In the third step, the electrons penetrate the surface and escape into the vacuum.

consists of three independent sub processes (see Fig. 2.2):

- (i) the excitation of the electron by one photon,
- (ii) the propagation of the excited electron towards the surface of the solid,
- (iii) the transition of the excited electron from the solid surface into the vacuum.

(i) In the "excitation step", the photoemission process can be quantum mechanically described in the following way:
One electron with the mass m_e and momentum operator $\vec{p}$ is bound to the periodic potential of the solid V. The electron is not interacting with other electrons in the solid. The Hamiltonian operator H_0 in the one–particle–approximation is

$$H_0 = \frac{\vec{p}^2}{2m_e} + V \qquad . \tag{2.3}$$

An incident electromagnetic wave is characterized by its energy $h\nu$ and its vector potential $\vec{A}$. The electromagnetic wave interacts with the electron in the solid. This interaction is considered by the transition of the momentum $\vec{p}$ to the generalized momentum $\vec{P}$:

$$\vec{P} = \vec{p} - \frac{e}{c}\vec{A} \qquad . \tag{2.4}$$

Here, e and c denote the charge of an electron and the velocity of light, respectively.
Applying this generalization with a gauge of the scalar potential $\Phi = 0$, the Hamiltonian operator of an electron in a periodic potential interacting with an electromagnetic wave is:

$$H = \frac{1}{2m_e}(\vec{p} - \frac{e}{c}\vec{A})^2 + V \qquad . \tag{2.5}$$

Within the dipole approximation ($\vec{\nabla} \cdot \vec{A} = 0$), the electromagnetic field is approximated as invariant to translations, because the electromagnetic wave is large against the dimension of the unit cell. In general, two–photon processes can be neglected ($\vec{A} \cdot \vec{A} \approx 0$). Finally, the Hamiltonian operator in this approximation can be described by:

$$H = H_0 + H_i = H_0 - \frac{e}{m_e c}\vec{A} \cdot \vec{p} \qquad , \tag{2.6}$$

with the interaction term H_i.
The transition probability ω_{if} per unit time of an electron from the initial state ψ_i to the final state ψ_f can be determined using "Fermi's golden rule" of the time–dependent perturbation theory:

$$\omega_{if} = \frac{1}{h} \cdot |\langle\psi_f|H_i|\psi_i\rangle|^2 \cdot \delta(E_f(\vec{k}_f) - E_i(\vec{k}_i) - h\nu) \; . \tag{2.7}$$

Here, the delta function guarantees the energy conservation $E_f = E_i + h\nu$, where E_f and E_i are the final and initial state energies and $\vec{k}_f$ and $\vec{k}_i$ are the corresponding final and initial state wave vectors. Finally, the photo current in the photoemission experiment is proportional to the sum over all transition probabilities.
In addition, the conservation of momentum is obtained by

$$\vec{k}_f = \vec{k}_i + \vec{G} + \vec{k}_{ph} \approx \vec{k}_i + \vec{G} \; . \tag{2.8}$$

$\vec{G}$ represents any reciprocal lattice vector and considers possible momentum transfer to the crystal lattice. The momentum of the photon $\vec{k}_{ph}$ can usually be neglected in ARPES experiments using photon energies in the VUV–range (vacuum ultra violet: $h\nu = 10..40$ eV corresponding to $\vec{k}_{ph} = 0.05..0.2\ \AA^{-1}$) compared to the dimension of the Brillouin zone (in the order of 1 $\AA^{-1}$). In this case, only direct transitions between electronic bands are possible. This means, that the momentum is kept constant or is changed by an integral multiple of the reciprocal lattice vector. In ARPES experiments using higher photon energies, the change of the momentum has to be considered.
(ii) The second step of the "three-step–model" deals with the movement of the electron through the solid towards the solid surface. The electron is scattered due to electron–electron, electron–phonon or electron–hole interactions. These scatting processes, for instance, contribute to the secondary–electron background in the measured spectrum. Furthermore, the resulting life–time shortening leads to broadened peaks in the photoemission spectrum for the corresponding transition. The inelastic mean free path of the electrons in the solid is typically limited to a few monolayers using photon energies in the VUV to XUV range (see Fig. 2.3) [34]. This makes the (AR)PES a very surface sensitive experimental method for analyzing the electronic structure.

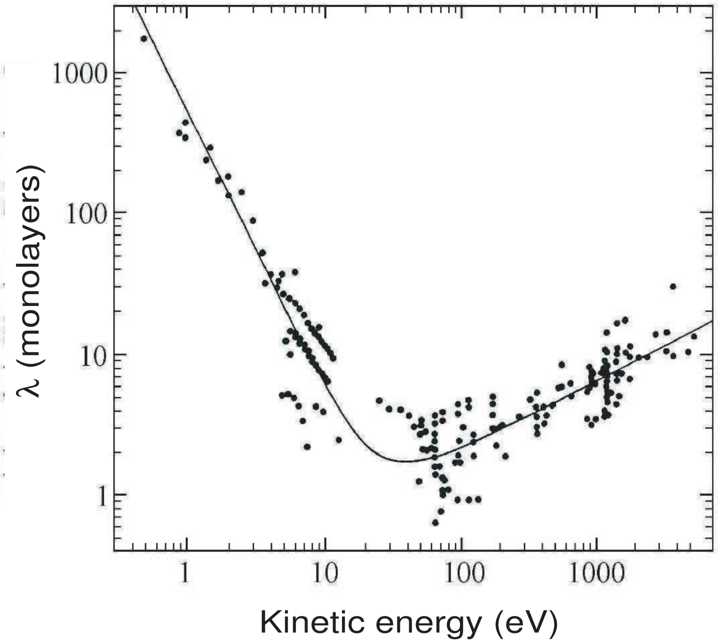

Figure 2.3: The electron inelastic mean free path as a function of the kinetic energy (from [34]): The mean free path is given in units of one monolayer. The data points are gained from PES measurements of different materials. This characteristic curve fits very well to every element and is, therefore, also known as the "universal curve" for the electron inelastic mean free path.

(iii) The third step describes the penetration of the electron through the surface into the vacuum. Here, the parallel component $\vec{k}_{f\parallel}$ of the electron wave vector is conserved while perpendicular component is changed the electron is diffracted because of the missing translation symmetry perpendicular to the surface. Furthermore, the kinetic energy of the electron in the vacuum can be described by the dispersion relation of a free–electron gas:

$$E_{kin} = \frac{\hbar^2}{2m_e}\vec{K}^2 \quad , \tag{2.9}$$

where $\vec{K}$ is the momentum of the electron in the vacuum. For the parallel components of the wave vector, the following relation is derived:

$$\vec{k}_{f\|} = \begin{pmatrix} k_{f\|x} \\ k_{f\|y} \end{pmatrix} = \frac{\sqrt{2m_e}}{\hbar}\sqrt{E_{kin}}\sin\vartheta \begin{pmatrix} \cos\varphi \\ \sin\varphi \end{pmatrix} \quad , \tag{2.10}$$

where ϑ and φ are the electron emission angles in the sample geometry (see Fig. 2.1). In the ARPES experiment the parameters E_{kin}, ϑ, and φ are measured and the corresponding parallel components can be calculated.

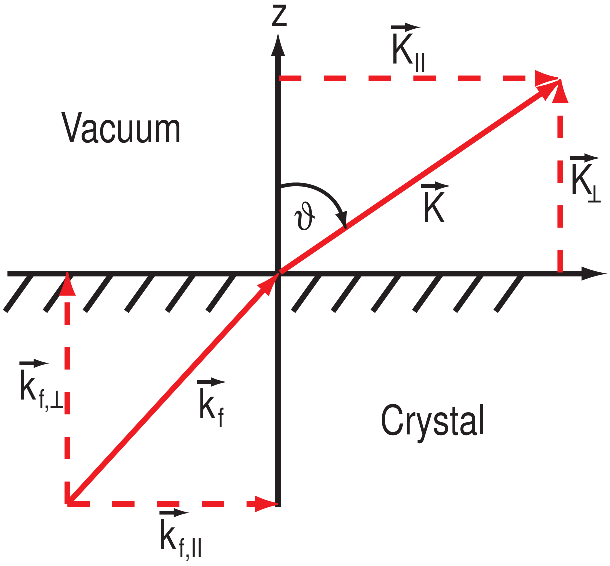

Figure 2.4: Illustration of the diffraction process of the electrons while penetrating the surface into the vacuum.

However, the determination of the perpendicular component of the wave vector $\vec{k}_\perp$ is more complicated due to the broken symmetry in this direction. If a free–electron like dispersion in the final state can be assumed, the dispersion relation is shifted approximately by $|eV_0|$, where V_0 is the so called inner potential. With this, the corresponding relation for the perpendicular component $\vec{k}_\perp$ is:

$$\left|\vec{k}_\perp\right| \approx \frac{1}{\hbar}\sqrt{2m_e(E_{kin}\cdot\cos^2\vartheta + |V_0|)} \ . \tag{2.11}$$

The inner potential V_0 is not directly experimentally accessible. It can be determined by, e.g., taking advantage of the symmetry in the $\vec{k}_\perp$ direction or comparing a measured ARPES series with a theoretically determined band structure.

2.2 Time–resolved pump–probe PES

Conventional PES as well as ARPES are techniques to measure the electronic structure of solids in the equilibrium state. With the development of ultra–short pulsed photon sources, the interest in measuring dynamical processes within the solid via spectroscopic methods strongly increased. Dynamic processes are, for example, externally induced phase transitions, structural changes of the surface or changes in the magnetic properties, which subsequently relax into the original equilibrium state [2–5]. In order to study these relaxation processes as well as the associated mechanisms leading to the relaxation, the electronic structure has to be measured as a function of time after an external excitation. This can be done by time–resolved photoelectron spectroscopy (TRPES). For this, excitation sources with pulse lengths in the femtosecond regime have to be used to be able to image fast processes like electron–electron ($\leq$ 100 fs) as well as electron–phonon ($\leq$ 10 ps) coupling, which are the fastest channels for the dissipation of energy after excitation.

In the last years, the development of pulsed radiation sources with pulse lengths down to the attosecond (laser systems) and femtosecond regime (free–electron lasers) enabled a strong increase in the number of time–resolved experiments. In the majority of cases, the experiments are performed as the so–called "pump–probe experiments". Here, two laser pulses with a defined and tunable delay are used. The first laser serves to excite the system, the second one samples the current state of the system after the excitation at a defined temporal delay.

In the case of TRPES (see Fig. 2.5) the pump pulse is used to excite the electronic

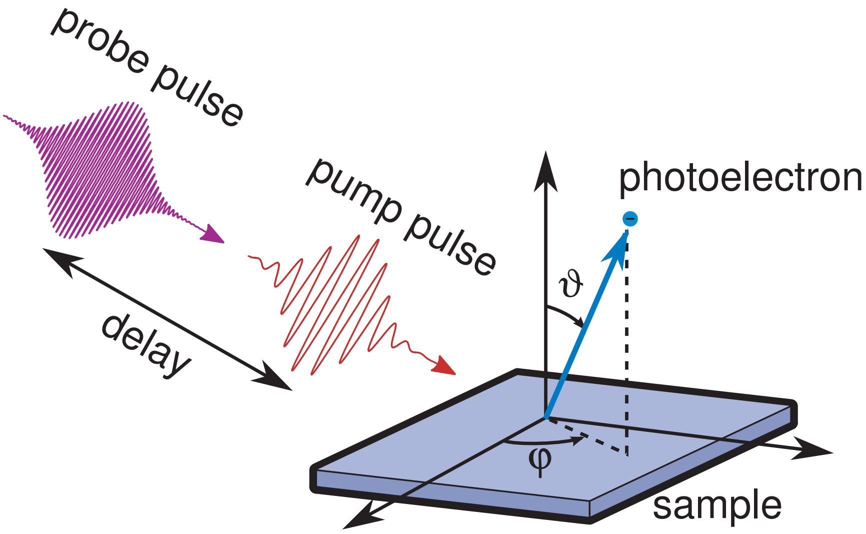

Figure 2.5: Scheme of a time–resolved pump–probe photoemission experiment (from Ref. [35]). In contrast to conventional PES or ARPES experiments, TRPES needs at least two short–pulsed photon sources. Here, an excitation pulse, the "pump pulse", deposites energy into the electronic system of the sample. With the second pulse, the "probe pulse" – exceeding the work function of the sample in order to generate photoelectrons – the excited electronic system is measured after a defined temporal delay. The temporal delay is subsequently varied within an interesting temporal interval and the relaxation process of the electronic system after excitation is monitored.

system. Here the photon energy lies below the ionization threshold and, therefore, no photoelectrons are emitted. A second pulse – with a photon energy exceeding the work function of the sample – is used to measure a photoelectron spectrum in order to monitor the non–equilibrium state at a defined point in time after the excitation. Finally, the delay between pump and probe pulse is varied in the interesting temporal regime. The changes in the photoelectron spectra as a function of the pump–probe delay monitor the evolution of the electronic structure of the solid during its equilibration process.

The temporal resolution of time–resolved experiments are especially limited by the pulse length of the used radiation sources. Proper radiation sources are, on the one hand, conventional ultra–short fs–laser sources, where the second or higher harmonic of the fundamental laser mode can be created by upconversion in a non–linear process. Depending on the generated photon energy the method is called second harmonic generation (SHG) or higher harmonic generation (HHG) [6–9].

On the other hand, the FEL as a fourth generation synchrotron radiation source generates photon pulses with pulse durations of some ten fs and is, therefore, suitable for time–resolved experiments as well. The experimental work in this thesis aimed to establish TRPES experiments at the FEL in Hamburg in close collaboration with the group of Wurth *et al.* from the University in Hamburg (Germany).

2.3 Modern photoelectron spectrometers

In order to measure photoelectron spectra, a variety of different kinds of photoelectron analyzers are used in this research field. In detail, these are plane or cylindrical mirror analyzers, time–of–flight analyzers and in a majority of cases hemisperical deflection analyzers. While first electron analyzers were only able to measure the photocurrent for one defined set of parameters (E_{kin}, ϑ, φ) at a time, nowadays, modern photoelectron analyzer are able to detect – dependent on the measurement mode and the requested energy and angular resolution – a specific kinetic energy interval as well as a defined angle or spatial interval in parallel. This significantly reduces the measurement time.

In this thesis, hemispherical analyzers equipped with such a parallel detection system were used for the PES experiments. On the left hand side of Fig. 2.6, an illustration of a hemispherical deflection analyzer and its working principle is shown. This analyzer mainly consists of three parts: (i) an electro–statical lense system, (ii) a hemispherical capacitor and (iii) an electron detection system in the exit plane of the hemispherical capacitor. The theoretically reachable energy resolution ΔE of such an analyzer system can be calculated by the following equation:

$$\Delta E = E_{pass}\left(\frac{s_1 + s_2}{4r_0} + \frac{\alpha^2}{4}\right) \qquad , \qquad (2.12)$$

where E_{pass} is the so called pass energy, s_1 and s_2 are the widths of the entrance and exit aperture. r_0 and α denote the mean radius within the hemispherical capacitor and the maximum acceptance angle of the photoelectrons entering the capacitor.

- The **electro–statical lense system** consists of a row of single electro–statical lenses, whose potentials can be varied seperately from each other. Within this lense system, incoming photoelectrons with a defined kinetic energy are retarded or accelerated via

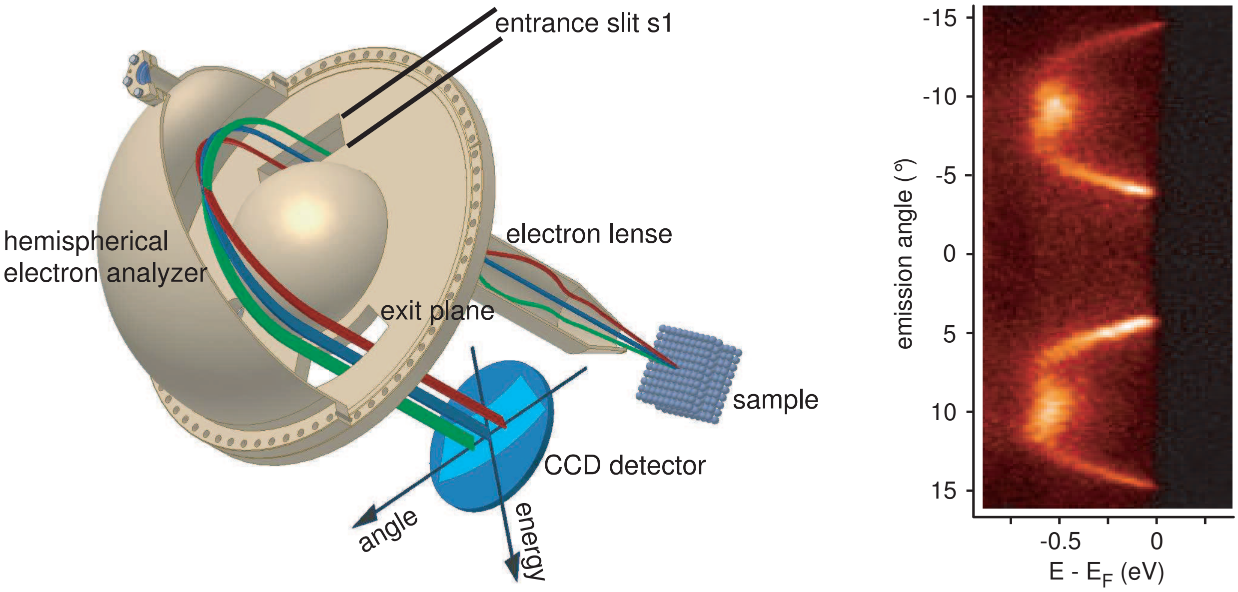

Figure 2.6: (Left) Illustration of a modern hemispherical deflection analyzer and its working principle (from Ref. [36]). The photoelectrons are imaged angularly resolved onto the entrance aperture s_1 of the hemisphirical capacitor. In the hemispherical capacitor the electrons are sorted with respect to their kinetic energy and in the exit plane a 2D–CCD detector is measureing the photoelectron intensity as a function of emission angle and kinetic energy in parallel. (Right) A typical photoemission intensity map of $(PbS)_{1.13}TaS_2$ measured with a hemispherical deflection analyzer (from Ref. [27]) and a 2D–CCD detector.

an applied voltage at the entrance plane of the hemispherical capacitor to the pass energy E_{pass}. This kinetic energy partly determines the energy resolution of the analyzer after equation 2.12. The smaller E_{pass} is, the better is the theoretically achievable energy resolution. Furthermore, the electrons are imaged by the lense system onto the entrance plane and, thus, onto the entrance aperture in a special way. Dependent on the measurement mode and, therefore, the combination of the applied lense voltages an angular or spatial dispersive distribution is achieved at the entrance aperture. (A lense mode with a high transmission of the photoelectrons but no further specified distribution is also possible.) In the angular dispersive case for example, the photoelectrons entering the lense system with an angle of 0° to the symmetry axis are imaged onto the center of the entrance aperture, while electrons with non–zero but equal entering angles are imaged on the same circle around this center point. This angular dispersion mode is apparently the most efficient lense mode for ARPES experiments. The entrance aperture into the hemispherical capacitor consist of one long and one short side. The long side is the angular dispersive direction of the analyzer, while the short side is the energy dispersive direction. The width of the entrance aperture s_1 as well as the maximum acceptance angle of the photoelectrons entering the hemispherical capacitor α account for the energy resolution of the experiment according to equation 2.12.

- While the electro–statical lense system is responsible for the angular dispersion in the analyzer, the subsequent **hemispherical capacitor** sorts the photoelectrons according to their kinetic energy. This is done by a virtual charge in the center of the hemisphere defined by the applied voltages on the two hemispherical capacitor plates. This central charge keeps the electrons entering the capacitor with the pass energy E_{pass} on the so called mean radius r_0. Therefore, electrons with higher (lower) kinetic energy are imaged further outwards (inwards) onto the exit plane than r_0. The beforehand generated angular dispersion is conserved even though slightly distorted during this imaging process.

- In the exit plane, the photoelectrons are detected via an **2D–detection system**, in order to measure an angular and kinetic energy interval as wide as possible in parallel and, thus, saving valuable measurement time. In most of the cases, this 2D–detection systems consist of a multi–channel plate, amplifying the incident electrons by a factor of $\approx 10^6$ while the local information is preserved. The generated charge cloud is accelerated onto a phosphor screen. Finally, the induced phosphorescence is acquired by a CCD camera. Due to the fact, that such a moderne photoelectron analyzer with parallel detection has no exit aperture, the pixel size of the 2D–detector system in energy dispersive direction is taken as the exit aperture width s_2 (typically ≈ 10 μm) for the calculation of the theoretical energy resolution achieved by the analyzer.

On the right hand side of Fig. 2.6, a typical angle– and energy–resolved detector image is shown. Clearly visible are the photoelectron intensities as a function of emission angle ϑ and kinetic energy E_{kin} (respectively binding energy E-E_F) belonging to the conduction bands of the transition metal dichalcogenide misfit compund $(\mathrm{PbS})_{1.13}\mathrm{TaS}_2$ [27] as well as the location of the Fermi level E_F. By means of those measured photoelectron intensity maps, conclusions can be drawn with regard to the occupied, momentum–resolved band structure $\mathrm{E}(\vec{k})$ of the solid surface including its Fermi surface $\mathrm{E}(\vec{k}) = \mathrm{E}_F$.

Today, using modern hemispherical deflection analyzers energy resolutions down to sub meV and angular resolution < 0.05 ° are reached [37,38].

One more analyzer technique should be mentioned in the context of modern photoelectron analyzers, the time–of–flight (ToF) technique (see Fig. 2.7). Currently, this technique is strongly forced in term of ARPES experiments due to the development of special 2D–electron detectors, the so called delay–line detectors. Those ToF analyzers in principle consist of a lense system comparable with the one from a hemispherical deflection analyzer. In the electro–statical lense system of an ToF analyzer the photoelectrons are likewise retarded and imaged onto the detection plane (cooresponding to the entrance plane in the hemispherical analyzer) with an angular or spatial dispersive distribution dependent on the lense mode. (Again a high transmission mode is possible.) Sorting of the photoelectron with respect to their kinetic energy is achieved by the measurement of the time of flight from the excitation at the sample surface via an ultra short photon pulse and the incidence on the detector plane. Therefore, a 2D–CCD detecter can not be used with this technique, because it does not measure the time of incidence but is integrating the signal over a defined time interval. Due to this delay-line detectors are used consisting of a multi–channel plate for electron amplification with conserved local information followed by a "wire–detector" measuring the induced charge spatially and temporally resolved.

The energy resolution achieved by an ToF analyzer is determined by the following parameters:

1. The pulse duration of the photon source – here, photon sources such as SHG or HHG laser systems with fs pulses as well as free–electron lasers with some ten fs pulses are good candidates.

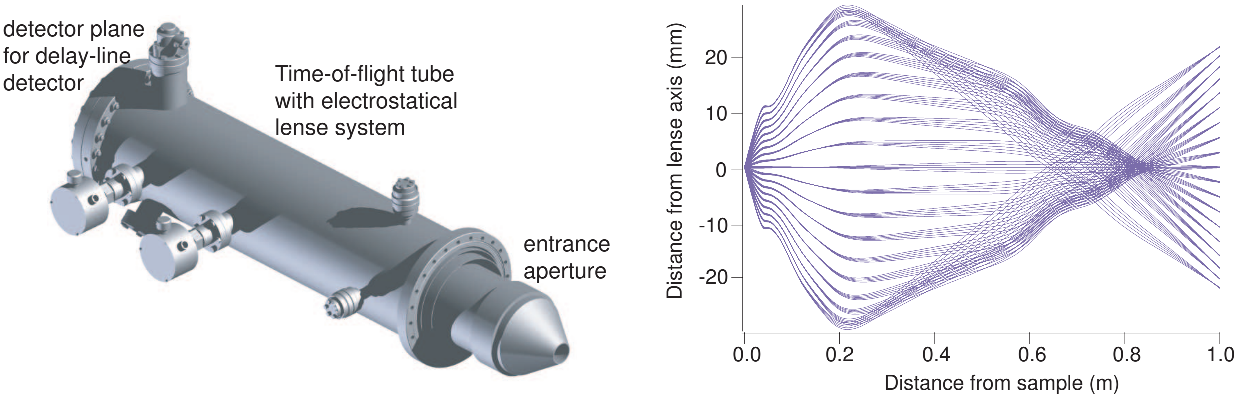

Figure 2.7: (Left) Illustration of a time–of–flight analyzer [39]. (Right) Calculated trajectories for 2 eV electrons with lens voltages optimized for a 0.1 eV energy window around 2 eV, and with angular window ± 15 ° using a ToF analyzer SCIENTA ArtOf 10k (from Ref. [40]).

2. The temporal resolution of the electronics used for measureing the temporal incidence of the electrons at the delay–line detector.

3. The kinetic energy of the electrons in the ToF spectrometer: The smaller the kinetic energy is, the larger is the temporal distance between two electrons with a defined kinetic energy difference at the detector and, thus, smaller kinetic energy difference can be measured with the temporal resolution of the electronics.

Therefore, ToF electron analyzers are only used at short–pulsed photon sources and are ideal for TRPES experiments. One advantage of a ToF analyzer compared to a hemispherical deflection analyzer lies in the parallel detection of the emission angle of the photoelectrons in two directions and not only in one direction due to the absence of an entrance aperture making this spectrometer especially ideal for mapping e.g. Fermi maps.

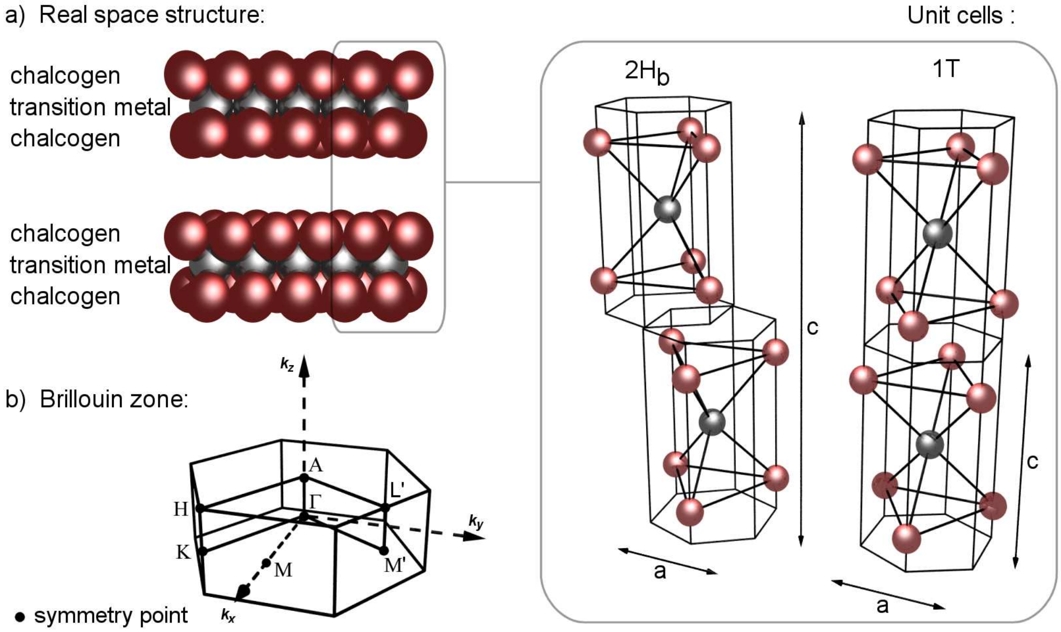

Figure 3.1: (a) Schematical side view of a transition metal dichalcogenide with unit cells of the 1*T*– and 2*H*–type. (b) Corresponding Brillouin zone of the 1*T*–type with high symmetry points (from Ref. [58]).

3 Transition metal dichalcogenides

The transition metal dichalcogenides (TMDC's) belong to the group of layered crystals. Due to their quasi–two–dimensional character, large anisotropies in the mechanical, optical and electronic properties are found [41]. Particularly interesting are temperature dependent electronic and structural phase transitions in form of charge–density waves (CDW's) and, thereby, potentially resulting periodic lattice distortions (PLD's) due to strong electron–phonon interactions [42–53]. Furthermore, the influence of other manipulating parameters on those phase transitions is intensively studied, e.g., the growth of Rubidium nanowires on the surface, the intercalation of adatoms into the van–der–Waals gap of TMDC's or excitation of the electronic structure via pulsed lasers [54–57]. In this chapter, the geometric as well as electronic structure of TMDC's are briefly introduced. A focus is laid on the TMDC's 1*T*–$TiTe_2$ and 1*T*–TaS_2, which are used for the PES experiments at the free–electron laser reported in chapter 7 and 8.

3.1 Geometric structure

TMDC's can be described by the general chemical formula TX_2. Here, the T indicates a transition metal atom of the groups IVb (Ti, Zr, Hf), Vb (V, Nb, Ta) and VIb (Cr, Mo, W), whereas X indicates a chalcogen atom of the main group VIa (S, Se, Te). As shown in figure 3.1 each layer of this compound consists of one hexagonally ordered transition metal layer sandwiched between two hexagonally ordered chalcogen layers. In this structure, each transition metal atom is coordinated by six chalcogen atoms, leading to two essentially different types of TMDC layers. In the trigonal prismatic 2*H*–type structure the atoms of

both chalcogen layers are lying directly upon each other, whereas in the nearly octahedral 1*T*–type structure, the layers are rotated by 180° against each other(see figure 3.1).
TMDC's show strong covalent bonds within the layers with an ionic part of 10 to 30 %. In contrast to that, these layers are bound among each other only by weak van der Waals forces, leading to a quasi–two–dimensional character. The resulting strong anisotropy is observable in the mechanical, optical as well as electric properties of the TMDC's, e.g., the electrical resistivity perpendicular to the layers can be one order of magnitude higher (and even more) than parallel to the layers. Due to the weak inter layer bonding the crystal can be easily cleaved. The crystal typically cleaves along the weak van der Waals bonding, leaving a clean, flat and very inert surface.
Finally, the Brillouin zone (BZ) of the quasi–two–dimensional TMDC's has to be introduced. Because of the hexagonal symmetry of the unit cell in real space, the Brillouin zone in reciprocal space is again hexagonal, but rotated by 30°. In figure 3.1(b) the BZ of a 1*T*–type TMDC is shown together with the high symmetry points. Due to its threefold symmetry the high symmetry directions $\overline{\Gamma M}$ and $\overline{\Gamma M'}$ as well as $\overline{AL}$ and $\overline{AL'}$ are not equivalent. The $\overline{\Gamma M'}$– and the $\overline{AL'}$–direction are defined as the directions where a chalcogen atom is situated above a metal atom.

3.2 Electronic structure

TMDC's show a large variety of electric properties, e.g., from semi–conducting, over half–metallic and metallic up to super–conducting properties. Except for superconductivity, this can be in first approximation explained via the general band theory with regard to the participating transition metal atoms. A scheme of the electronic density of states of the TMDC's is given by Wilson and Yoffe [41] (see Fig. 3.2(a)).

The s– and p–orbitals of the chalcogen atoms split into the bonding valence band states (σ) and the antibonding conduction band states (σ^*) resulting in a bonding–antibonding–gap of typically several eV depending on the compound. In between, the d–bands of the transition metal are located. These bands further split into the doubly degenerate level e_g containing the d_{xz} and d_{yz} orbitals, and the threefold degenerate level t_{2g} with the d_{z^2}, $d_{x^2-y^2}$ and d_{xy} orbitals. The degeneracy is further lifted in case of a mismatch of the unit cell from the ideal octahedral environment (in case of 1*T*–compounds) or the hybridization between the d_{z^2}, $d_{x^2-y^2}$ and d_{xy} subbands (in case of 2*H*–compounds). The resulting lowest d_{z^2} band is mainly responsible for the electronic properties of TMDC crystals. In a simplified model the Fermi level can be located on three different positions in the density of states (see Fig. 3.2 (a)).
In the first case, the transition metal atoms are from the group IVb from the periodic system and the d_{z^2} band is completely empty (d^0) and the Fermi level is located between this lowest d–band and the highest p–band of the chalcogen atoms. Depending on the overlap of these bands a semiconducting (see Fig. 3.2(a)) or semimetallic (see Fig. 3.2(b)) behavior is induced. In the second case, TMDC's containing transition metal atoms from the group Vb have a half–filled d_{z^2} band. Thus, the Fermi level cuts this band directly in the middle resulting in a metallic behavior. A completely filled d_{z^2} band and semiconducting properties can be found in the third case. Here, transition metals from the group VIb are involved.

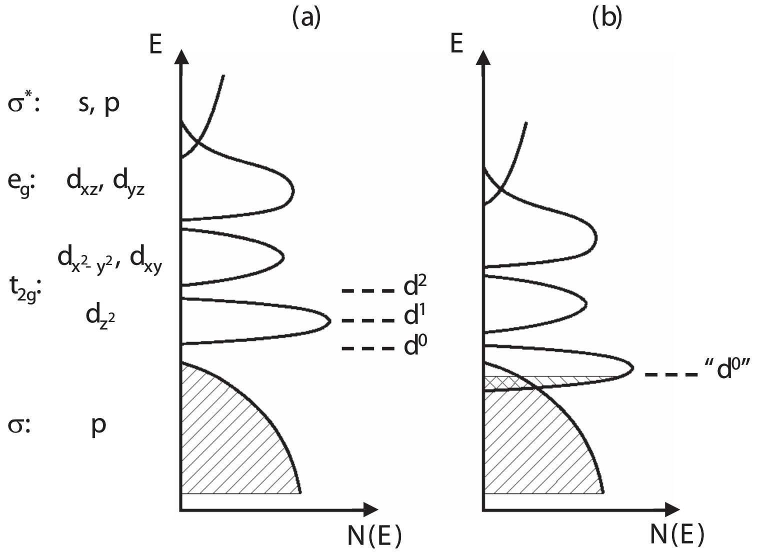

Figure 3.2: Scheme of the electronic density of states of TMDCs (from [59] after [41]): (a) The involved orbitals of the transition metal (d_{xz}, d_{yz}, d_{z^2}, $d_{x^2-y^2}$, d_{xy}) and the chalcogen atoms (s,p) as well as the symmetries of the states (e_g, t_{2g}) are indicated. Furthermore, the Fermi level position for different d–configurations are shown. The d^0– and d^2–configuration result in insulating or semiconducting properties due to the Fermi level lying within a band gap. However, the TMDC with d^1–configuration is metallic. (b) In case of overlapping p_z and d_{z^2} bands, the d^0–configuration can also lead to a metallic behavior.

3.3 Fermi–liquid reference system 1*T*–TiTe$_2$

TiTe$_2$ has an experimentally and theoretically well described electronic and geometric structure [59–66]. Furthermore, its geometric structure is constant due to the absence of any temperature dependent phase transitions. This makes TiTe$_2$ an ideal reference system for the commissioning of new experimental setups for PES. This is the main reason for using this reference system at the free–electron laser for the first ARPES measurements with high–intense photon pulses in chapter 7.

The crystal strucure of TiTe$_2$ is the 1T–structure. The unit cell contains one Titanium and two Tellurium atoms and forms the typical octahedral coordination. Its lattice constants (see Fig. 3.1) are $a = 3.78$ Å and $c = 6.50$ Å ($c/a = 1.72$) [60]. The ideal value for c/a in an ideally octahedrally coordinated transition metal atom is 1.633. In the case of TiTe$_2$, the coordination is triclinically mismatched. This has a direct influence to the band structure as will be seen in the following.

The TMDC TiTe$_2$ has the hexagonal Brillouin zone of the 1T–structure. The characteristic distances between the high–symmetry points (see Fig. 3.1) of the Brillouin zone are $\overline{\Gamma M} = \overline{\Gamma M'} = 0.960$ Å^{-1}, $\overline{\Gamma K} = 1.109$ Å^{-1} and $\overline{\Gamma A} = 0.485$ Å^{-1}.

In order to introduce the electronic band structure of TiTe$_2$, the band structure calculation in Fig. 3.3 is used. Though, Titanium is a group IVb transition metal and, therefore, TiTe$_2$ belongs to d^0–configurated TMDC's with predicted semiconducting properties, a metallic character is experimentally observed. This is due to the above mentioned slightly higher value for c/a and the trigonal mismatch of the ideally octahedral coordination of the Ti atoms. The larger the mismatch is, the smaller becomes the band gap between the p derived bands and the d_{z^2}–band. Finally, both bands overlap and the Fermi level is not longer

located within a gap, resulting in metallic sample properties. This is the case in $TiTe_2$, where the Ti $3d_{z^2}$ and the Te $5p$ bands overlap. Consequently, the Fermi level crosses both kinds of bands (see Fig. 3.3). With regard to the Ti–compounds, this effect is especially pronouncing in $TiTe_2$. The metallic character increases in the row of TiS_2, $TiSe_2$, $TiTe_2$ as a consequence of increasing c/a value.
Furthermore, the Ti $3d_{z^2}$ band plays a very special role in PES experiments due to strong photoemission intensities coming from this band near the M(L)–point of the Brillouin zone. This emission is approximately free from inelastically scattered electrons. In combination with its metallic character, this makes the TMDC $TiTe_2$ a reference system for the description of Fermi liquids [61, 62, 64].

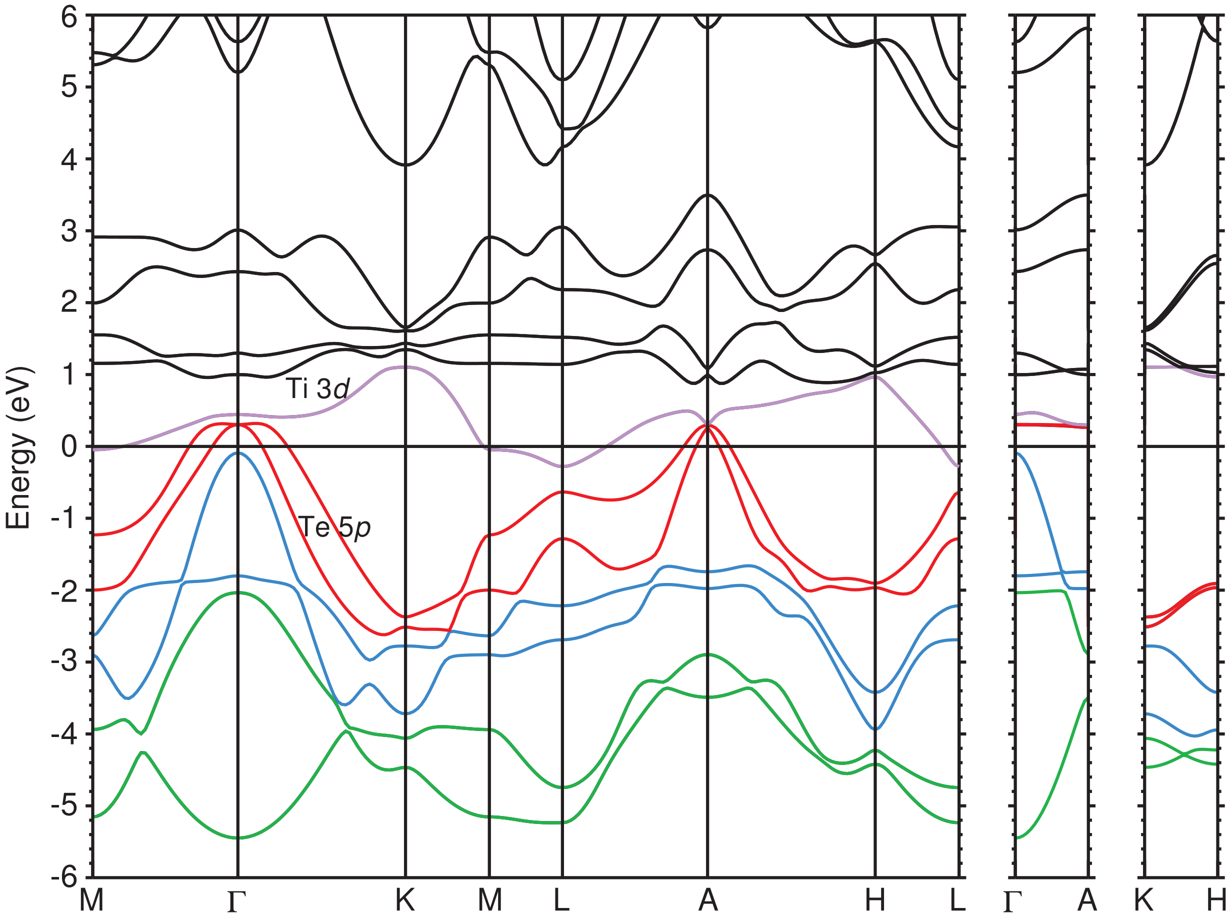

Figure 3.3: Calculated band structure of $TiTe_2$ including spin–orbit splitting from Ref. [65]. The electronic band structure is calculated along the high–symmetry directions of the Brillouin zone. The Te $5p$–derived bands are indicated as red, blue and green lines, the Ti $3d_{z^2}$ band is indicated as a violet line. The Te $5p$ bands (red) as well as the Ti $3d$ band are crossing the Fermi level determining the metallic character of $TiTe_2$.

3.4 Charge–density wave system $1\boldsymbol{T}$-TaS_2

The TMDC $1T$–TaS_2 is a very complex material compared to $1T$–$TiTe_2$ and contains interesting physics restricted to the hexagonal Ta layers. Due to an interesting phase diagram with a metal–insulator transition at low temperatures – by reason of strong electron–electron as well as electron–phonon couplings – $1T$–TaS$_2$ is an intensively studied model system [42, 50, 67]. In the following, the different phases of TaS$_2$ will be introduced with a focus on the insulating phase and the metal–insulator phase transition. Above a temperature of 570 K, an irreversible phase transition from $1T$–TaS$_2$ to the trigonal–prismatic $2H$–structure takes place and will not be further discussed here. An other transition into a superconducting phase takes place at 1.5 K and an applied pressure of more than 2.5 GPa [67] and will not be further discussed here as well.

Though a modulation of the electron density in the Ta layers – also known as "charge–density wave" (CDW) – already exists in $1T$–TaS$_2$ at room temperature, the most interesting phase is the insulating phase, the so called Mott–insulating phase [49,51], below a temperature of 190 K. In this phase, a low–temperature commensurate CDW (CCDW) phase coexists with a Mott–insulating phase [44, 47]. Due to strong electron–phonon coupling, the CDW leads to a distortion of the periodic structure of the Ta layers. The Ta atoms regroup into a $\sqrt{13} \times \sqrt{13}$–structure, the so–called "Star of David"–structure [52] (see Fig. 3.4). The inner ring of Ta atoms is stronger shifted towards the central atom than the outer ones, up to 7% compared to the undisturbed lattice positions [45]. This shift is connected with a modulation of the electron density towards the central Ta atom, where approximately 0.44 electrons per atom are transferred from the outer to inner Ta atoms [48].

This distortion also influences the binding energy of the Ta core electrons due to the different chemical environment of the three "types" of Ta atoms ("CDW–splitting"). This is shown in Fig. 3.4(c). The Ta $4f$ levels are not only spin–orbit–splitted into Ta $4f_{7/2}$ and $4f_{5/2}$. Each of them is further splitted into three sublevels with the intensity ratio 1:6:6 according to the different kinds of Ta atoms within the star of David. The peak from the central Ta atom is very weak and not resolved here [68].

The phase transition into the commensurate phase and, therefore, in the insulating phase can be followed in Fig. 3.4(a). Here the resistivity of $1T$–TaS$_2$ is plotted as a function of the temperature. Cooling the sample below 190 K leads to a the phase transition and an increase of the resistivity of more than one order of magnitude. This phase transition can also be observed in the behavior of the charge–density wave splitting Δ_{CDW} of the Ta $4f$ core levels [67,69]. This is explained by the increase of the CDW amplitude and, therefore, a larger dislocation of the Ta atoms from their undisturbed position in the $1T$–structure. Thus, the splitting of the Ta $4f$ levels is a direct indicator for the CDW amplitude [43].

Heating up the crystal in the CCDW phase results in a phase transition from insulating to a metallic nearly commensurate CDW (NCCDW) phase at temperatures of $\approx$ 220 K (note the hysteresis). The generation of a domain structure and a loss of phase coherence can be observed. The domains still form a commensurate CDW, but the domains with each other break the periodicity of the crystal structure and the domain walls form a metallic network suppressing the Mott–insulating phase [67]. Again this can be followed in the decreasing resistivity as well CDW splitting curve in Fig. 3.4(a).

Further increasing the temperature leads to a shrinking of the domains, finally ending in a phase transition into an incommensurate CDW (ICCDW) phase. At even higher temperatures between 543 K and 570 K, the CDW vanishes and a high–temperature metallic phase exist with a crystal structure in its clean octahedral coordination.

An other possibility to induce an insulator–to–metal like phase transition in $1T$-TaS$_2$ can be achieved by the deposition of energy within a short timescale. This has been done

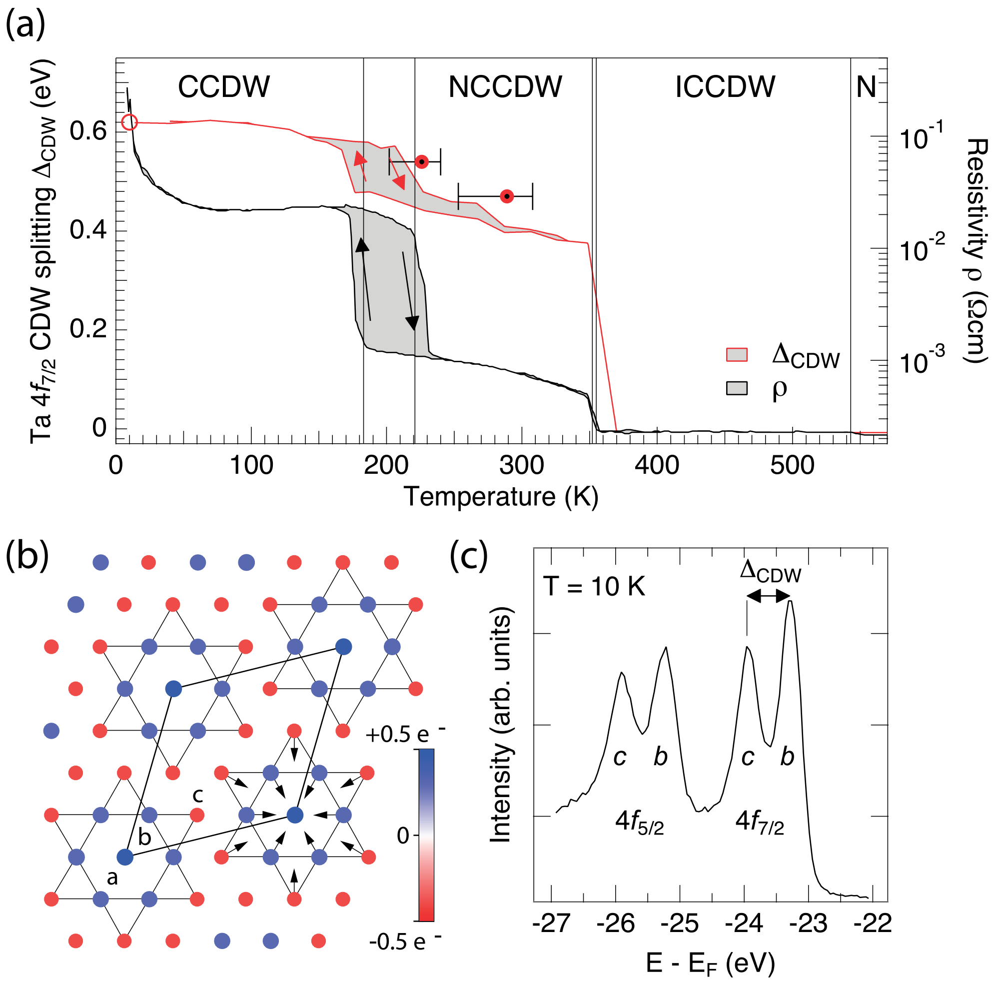

Figure 3.4: Charge–density wave phases of $1T$–TaS_2 (from Ref. [4]). (a) Phase diagram with the normal undistorted phase (N) as well as incommensurate (IC), nearly commensurate (NC), and commensurate (C) charge–density wave (CDW) phases. Temperature dependencies of the electrical resistivity (black line, Ref. [67]) and of the CDW–induced Ta $4f$ core level splitting Δ_{CDW} (red line, Ref. [43]). (b) Sketch of the CCDW showing star of David reconstruction with inequivalent a, b, and c Ta atom sites. The arrows indicate the displacement of the Ta atoms from their original positions. The electron density increases towards the center of the star. (c) Ta $4f$ photoemission spectrum measured with a photon energy of 156 eV. Each Ta $4f$ level is split into two peaks associated with sites b and c, separated by Δ_{CDW}.

by Perfetti *et al.* via pumping the crystal with an intense, short–pulsed infrared laser source [55,56]. They investigated the relaxation dynamics at the Fermi edge of the induced transition with time–resolved pump–probe PES.

The infrared pump laser delivered photon pulses with 50 fs pulse length, a photon energy of 1.5 eV and a energy density on the sample of 200 μJcm^{-2}. The photon energy was not sufficient for emitting photoelectrons. As a probe, the infrared laser was frequency multiplied up to a photon energy of 6 eV. The final pulse duration of the probe pulse was 80 fs. The temporal delay between pump and probe laser was controlled via a delay stage, and for different delays the energy distribution curves (EDCs) near the Fermi edge were measured.

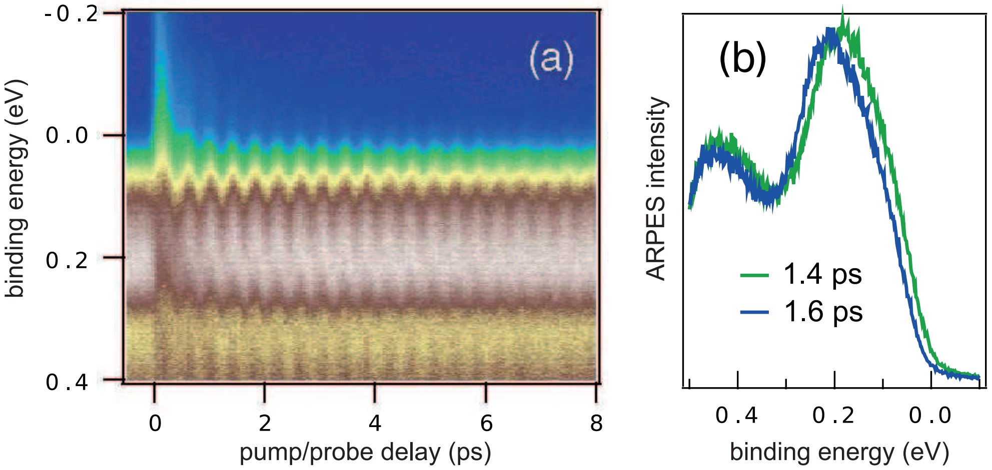

Figure 3.5: Time–resolved PES of the Fermi edge of Mott–insulating TaS$_2$ at a temperature of 30 K [55]. (a) Clearly visible oscillation of the CDW as a function of the temporal delay between pump (hν=1.5 eV, 50 fs, 200 μJ/cm^{-2}) and probe (hν=6 eV, 80 fs) pulse. (b) Two EDC, representing the maximum and minimum energetic position of the oscillating Fermi level.

The deposition of energy results in a heating of the electronic system up to 1100 K within a few fs. The relaxation dynamics of the electronic system was studied on the one hand on metallic TaS$_2$ at room temperature (≈300 K) and on the other hand on TaS$_2$ in the Mott–insulating phase (≈30 K). At the different temperatures, the time–resolved PES results look quite similar as depicted in Fig. 3.5 for the Mott–insulating phase. Hence, the time constants of the relaxation dynamics are significantly different and in the case of the Mott–insulator–to–metal transition an additional damped modulation in the Fermi edge position was observed.

In the case of TaS$_2$ at room temperature, the strong increase via the optical excitation was observed in form of a broadening of the Fermi edge as well as spectral intensity above the Fermi level coming from hot electrons. Afterwards, the relaxation process took place due to electron–phonon interactions with a time constant of 150 fs.

In the Mott–insulating phase, the deposited energy leads to a transition from the Mott–insulating to a metallic intermediate phase due to the strong increase of the electronic temperature. Here, with a time constant of 680 fs the system returned into the Mott–insulating phase. As already mentioned in addition to this a periodic modulation of the PE spectra was observed (see Fig. 3.5). This periodic modulation was explained by Perfetti *et al.* with the excitation of coherent phonons, which were already observed by Demsar *et al.* in reflectivity measurements [70]. These coherent phonons are also known in the literature as "breathing star of David" modes, and are explained as follows: The excitation energy generates hot electrons. The energy transfer between the electronic system and the lattice via a strong electron–phonon coupling induces periodic growing and shrinking of the "star of David" structure existing in the Mott–insulating phase. Two slightly different modes were found: $\nu_B = 2.45$ THz and $\nu_S = 2.51$ THz indicating the modes generated from the bulk and surface of the TaS_2 crystal, respectively. The bulk mode $\nu_B = 2.45$ THz corresponds with the breathing mode found in the reflectivity measurements [70, 71]. The breathing modes relaxated with a time constant of 9.5 ps. This was mainly due to incoherent phonons like electron–phonon or phonon-phonon couplings. The relaxation times are strongly dependent on the temperature and, thus, on the existence of incoherent phonons. The results of this time–resolved PES experiment could be successfully explained using the two–temperature–model [72]. Here, the dynamical relaxation process was studied by the observation of the EDC's near the Fermi energy. This was due to the limitation of a the probe energy of 6 eV.

Increasing the photon energy of a time–resolved ARPES experiment, in addition to the valence band at the Γ–point the full Brillouin zone as well as the core levels, and, thus, physical phenomena with chemical contrast are possible. At FLASH with its photon energies in the VUV to EUV regime, e.g., time–resolved pump–probe core–level PES experiments on TaS_2 and, therefore, the evolution of the CDW–splitting of Ta $4f$ levels after excitation will be feasible.

4 The free–electron laser in Hamburg (FLASH)

In material science, different kinds of light sources are essential in order to study the nature of matter. In photoelectron spectroscopy, light sources delivering photons with energies from the vacuum ultra violet up to the hard X–ray regime are used, i.e., gas discharge lamps, laser sources and X–ray tubes in the laboratory as well as synchrotron radiation sources at research facilities like DESY[1] in Hamburg, BESSY[2] in Berlin, etc.. In order to describe a radiation source, the physical parameter "brilliance" is defined as the number of delivered photons per area, solid angle, time and 0.1% bandwidth. For pulsed radiation sources, the "peak brilliance" is more meaningful, describing the brilliance of single photon pulses. Figure 4.1 exemplarily depicts the peak brilliance of todays modern synchrotron radiation sources as a function of photon energy.

Free–electron lasers (FEL) are fourth generation synchrotron radiation sources delivering highly intense, short pulsed (some ten fs) and coherent light, tunable in its photon energy. Especially the FEL in Hamburg (FLASH) is regarded as the most brilliant synchrotron light source in the VUV and XUV range (4.12 to 30 nm), while the LCLS (Linac Coherent Light Source) in Stanford, USA is covering a higher photon energy range up to 0.15 nm. The outstanding characteristics of the produced pulses opens the path for studying physics, previously not possible with conventional radiation sources.

There are experiments investigating samples under extreme conditions on a fs–time scale benefiting from the high photon intensities focused on a some ten μm spot size [16]. An optical ps–laser served as a probe laser. By changing the delay between the FEL pulse and the optical probe pulse and by measuring the reflected optical laser beam via a CCD camera, the dynamics of sample destruction could be studied. Other groups were able to study multi ionization processes at molecules, atoms and clusters [15–18]. Here, molecules have been ionized multiple times [16–18], while multi ionization of clusters has lead to a destruction by a so–called coulomb explosion [15]. Finally, Chapman *et al.* performed diffraction experiments and were able to produce a coherent diffraction pattern from a non–periodically structured object by using one single shot [13, 14]. This diffraction pattern could be reconstructed to the original image. The sample itself was destroyed after this single shot experiment. In general, FLASH can be used to probe ultra fast (some 10 fs), physical, chemical and biochemical processes at a spatial resolution according to the delivered wavelength (at least in diffraction experiments).

In contrast to the above mentioned experiments, in PES experiments the FEL radiation should not destroy the samples under investigation. However, the highly intense FEL radiation may give the possibility to study the effects of high fields on the electronic band structure. Concerning this the question rises, if this will be realizable or if other effects disturb the measurements at the necessary intensities, such as space–charge effects due to a huge amount of electrons emitted from the sample surface within a short time. Furthermore, the vision of time, space and angle resolved PES can be followed. First, a good time–resolution is given by the shortness of the FEL pulses combined with an optical fs–laser as a pump source. Second, spatial resolution can be achieved by focusing the FEL radiation via reflective zone plates [19] or photon sieves [20, 21] to a sub micrometer spot. For this the total transverse coherence of the FEL radiation is used as well as the high intensities, resulting in enough pulse intensities at the sample position. Third, angle resolution

---

[1] Deutsches Elektronen–Synchrotron

[2] Berliner Elektronenspeicherring–Gesellschaft fr Synchrotronstrahlung

will be achieved by using a conventional hemispherical analyzer being able to measure a specific angle and energy interval in parallel. And with the photon energy up to the X–ray regime, one is able to map the momentum resolved valence band structure of the complete first as well as higher Brillouin zone.

In the following, the working principle of a SASE–FEL will be described. Furthermore, the FEL in Hamburg, the monochromator beamline PG2 and the optical laser system will be introduced briefly, which were used for the photoemission experiments as a function of photon intensity and the time–resolved PES presented in chapter 7 and 8, respectively.

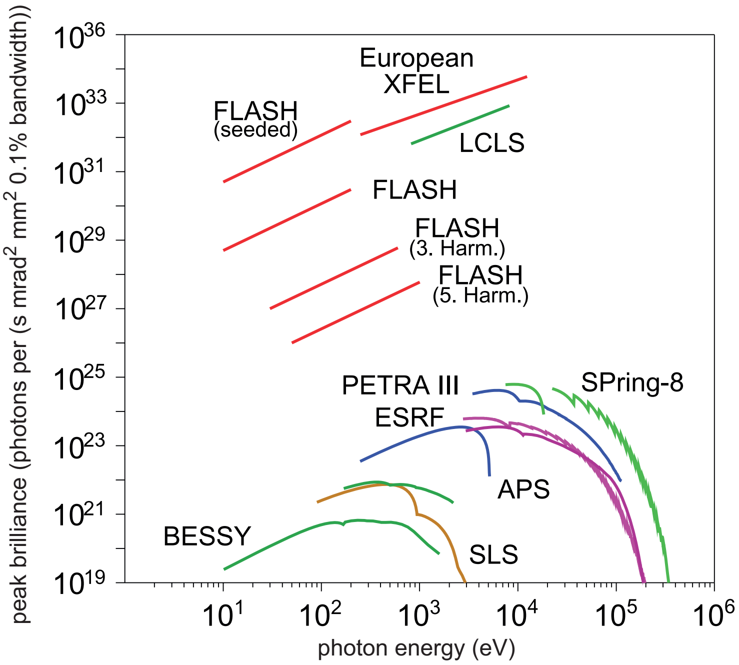

Figure 4.1: Peak brilliance of different free–electron lasers (FLASH, European XFEL, LCLS) compared to modern 3^{rd} generation synchrotron radiation sources (BESSY, PETRA III, ESRF, SLS, APS, SPring-8) [11].

4.1 Working principle of a SASE–FEL

In the beginning of synchrotron radiation, it was a by–product at the facilities of nuclear physics, where charged particles were accelerated to relativistic energies on circular paths to let them collide. Since then, this by–product gained more interest and was used to perform spectroscopic, imaging as well as X–ray–diffraction experiments taking advantage of monochromators to choose one specific wavelength from the generated spectrum. New technologies for generating synchrotron radiation were developed, increasing the brilliance of these sources by orders of magnitude.

Today, the synchrotron radiation facilities originally used in high energy physics are indicated as the 1^{st} generation of synchrotron radiation sources. The bending magnets of the synchrotron radiation sources are used to keep the charged particles on their circular path, while they are accelerated to relativistic velocities. The resulting acceleration of the relativistic electrons or positrons leads to a loss of energy via emitting electro–magnetic rays perpendicular to the acceleration direction. Due to relativistic velocities of the charged

particles, the electro–magnetic waves are focused in the direction of propagation. The particles emit a characteristic continuous and broad spectrum with a strong divergence of the photon beam and a maximal photon energy dependent on their kinetic energy.
In the 2^{nd} generation of synchrotron radiation sources the synchrotron is exchanged by a so called "storage ring". Here, the charged particles, typically electrons or positrons, are again traveling on a circular path, but with a constant kinetic energy. The magnet structures are typically superbends or wigglers. Superbends are bending magnets with higher magnetic fields, leading to a stronger acceleration of the particles and, therefore, to a higher average photon energy of the emitted spectrum. A wiggler consists of periodically arranged magnet structures, which keep the electron bunch on a slalom course (similar to the magnet structure of an undulator in Fig. 4.2). One can compare the wiggler with a row of bending magnets with changing orientation, so the resulting spectrum is similar to the one of a bending magnet, but more intense. The variation of the gap between the magnet structures changes the magnetic field and, thus, influences the emitted radiation spectrum. Higher magnetic fields result in higher average photon energies of the emitted spectrum.
With the implementation of undulators, the 3^{rd} generation of synchrotron radiation sources were born. The magnet structure of an undulator is similar to the one of a wiggler, but the magnetic field is weaker leading to a narrower slalom course and, therefore, to a smaller divergence of the emitted radiation. The emitted radiation of every undulator period is thereby interfering constructively with each other resulting in a nearly discrete spectrum consisting of the fundamental and higher harmonics. The emitted wavelength λ can be calculated by the "undulator equation" [73]:

$$\lambda = \frac{\lambda_u}{2\gamma^2}(1 + \frac{K^2}{2}) \ . \tag{4.1}$$

The wavelength is dependent on the Lorentz factor γ, defined as the ratio between moving and rest mass $\frac{m}{m_0}$, or accordingly between total energy and rest energy $\frac{W}{W_0}$ of the accelerated particle. The undulator parameter K can be calculated by:

$$K = \frac{e_0 B_u \lambda_u}{2\pi m_e c} \ . \tag{4.2}$$

The generated radiation is typically a million times shorter than the period of the undulator magnets λ_u. This is due to the shortening of the wavelength by $1/\gamma$ and $1/2\gamma$ due to length contraction and a blue shift because of relativistic Doppler effect. Therefore, the radiation is able to reach the X–ray regime, though the undulator period is in the order of some ten millimeter. B_u is the magnetic flux density of the undulator magnets and can be varied, comparable with the wiggler, via changing the undulator gap. Undulators deliver highly brilliant (see Fig. brilliance at BESSY, PETRA III, ESRF, SLS, APS and SPring-8 in Fig. 4.1), partly coherent and almost monochromatic synchrotron radiation. The average photon energies reached by undulators are typically smaller than achievable with a wiggler because of the weaker magnetic field.
The radiation power in all the above mentioned synchrotron radiation sources is increasing linearly with the number of charged particles in the particle bunch. Furthermore, a pulse duration of some ten ps can be reached. In free–electron lasers (FELs), regarded as the 4^{th} generation of synchrotron radiation sources, the pulse duration can be further decreased to a few fs, and the radiation power is proportional to the square of the charged particles. The main component for generating FEL radiation is no other than an undulator, so that

the undulator equation 4.1 is also valid for an FEL. The main difference is the length of the undulator. An FEL–undulator is far longer, so that the bunched relativistic electron beam, crossing this undulator, has the time to interact with its own spontaneously emitted electro–magnetic field.

The process leading to FEL radiation will be briefly explained in the following and is illustrated in Fig. 4.2. An electron bunch is traveling on an almost sinusoidal path through the periodic magnetic field of the FEL–undulator. In the first part of the undulator, the electrons are spontaneously emitting radiation according to the "undulator equation" 4.1. Afterwards, the electrons are interacting with this radiation. Electrons which are in phase with the electric field are stimulated and are transferring kinetic energy to the radiation field, electrons out of phase are gaining kinetic energy. Furthermore, the electron bunch is obviously traveling slower through the undulator than the electro–magnetic wave. When the electron bunch is traveling half of an undulator period while the light wave is slipping by one half of an optical wavelength in forward direction, always the same electrons are interacting with the same part of the electromagnetic wave, and, accordingly, are loosing or gaining kinetic energy. This process leads to a density modulation of the electron bunch in the direction of propagation and is called "microbunching" (see Fig. 4.2). The distance between the slices is similar to the emitted wavelength. The resulting electron slices of one bunch are oscillating in phase. The amplitudes of the electro–magnetic waves emitted by each electron can be summed up, leading to a radiation power proportional to the square

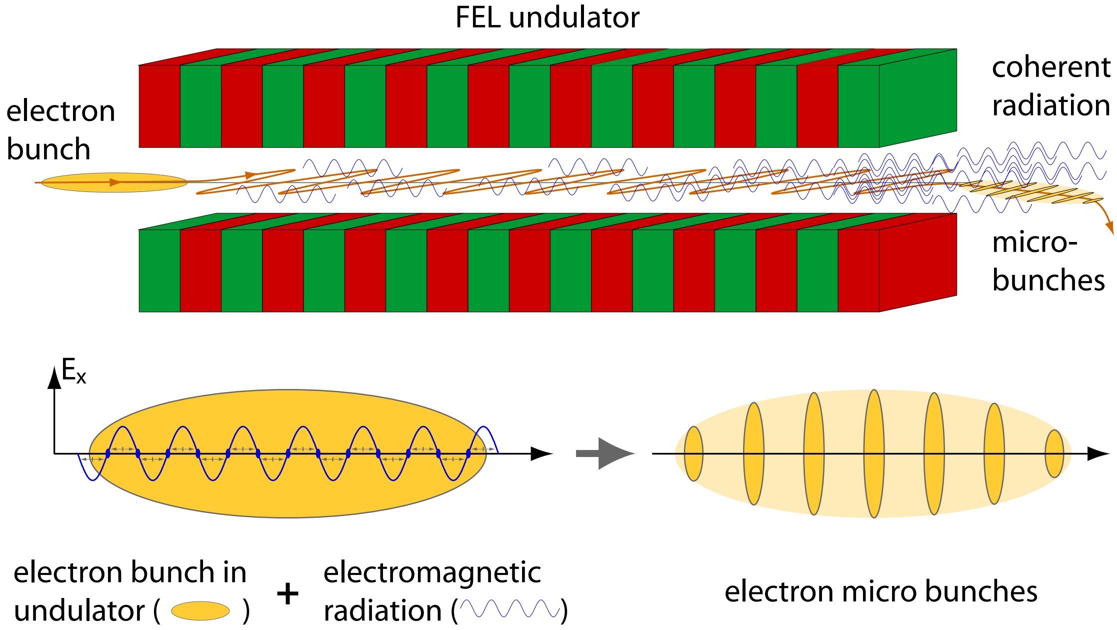

Figure 4.2: Illustration of the SASE (Self Amplified Spontaneous Emission) process and associated microbunching of a highly compressed electron bunch in an FEL–undulator [27]: The electron bunch (yellow ellipse) passes the undulator on a slalom path, and the electrons spontaneously emit photons (blue sine waves) in the first undulator section (top and bottom, left). In the following, the electron bunch interacts with the strong electromagnetic field leading to a density modulation ("microbunching") of the electron bunch with a lateral distance equally to the emitted wavelength (bottom, right). These generated slices oscillates in phase resulting in a radiation intensity proportional to the square of the number of electrons in the bunch.

of the numbers of electrons in the electron bunch. Furthermore, the radiation power of the electron bunch is increasing exponentially as a function of the covered distance in the undulator as long as the microbunching is proceeding. Saturation is reached when no further microbunching is possible due to repulsive forces between the electrons within the micro bunches. The whole process leading to FEL–radiation is called "Self Amplified Spontaneous Emission (SASE)".

FELs typically deliver synchrotron radiation with pulse durations of some ten femtoseconds, with high intensities and almost perfect transversal coherence. In terms of peak brilliance, these photon sources exceed conventional 3^{rd} generation synchrotrons by several orders of magnitude (see Fig. 4.1). However, there are still a few disadvantages. These are photon energy fluctuations in the range of 1% of the used photon energy as well as intensity variations of up to 20% from pulse–to–pulse. This is mainly due to the statistical nature of the SASE process and the varying starting point of the amplification process from noise. Furthermore, the electron bunch entering the FEL–undulator has a non–zero kinetic energy bandwidth. Since the generation of undulator radiation is dependent on the kinetic energy of the electrons, more than one wavelength can potentially be amplified. This photon energy fluctuation becomes more relevant in terms of huge intensity fluctuations, when a monochromator is used to select one specific wavelength.

Those problems with photon energy and intensity fluctuations can be solved via using a "seeded" FEL [74–77]. This means that the amplification of spontaneous emitted light within an energy bandwidth of the electron bunch is prevented by injecting highly–intense radiation with the fundamental wavelength into the undulator. Microbunching starts using this fundamental wavelength. Therefore, only this wavelength is amplified until saturation and no further amplification of wavelengths differing from the undulator wavelength takes place. This results in an increase of brilliance by up to two orders of magnitude due to decreased bandwidth compared to a non–seeded FEL. Furthermore, the FEL pulse duration and radiation intensity is stabilized significantly. The seeding of a FEL in the VUV to X–ray regime can be done in two ways: On the one hand, monochromatized undulator radiation can be used. The advantage of this setup is, that the wavelength can be varied steplessly, especially advantageous for photoemission experiments. On the other hand – and this option is preferred at FLASH – the VUV light delivered by higher harmonic generation of a pulsed laser source can be used as the injected fundamental. At FLASH, this seeding technique is planned for fundamental wavelength between 13 nm and 30 nm.

4.2 Layout and parameters of FLASH

In Fig. 4.3 the layout of FLASH is illustrated. FLASH is a single–pass FEL delivering light pulses from the VUV to the X–ray regime (30 eV to ≈ 1500 eV with fifth harmonic [12]). Single–pass means that no resonator mirrors (as in infrared–FELs) are used and that the FEL radiation is produced by the SASE–process (see subsection 4.1).

In the beginning, a UV–laser hits a Cs_2Te sample and electrons are emitted and accelerated. After first bunch compression in a radiofrequency gun (RF gun) an electron bunch with a temporal width of ≈ 4 ps is further accelerated to relativistic kinetic energies (up to 1.25 GeV [12]) by seven superconducting, linear accelerator modules (LINACs). On two locations in between additional bunch compression is performed via special magnetic structures. Here, the faster electrons are guided on a longer, curved path than the slower ones. Subsequently, a highly dense electron bunch with a current of several 1000 A, a diameter of less than 100 μm and a small energy bandwidth is passing a collimator unit and is entering the FEL undulator along the undulator axis. The FEL–undulator of FLASH consists of six separate undulators with a length of 4.5 m each. In the first undulator section, the electrons within the bunch are emitting spontaneously synchrotron radiation according to the undulator equation 4.1. SASE starts and the electron bunch is density modulated to slices with distances of the emitted wavelength. The gain length is defined as the length within the FEL–undulator where the radiation power grows by a factor of e $\approx$ 2.718 and is specified for FLASH with 1 m. The wavelength of the emitted FEL radiation is changed by the variation of the kinetic energy of the electrons. The undulator gap size is fixed at 12 mm and the magnetic flux density is B_u=0.747 T leading to a maximum deflection of the electron bunch from its center position of 10 μm. At the end of the FEL–undulator, the electron bunch is deflected into the beam dump, and the FEL pulse is guided to the different beamlines in the experimental hall.

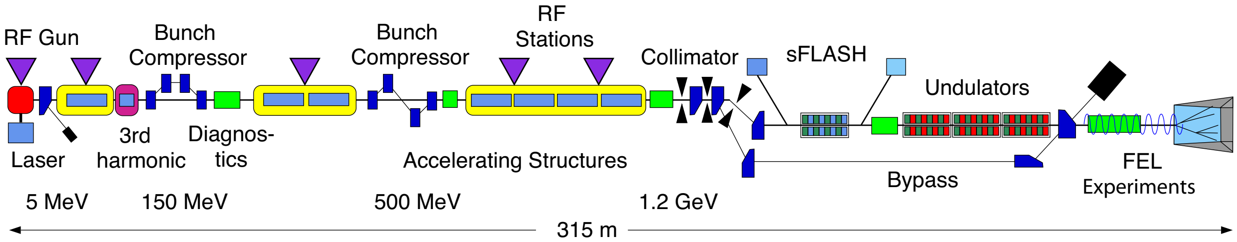

Figure 4.3: Layout of the free–electron laser in Hamburg [12]: This illustration shows the main components necessary for the production of FEL–radiation, starting with the creation of electrons with an UV–laser and a RF gun, the subsequent acceleration and compression of the electron bunch, the generation of SASE radiation in the FEL–undulator, and, finally, the deflection of the electrons into the beam dump.

At FLASH, the user can choose between two different running modes. The first one is the ”single–pulse mode”. In this mode every 200 ms (currently the repetition rate at FLASH is 5 Hz) one single ”micro pulse” with a pulse duration of 10–70 fs is delivered. In the second mode, the ”multi–pulse mode”, with the same repetition rate of 5 Hz a whole bunch of micro pulses (”pulse train”) is generated with a micro pulse separation of a few μs (this is adjustable).

In both modes the characteristic pulse–to–pulse intensity and photon energy fluctuations are observed (see section 4.1). Furthermore, an effect called ”temporal jitter” is very pronounced in the multi–pulse mode. The temporal jitter describes the phenomenon that the temporal pulse position varies due to different entering times of the electron bunch into the FEL undulator. In the multi–pulse mode, the electron bunches are automatically readjusted by the machine during the first 10–15 micro pulses leading to temporal mismatch of at least 100 fs. All these fluctuating pulse parameters are problematic and sometimes inacceptable for some experiments. This is for example the case in PES experiments using a hemispherical electron analyzer with a two–dimensional CCD detector. The CCD detector is too slow to temporally resolve the micro pulses with their temporal distances of a few μs.

Further parameters of FLASH are listed in table 4.2. FLASH was opened for users operation in the year 2005 and, since then, was gradually upgraded. Due to this the parameters have slightly be changed since the ARPES experiments in 2005 (see chapter 7) to the time–resolved PES experiments in 2008 (see chapter 8).

The fundamental wave length produced by FLASH ranges between 4.12 nm (300 eV) to 42 nm (30 eV) [12]. Furthermore, the odd harmonics of the fundamental wave length are available as well, expanding the useable photon energy range considerably. Though, the pulse intensity decreases to 1% when going from one odd higher harmonic to the next. This makes FLASH also interesting for experiments that need wavelengths in the water window (2.3–4.4 nm), and, therefore, very attractive for, e.g., the science on biological materials.

FLASH parameter	Nov. 2005	Nov. 2007 to Aug. 2009 [12]
number of photons per single pulse	$\approx 10^{12}$	$\approx 10^{13}$
photon energy regime (fundamental)	$\approx$ 38.5 eV	26 to 190 eV [12]
single pulse duration (before monochromatization)	10–70 fs	10–70 fs
repetition rate	2 Hz	5 Hz
number of single pulses per pulse train	n$\leq$ 20	n$\leq$ 500
average energy per single pulse	1–10 μJ	10–100 μJ

Table 4.1: User operation parameters available at FLASH during the measurement periods, when the PES experiments presented in this thesis took place. The investigation of sample destructions and the ARPES measurements on $TiTe_2$ were performed in 2005 (see chapter 7.3 and 7.4, respectively). The core–level PES experiments on the Ta $4f$–level of TaS_2 as a function of pulse intensity (see chapter 7.5) and the time–resolved PES measurements (see chapter 8) took place within the second user period from 2007 to 2009.

4.3 Monochromator beamline PG2

Figure 4.4 shows a photograph of the experimental hall at FLASH. There are five beamlines for user experiments. One of these beamlines is the monochromator beamline PG2. Here, the experiments for ARPES, core–level PES and time–resolved PES presented in this thesis were performed.

The main part of the PG2 beamline is the plane grating monochromator SX700. This monochromator significantly increases the energy resolution of the radiation from $E/\Delta E \approx 100 - 200$ delivered by the SASE–FEL up to $E/\Delta E \approx 10000 - 50000$. Furthermore, higher harmonics can be separated from the fundamental and a wave length of 1.6 nm can be reached in the fifth harmonic. The monochromator contains two different gratings, the high transmissivity grating with 200 lines/mm and the grating for high energy resolution experiments with 1200 lines/mm. Different photon energies can be used without changing the focal point in the experimental chamber due to a combined movement of the monochromator grating together with a mirror. The incident as well as the exit angle of the FEL–radiation on the grating differ as a function of the photon energy. The change of the incident angle leads to a change in the illuminated number of lines on the grating N_{lines} contributing to the monochromatization. In turn this change results into a changed

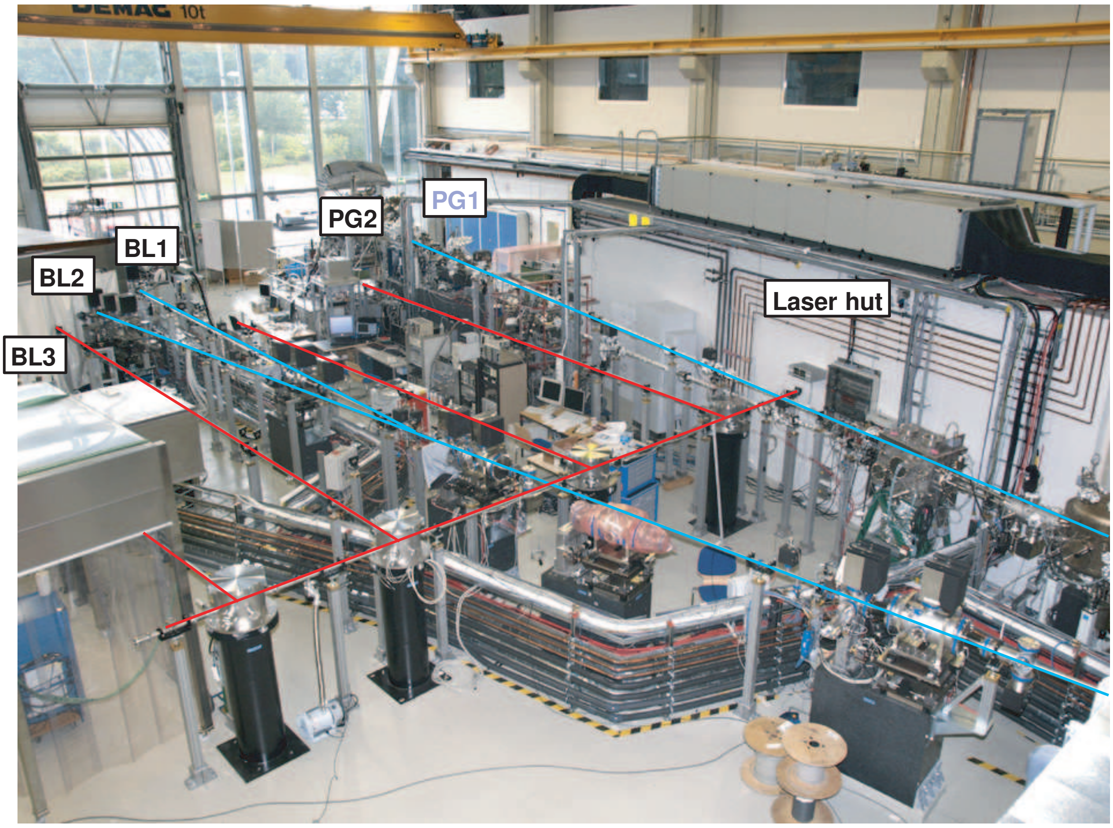

Figure 4.4: Photograph of the FLASH experimental hall with five beamlines (BL1–3, PG1 and PG2) for user operation. The laser hut contains two optional IR–laser systems delivering photon pulses with a wavelength of 800 nm and 120–150 fs duration for pump–probe experiments. The blue and red lines indicate the possible trajectories of the FEL and the IR–laser pulses, respectively.

temporal length of the FEL pulse due to $\Delta t \propto N_{lines}$ [78]. The temporal resolution can decrease from originally 50 fs before the monochromator to more than 1 ps behind the monochromator. A combination of mirrors focus the FEL radiation to a nominal spot size of 50 μm and a divergence of $\approx$ 1 mrad. By now, the best reported spot size was 270 × 400 $\mu\mathrm{m}^2$ (FWHM) [79].

Due to the immanent intensity fluctuations from pulse–to–pulse, an intensity monitoring device is positioned between the monochromator and the experimental chamber. This was realized by a multi–channel–plate detector (see section 5.1.2).

In order to effectively decrease the total intensity of the monochromatized FEL pulses, different filter foils (silicon, zirconium) of different thicknesses can be transferred directly into the beam. This will especially be advantageous for the time–resolved photoemission experiments, below the limitations due to space charge effects presented in chapter 8.

4.4 Infrared–laser systems for time–resolved pump–probe experiments

In order to perform time–resolved pump–probe experiments at FLASH, a second pulsed photon source is provided in the FLASH hall and installed in the laser hutch indicated in Fig. 4.4. The two different infrared–laser (IR–laser) systems as well as the streak camera and the "electro–optical sampling" (EOS) device for determining the relative temporal distance between the FEL and IR–laser pulses are briefly introduced in the following.

At FLASH, there are two available laser systems, both producing photon pulses with 800 nm wavelength and pulse durations of 120–150 fs. One system consists of a **Ti–Sapphire laser** for single pulse operation. The repetition rate is 5 Hz corresponding with the FEL–operation rate, and the maximum pulse energy is 25 mJ per pulse. The second system is a **burst mode laser** being able to mimic the temporal behavior of the FEL radiation in the multi pulse mode. It delivers up to 800 pulses per pulse train with variable temporal distance in the μs regime. The maximum pulse energy is limited to $\approx$ 50 μJ per pulse.

The FEL and the IR–laser systems are separate and independently running systems, therefore, the relative temporal distance between both must be measured as exactly as possible with special timing tools. Furthermore, for time–resolved measurements of dynamic processes the temporal distance between both must be varied. The variation of the temporal distance is achieved via a delay stage in the laser hutch. The **delay stage** mainly contains mirrors with adjustable distance to each other. This results in a variable traveling path and, hence, in a controllable delay between FEL and IR–laser pulses. The delay can be changed with a resolution of some femtoseconds over a temporal interval of several hundred picoseconds.

In order to measure the relative temporal distance between both pulses, a **streak camera** and an **electro–optical sampling (EOS) tool** are available at FLASH. Both system should briefly be described here:

- Within the **streak camera**, decoupled parts of the IR–laser and the FEL hit a cathode and both eject photoelectrons. These generated electron pulses cross two capacitor plates. Here, they are deflected by an electric field perpendicular to the propagation direction. The electric field is varied as a function of time. So, both electron pulses are deflected differently according to the current electric field strength between the plates while passing them. Finally, a two dimensional detector detects the electron pulses, and the distance between both measured peaks directly contains the information about the relative temporal distance between both pulses. The temporal resolution of the streak camera is quantified to be ≈ 1 ps.

- A better temporal resolution can be achieved with the **electro–optical sampling device (EOS)** [80]. An illustration of the functional principle of this device is shown in Fig. 4.5. A decoupled part of the IR–laser is guided through an electro–optical crystal. This electro–optical crystal is located in the FEL tunnel, next to the trajectory of the electron bunch. An electron bunch passing this crystal induces an electrical field and suddenly changes its birefringent properties. Only a part of the IR–laser pulse is crossing the crystal during this time and is, therefore, interacting with its changed birefringent properties resulting in a change of the polarization of the electro–magnetic wave. After passing the crystal, a polarizer absorbs the part of the laser pulse with the original polarization. Only the influenced part (with changed polarization) hits the CCD detector, and the spatial displacement from the middle position of the CCD detector contains the information about the temporal delay. Fig. 4.5 illustrates, what happens when the IR–laser pulse is crossing the electro–optical crystal at three different times, before, exactly when and after the electron bunch is passing. The temporal resolution is determined to be ≈100 fs. This is especially important in order to perform time–resolved experiments beyond the jitter limitations.

However, both systems, the streak camera as well as the EOS tool, are installed quite far away from the experiment and, therefore, are measuring the temporal distance between FEL and IR–laser pulse only relatively. For time–resolved experiments after the monochromator, it is essential to determine the temporal overlap directly at the sample position. In order to do this, a special timing–tool is installed (see subsection 5.2.2).
Using the monochromator beamline PG2, the IR burst–mode laser and the streak camera for determining the temporal delay between IR and FEL laser pulses, it was the first time possible to perform pump–probe PES experiments with ultra short photon pulses and adequate pulse intensities at high photon energies, as it will be demonstrated with our time–resolved PES experiments on the TMDC $1T$–TaS_2 in chapter 8.

To conclude, PES experiments using synchrotron radiation sources up to the third generation significantly differ from experiments performed at the FEL due to the differing radiation characteristics described in this chapter. Synchrotron radiation sources typically deliver photon pulses with quasi–constant pulse energy and pulse durations in the order of some ten ps. These sources are ideal in order to perform conventional PES experiments, but are disadventageous with regard to TRPES. In contrast to that, the photon pulses generated by the FEL are significantly shorter, allowing TRPES with fs resolution, and especially time–resolved core–level PES due to reachable photon energies (up to 1500 eV at FLASH). Furthermore, the highly intense FEL radiation allow to study space–charge effects in PES as well as possible high–field effects.
Nonetheless, PES at FLASH is ambitious and a few challenges have to be solved in

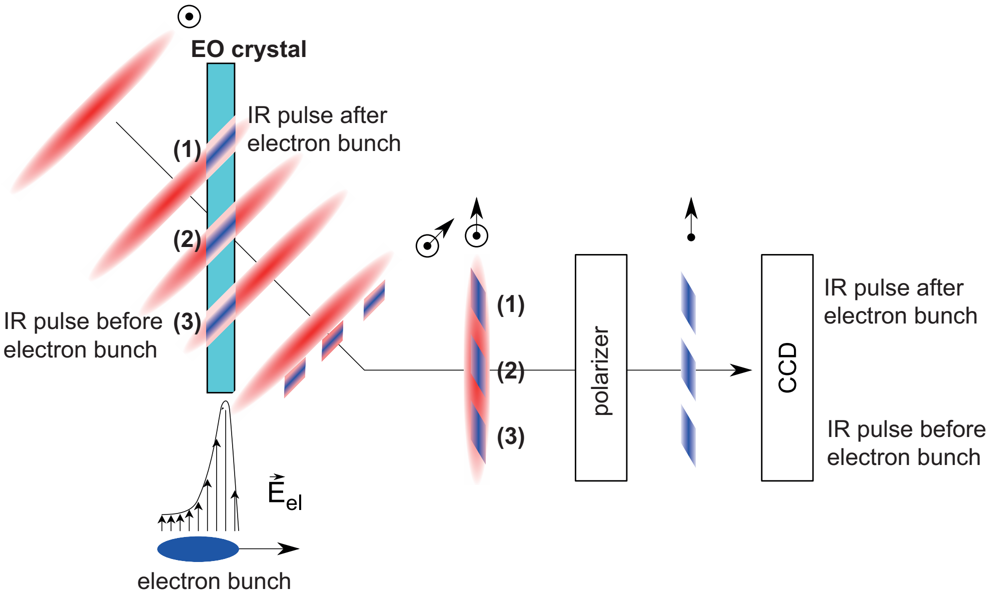

Figure 4.5: Illustration of the electro–optical sampling device for determining the relative temporal distance between the FEL pulse and the IR–laser pulse (from [35] after [80]): The IR–laser pulse is crossing the electro–optical crystal while its bifringent properties are changed due to the induced electric field from the passing electron bunch. The polarization of the IR–pulse is partly changed, dependent on the delay between electron bunch and the laser pulse. Depicted are three different situations: (1) the IR pulse arrives after the electron bunch, (2) both pulses arrive coincidently and (3) the IR pulse arrives before the electron bunch. The part with changed polarization is filtered from the original IR–pulse polarization, and the temporal displacement between laser pulse and FEL electron bunch can be derived by the lateral position on a CCD detector. A temporal resolution of 100 fs can be reached with the EOS.

order to realize the mentioned PES experiments at FLASH. These are, on the one hand, the intrinsically fluctuating FEL pulse intensities and, on the other hand, the temporal inaccuracy of the pulses within a few hundred femtoseconds (temporal jitter). In order to control the pulse intensity in our experiment, existing intensity monitoring systems were integrated into a typical PES experimental setup and one monitoring system was developed during this thesis. For TRPES, a system for collinear injection of an optical laser into the FEL beam was developed and set up, and a timing tool was integrated into the PES chamber in collaboration with the research group from Wurth *et al.* for measuring the delay between optical laser and FEL pulses. The set up of the existing instruments as well as the newly developed tools will be described in the following chapter 5.

5 Experimental aspects for PES at FLASH

Free–electron lasers using SASE delivering light pulses in the VUV to X–ray regime became interesting for a great variety of research topics [13–18, 81–84] due to their outstanding characteristics, i.e., ultra–short pulses as well as peak intensities exceeding conventional radiation sources by several orders of magnitude. With regard to PES, these properties can be used for time–resolved pump–probe experiments to investigate dynamical processes in the electronic properties of solids. Especially the available photon energies up to 1500 eV reveal the possibility to study nonequilibrium dynamics of condensed matter systems with full elemental, chemical and atomic site selectivity with the technique of time–resolved XPS.

This chapter describes the instrumental aspects to realize intensity–dependent as well as time–resolved photoemission experiments at FLASH. These are, on the one hand, pulse–intensity monitors determining the intensity of every incident single pulse. On the other hand, timing tools are needed measuring the delay between excitation (pump) pulse and FEL pulse as accurate as possible to ensure high temporal resolution only limited by pulse durations. One further aspect to be mentioned here is the realization of the data acquisition at FLASH differing from experiments at conventional light sources due to the uniqueness of each photon pulse. The development of those tools and the setup of complete experiments leading to the experimental results discussed in the chapters 7 and 8 have been a major part in this work.

5.1 Tools for FEL pulse intensity measurements

Even though the properties of FEL radiation are very promising in order to study new physics, there are still a few limitations to handle during the experiments. The SASE process itself is of stochastic nature and, therefore, subject to fluctuations. This leads to significant intensity fluctuations from pulse train to pulse train, and even between single pulses within one pulse train. Since a lot of physical effects under investigation are dependent on intensity, the measurement of single pulse intensities as accurate as possible is mandatory for research projects at FEL sources. Furthermore, the monitoring tools have to operate in parallel to the experiments and, therefore, in a non–destructive way. At FLASH two different systems for pulse intensity monitoring are implemented: a gas–monitor detector (GMD) and a micro–channel–plate (MCP) detector. Both systems will be briefly introduced in the following. The MCP tool has been calibrated for a photon energy of 38.5 eV, hence, a conversion equation for the usage of differing photon energies will be deduced. Finally, a home built intensity–monitoring system will be presented, the so called "I–tube", whose development is part of this thesis. This system enables to acquire absolute single pulse intensities more accurately and universally during the experiment (at any photon energy and intensity).

5.1.1 Gas–monitor detector

The gas–monitor detector is a device for online photon diagnostics and is described in detail in references [85–87]. A scheme of a GMD currently used at FLASH is shown in

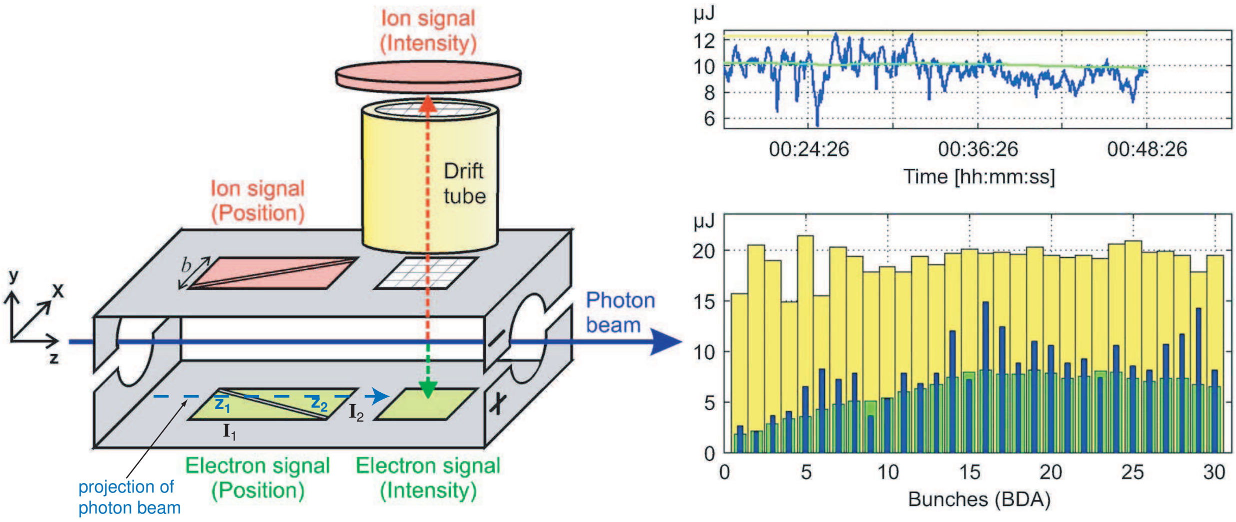

Figure 5.1: Left hand side: Illustration of the functional principle of the Gas–Monitor–Detector (GMD) at FLASH (from Ref. [85]). The splitted electrodes on the left side analyze the beam position, while the electrodes on the right side determine the photon pulse intensity. Right hand side: GMD diagnostic panel in the FLASH control system during an FEL run with 30 single pulses in one bunch train.

figure 5.1. The functional principle is based on the photoionization of a gas.
The ions and electrons are generated in the gas chamber. They are separated by an almost homogeneous electric field and are detected at signal electrodes. At constant gas pressure, the amount of detected ions is proportional to the number of photons in the single pulse. This is shown by the following equation for the so called spectral responsivity s_{ion} [85]:

$$s_{ion}(\hbar\omega) = \frac{I_{ion}}{\Phi} = \frac{q(\hbar\omega)QE_{ion}(\hbar\omega)}{\hbar\omega} \qquad , \tag{5.1}$$

where I_{ion} is the signal current at the electrode, Φ the radiation power, QE_{ion} the quantum efficiency of the detector and $q(\hbar\omega)$ the mean charge generated by one absorbed photon at a specific photon energy $\hbar\omega$. In contrast to classical ionization chambers, the GMD operates at significantly lower pressures ($\approx 10^{-3}$ Pa). This prevents the generation of secondary ionization processes.
The integrated ion signal $\langle I_{ion}\rangle$ (over 20 s) in the ”current mode” serves as a calibration for the determination of absolute photon pulse energies in the following way [85]:

$$s_{el}(\hbar\omega) = s_{ion}(\hbar\omega)\frac{\langle Q_{el}\rangle}{\langle I_{ion}\rangle}\nu \qquad , \tag{5.2}$$

where s_{el} is the spectral responsivity for the electrons in the pulsed mode and $\langle Q_{el}\rangle$ the average charge detected per FEL pulse. ν is the number of FEL pulses per time. Finally, the measurement uncertainty of pulse energies is less than 10%. Due to the fast electrons a temporal resolution of better than 100 ns can be reached. This temporal resolution is sufficient regarding a pulse separation of single pulses in a pulse train of 1 μs.
Additionally, the GMDs at FLASH can be used to determine the photon beam position. For this purpose two splitted electrodes are implemented in the ionization chamber (see Figure 5.1). The generated charges are again separated and accelerated by a homogeneous

electric field. The trace of incident charges on the electrodes corresponds to a projection of the photon beam in this direction. Therefore, one is able to determine the beam position via the measured signal ratio I_1/I_2, which corresponds to the ratio of the lengths of the projection on the splitted electrodes z_1/z_2 (see Fig. 5.1). For the determination of the photon beam position in the remaining direction, a second, perpendicularly oriented GMD is positioned behind the first one at FLASH. With this pair of GMDs, the photon beam position can be measured with an accuracy better than 20 μm. A second pair of GMDs is located 15 m away from the first pair, hence the photon beam direction can be determined with an uncertainty in the microradiant regime.

Figure 5.1 (right hand side) demonstrates the GMD diagnostic panel in the FLASH control system during an FEL run with 30 single pulses in one bunch train. The upper graph of the diagrams on the right hand side shows the long–term behavior of the mean ion signal, while the lower bar diagram depicts the pulse intensity distribution within the bunch train on a shot–to–shot basis.

In conclusion, the GMD setup at FLASH is able to measure online the single pulse energies sufficiently accurately without disturbing the beam characteristics with regard to the experimental setup at the beamline. Due to the location of the two pairs of GMDs in front of the monochromator of beamline PG2, only zero order and, therefore, maximum photon pulse energies (including a broad energetic spectrum of up to 1% of the used photon energy as well as higher harmonics) are known for experiments with high photon energy resolution. This makes the absolute pulse intensity monitoring with the GMDs at FLASH unfavorable with regard to PES experiments, where monochromatized radiation and a good energy resolution is essential. Nevertheless, the GMDs can be used for the calibration of other intensity monitoring systems installed behind the monochromator. This has been done, e.g., for the "MCP detector" described in the following.

5.1.2 Multi–channel plate detector

The multi–channel plate (MCP) based detector was developed to determine single pulse intensities within a wavelength range from 6 nm to 200 nm [88]. The MCP detector at the monochromator beamline PG2 at FLASH was built up by the research group of Wurth *et al.* from the University of Hamburg, Germany [89]. It is situated behind the monochromator and in front of the experimental station. Therefore, it is directly monitoring the pulse intensities used for the experiment contrary to the GMD, described in the previous section.

An illustration of the principle of the operation is shown in figure 5.2. The FEL radiation is crossing a gold mesh (transparency of 66%) with a grazing angle of 45°. The radiation is partially reflected in the direction of a multi–channel–plate directly positioned above the mesh. The primarily photoemitted electrons are amplified due to the applied high voltage by several orders of magnitude and the resulting current pulse can be measured. Careful calibration of the MCP with a flash lamp leads to the following gain function [90]:

$$\frac{MCP_{out}}{MCP_{in}} = 10^{g(HV)} \qquad . \tag{5.3}$$

MCP_{out} and MCP_{in} are the amplified and non–amplified signals in Vs at the MCP, respectively. The gain factor $g(HV)$ as a function of applied high voltage HV can be calculated

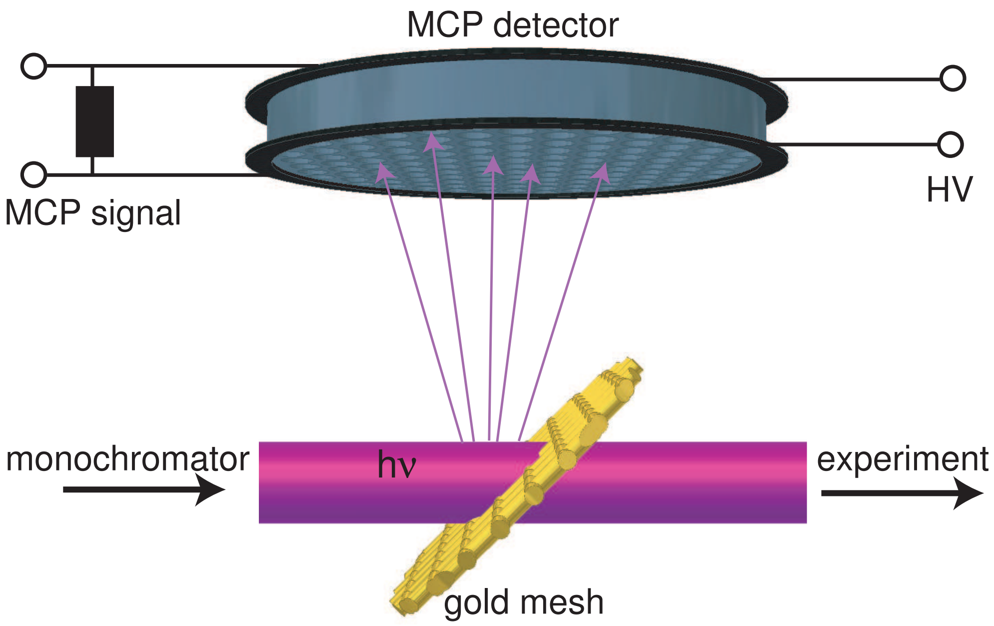

Figure 5.2: Scheme of the MCP detector at FLASH: The FEL radiation is partially reflected by a high transmissive gold mesh into a multi–channel plate. The amplified photo electron signal is measured and can be directly correlated with the photon pulse intensity.

by [90]

$$g(HV) = -8.46+3.4\cdot10^{-3}\cdot\left(\frac{HV}{[V]}\right)+3.04\cdot10^{-6}\cdot\left(\frac{HV}{[V]}\right)^2-7.29\cdot10^{-10}\cdot\left(\frac{HV}{[V]}\right)^3 \quad . \quad (5.4)$$

With the MCP detector at PG2, absolute photon pulse energies can only be measured for photon energies of 38.5 eV. It was calibrated using the GMD in front of the monochromator, a monochromator exit slit of 2 mm and the first harmonic FEL radiation [89]. A beamline transmission of $BT = 0.38 \pm 0.18$ was taken into account [79]. Plotting the absolute pulse energies delivered by the GMD against the measured MCP signal lead to a linear dependency. Linear regression resulted in the determination of absolute photon pulse energies E_{ph} for 38.5 eV radiation [89, 90]:

$$E_{ph}\,[J] = BT \cdot (a - b \cdot MCP_{in}\,[Vs]) \cdot 10^{-6} \quad , \quad (5.5)$$

with the coefficients a=3.2570±0.0023 and b=(-103.675±0.019)Vs^{-1}. The coefficients a and b were delivered by a calibration procedure using relatively high photon pulse intensities. Therefore, in the case of relatively low photon pulse energies the coefficient a must be neglected, only the proportionality factor b is relevant then. Otherwise one would get a non–vanishing pulse energy, when there is no incident light on the MCP. Furthermore, a refit of the measured calibration data to a linear function crossing the zero–point does not generate a significantly different slope.

In order to use different photon energies, e.g., the third harmonic of the FEL radiation, relation 5.5 has to be transferred with regard to photon energy dependent parameters. Essentially, there is a change in the reflectivity of the gold mesh $r(h\nu) = \frac{R(38.5\ eV)}{R(h\nu)}$ as well as a change due to the energy dependent conversion efficiency of the MCP $S(h\nu) = \frac{\sigma(38.5\ eV)}{\sigma(h\nu)}$.

From reference [91] the change in reflectivity is calculated. Here, the relevant parameter are the s–polarization of the FEL light, the incident angle of 45° as well as a surface roughness of the scattering surface of 1.8 to 2 nm. The resulting correction factor due to the change in reflectivity as a function of photon energy can be seen in figure 5.3(a). The second correction factor due to the photon energy dependent conversion efficiency of the MCP is depicted in 5.3(b). The basis for this graph lies in reference [92], where the efficiency of a bare MCP is presented as a function of the incident photon energy. Finally, a universal function for the number of photons per pulse $N_{ph}(h\nu)/MCP_{in}$ (see Fig. 5.3(c)) and the relative accuracy $\Delta N_{ph}/N_{ph}(h\nu)$ (see Fig. 5.3(d)) is derived and can be calculated by using table 5.1.2.

The following disadvantages occur when using the MCP detector. The MCP detector is calibrated for photon energies of 38.5 eV. An imprecise conversion is needed that is presented here (see Fig. 5.3 (d) and table 5.1.2). Even while using 38.5 eV FEL radiation, the relative error exceeds 50 % due to the inaccuracy in the beamline transmission BT [79]. The theoretical conversion presented here is practicable up to 120 eV mainly due to the underlying assumptions with regard to the reflectivity of the gold mesh and the conversion efficiency of the MCP as a function of photon energy.

The advantages of using the MCP detector at beamline PG2 for intensity dependent experiments at high photon flux are obvious. The detector covers the complete dynamic range of the radiation intensity at FLASH and does online intensity monitoring behind the monochromator. Especially for our studies of space charge effects in PES, it is essential to know the pulse intensities directly at the sample as accurately as possible.

Fitting parameters:	$f(h\nu) = \sum_{i=0}^{5} K_i \cdot (h\nu)^i$	
	$f(h\nu) = N_{ph}/MCP_{in}(h\nu)$	$f(h\nu) = \Delta N_{ph}/N_{ph}\ (h\nu)$
K_0	$-7.77 \cdot 10^{14}$	$4.77 \cdot 10^{-1}$
$K_1(\mathrm{eV}^{-1})$	$6.38 \cdot 10^{13}$	$8.19 \cdot 10^{-3}$
$K_2(\mathrm{eV}^{-2})$	$-2.05 \cdot 10^{12}$	$-2.64 \cdot 10^{-4}$
$K_3(\mathrm{eV}^{-3})$	$3.24 \cdot 10^{10}$	$3.69 \cdot 10^{-6}$
$K_4(\mathrm{eV}^{-4})$	$-2.54 \cdot 10^{8}$	$-2.14 \cdot 10^{-8}$
$K_5(\mathrm{eV}^{-5})$	$7.99 \cdot 10^{5}$	$4.75 \cdot 10^{-11}$

Table 5.1: The number of photons per single pulse $N_{ph}(h\nu)/MCP_{in}$ as well as the relative accuracy $\Delta N_{ph}/N_{ph}(h\nu)$ as a function of the used photon energy can be calculated by the polynomial fit $f(h\nu)$. See also the graphs (c) and (d) in Fig. 5.3.

5.1.3 Intensity tube for FEL pulse intensity monitoring

In order to monitor absolute photon pulse intensities, an additional system, the so called "Intensity tube" (I–tube), was developed in our research group as part of this thesis and two associated diploma theses [35, 93]. The I–tube is a 200 mm long, UHV–tube which is situated directly in front of the experimental chamber.

Figure 5.4 shows the principle setup of the I-tube. It consists of three units being able to measure the incident FEL radiation: a fine gold mesh (transmissivity of 47.5%, mesh aperture of 11 μm) and two ultra–fast photo diodes. One of the photo diodes (a) is

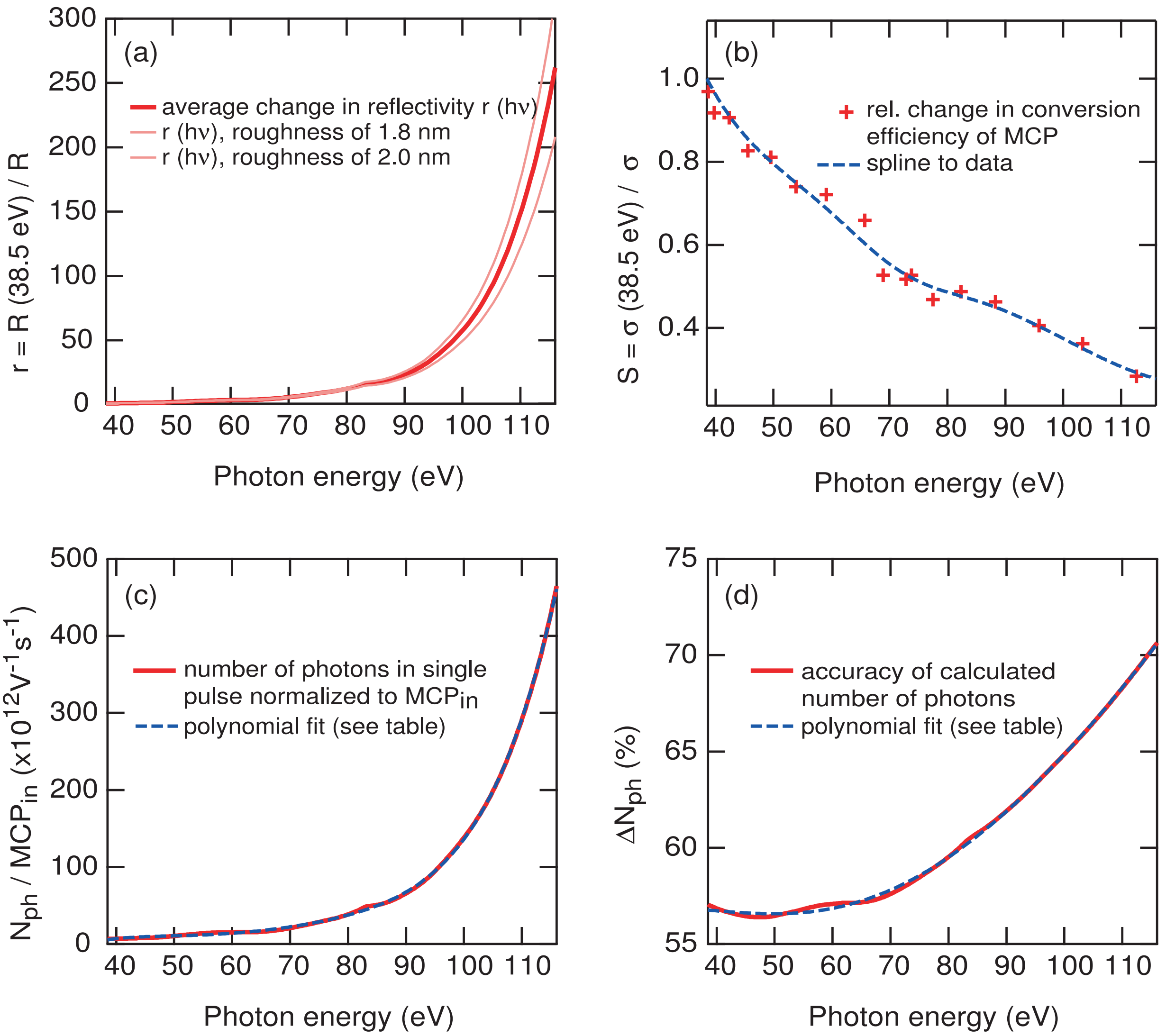

Figure 5.3: Determination of the number of photons per single pulse as a function of photon energy using the MCP detector at PG2, which was calibrated for $h\nu = 38.5$ eV. For this, the change in the reflectivity of the gold mesh $r(h\nu) = \frac{R(38.5\ eV)}{R(h\nu)}$ (see graph (a)) from [91] as well as the change in the conversion efficiency of the MCP $S(h\nu) = \frac{\sigma(38.5\ eV)}{\sigma(h\nu)}$ (see graph (b)) from [92] was used. The resulting relation for calculating the number of photons $N_{ph}(h\nu)/MCP_{in}$ normalized to the non–amplified MCP signal MCP$_{in}$ (see graph (c)) and the corresponding relative accuracy $\Delta N_{ph}/N_{ph}(h\nu)$ (see graph (d)) is given by the polynomial fit presented in table 5.1.2.

attached beside the main axis of the FEL beam, the other photo diode (b) as well as the gold mesh can be positioned directly in the beam via linear feedthroughs.

To determine absolute pulse intensities and, therefore, the number of photons in one single pulse, photo diodes of the model SXUV20HS1 (International Radiation Detectors Inc.) are used. These photo diodes are characterized by a short rising time of 2 ns and an extreme radiation hardness preventing damage to the diode due to the intense FEL radiation. Moreover, the SXUV diodes are calibrated for a wide photon energy range from 6 eV to 12 keV. This makes the photo diode (b) an ideal system to measure absolute photon numbers of the FEL pulses even if the radiation directly hits the diode. This option serves to calibrate the other two remaining units for online monitoring, the gold mesh and the photo diode (a).

For online monitoring of pulse intensities, the gold mesh is positioned directly in the photon beam. On the one hand, the incident photons are generating photoelectrons leaving the mesh as well as photoholes, which are almost instantaneously neutralized. This photocurrent serves as a measure of relative pulse intensities. On the other hand, the photons are partially reflected from the mesh surface in the direction of the photo diode (a), again resulting in a signal proportional to the pulse intensity. On all three units a bias voltage can be applied to prevent saturation effects. Screening of the electric field from the experimental chamber can be assured by linearly moveable, electrically connected copper edges. Furthermore, these copper edges serve as an option to determine the beam position at the entrance to the experimental chamber.

During the online monitoring, the gold mesh photocurrent is preamplified by a high–speed amplifying system DHPCA–100 from Femto Inc. It additionally serves as a current–to–voltage converter, and the resulting voltage signal of a whole pulse train is measured and stored by a digital storage oscilloscope LeCroy WaveRunner 6030A. In combination with the measured data a 24–bit–timestamp unique for each pulse train is stored. This timestamp is delivered by the FEL machine and is read out by the oscilloscope via an USB Digital I/O Device (NI USB 6501). Then, every stored intensity data set can be assigned to other experiment relevant data, e.g., PES spectra, delays in pump–probe–experiments, GMD or MCP detector intensities.

In general the use of the I–tube can be described as follows: Prior to the experiment, the gold mesh and the photo diode (b) are moved into the beam and intensities are measured on all three units. The gold mesh and the attached photo diode (a) are calibrated for the used photon energy with regard to the absolute measurement of incoming photons at the diode (b). Then the photo diode (b) is moved out of the beam and the experiment can start with a calibrated intensity monitoring system.

The development of the I–tube and first tests during FEL beamtimes are described in references [35, 93] in more detail. In [35] it was found that the gold mesh photocurrent behaves non–linearly as a function of pulse intensities at high photon flux in the first harmonic of FLASH. This intensity regime is anyway not interesting for PES experiments due to a resulting spectral broadening and shifts in a regime of several eV because of Coulomb interactions between a huge amount of generated photoelectrons. For lower intensities a linear behavior was found.

In future PES experiments at FLASH the I–tube will be favored over the MCP–tool, because a fast calibration to the used photon energy will be possible and no imprecise conversion relation (see table 5.1.2) will be necessary. Furthermore, the I–tube works for the whole photon energy regime delivered by FLASH.

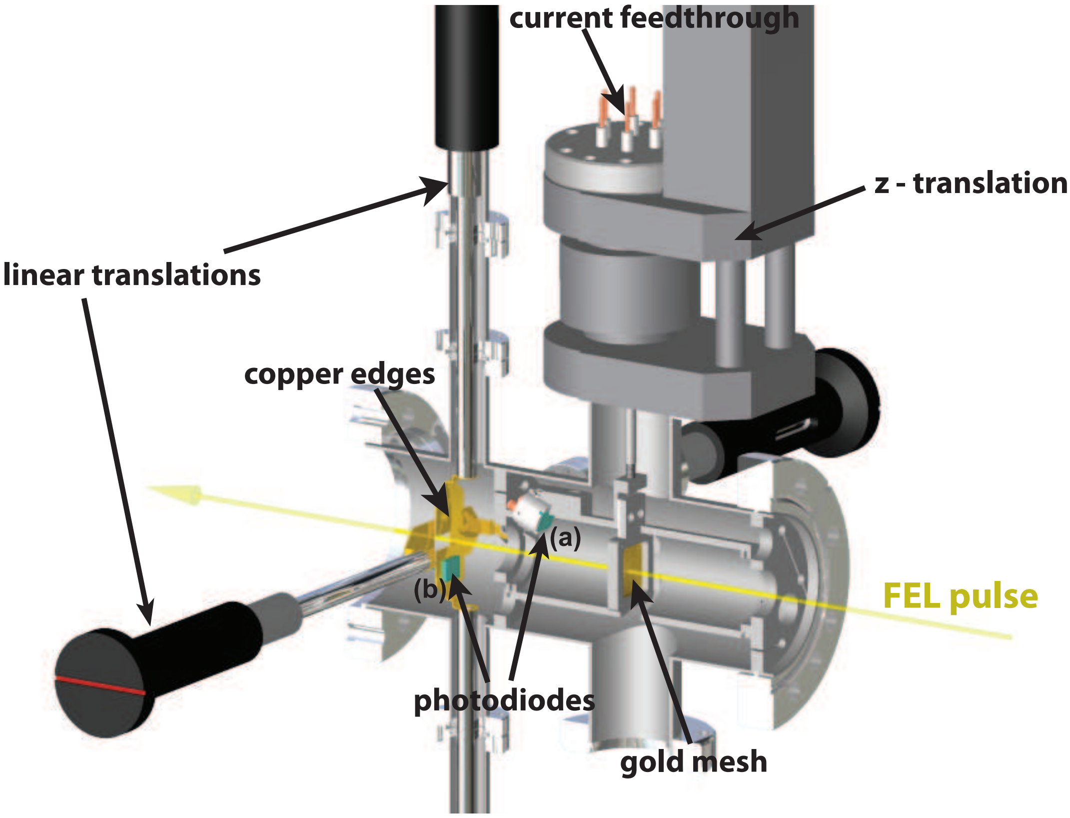

Figure 5.4: Illustration of the I–tube: The FEL radiation is crossing from right to left. A gold mesh and an attached photo diode (a) are measuring the photon pulse intensity online and in a non–destructive way. In order to calibrate those, a second photodiode (b) can be transferred directly into the beam. Four copper edges at the end of the tube prevent the electric fields of the I–tube (due to biasing of the gold mesh or photodiodes) from entering the experimental chamber and measure the beam position.

5.2 Tools for generating spatial and temporal overlap of IR–laser and FEL radiation

In order to perform time–resolved pump–probe experiments on solid state surfaces, two major requirements must be fulfilled. These are the spatial and the temporal overlap of the pump and the probe pulse on the sample surface. For this purpose two experimental setups have been developed.

5.2.1 Collinear injection of an optical laser into the FEL radiation path

The parallel injection of an additional pulsed optical laser (λ = 800 nm) into the path of the FEL beam was realized in collaboration with the research group of Wurth *et al.* from the University of Hamburg, Germany. Figure 5.5 illustrates its principle setup. The entire system is attached to a granite block to prevent disturbing oscillations.

At monochromator beamline PG2 the optical laser is provided about 1 m to the left and 1 m below the FEL beam line. Two vertically arranged optical breadboards are assembled with a set of lenses and optical elements for focusing the optical laser onto the sample surface. Between the first two lenses on the horizontal breadboard, an option for the generation of second harmonic radiation (λ = 400 nm) via a non–linear crystal is provided. Behind those, the laser beam is reflected by a partially transmitting mirror in perpendicular direction towards the "mirror chamber". Behind the partially transmitting mirror, a photo diode is installed for reference intensity measurements. With two more lenses on the vertical breadboard the focal distance with regard to the sample position can be adjusted. An optical filter wheel can be used in order to vary the laser pulse intensity by several orders of magnitude.

The converging laser beam is entering the mirror chamber through a silica glass window, where it is subsequently injected collinearly into the FEL beam (inset of figure 5.5). Two mirrors – one mirror for 800 nm and the other for 400 nm laser radiation – can be transferred into the laser beam via a linear transfer system in x–direction. An aperture between both mirrors serves for experiments without an additional optical laser. Both mirrors contain a 2 mm hole in the center in order to let the FEL radiation pass through. Three more degrees of freedom of the whole mirror chamber are implemented. These are two rotational degrees of freedom around the x– and z–axis, performed by two goniometers (Huber-Goniometer), and one linear translation in z–direction. Finally, the adjustment of the spatial overlap of FEL and optical laser is done by using a GaAs sample in the measurement position. Both, the FEL radiation and the optical laser are visualized on the GaAs surface due to photo luminescence. These spots are filmed with two high–speed cameras for three–dimensional orientation and can be adjusted on the same spot by using the two rotational and two translational degrees of freedom of the mirror chamber.

In the meantime, this system was used during different beamtimes at FLASH for time–resolved experiments [4,94], and the horizontal breadboard was additionally equipped with a delay stage providing a total delay time of 650 ps with an accuracy of 3 fs.

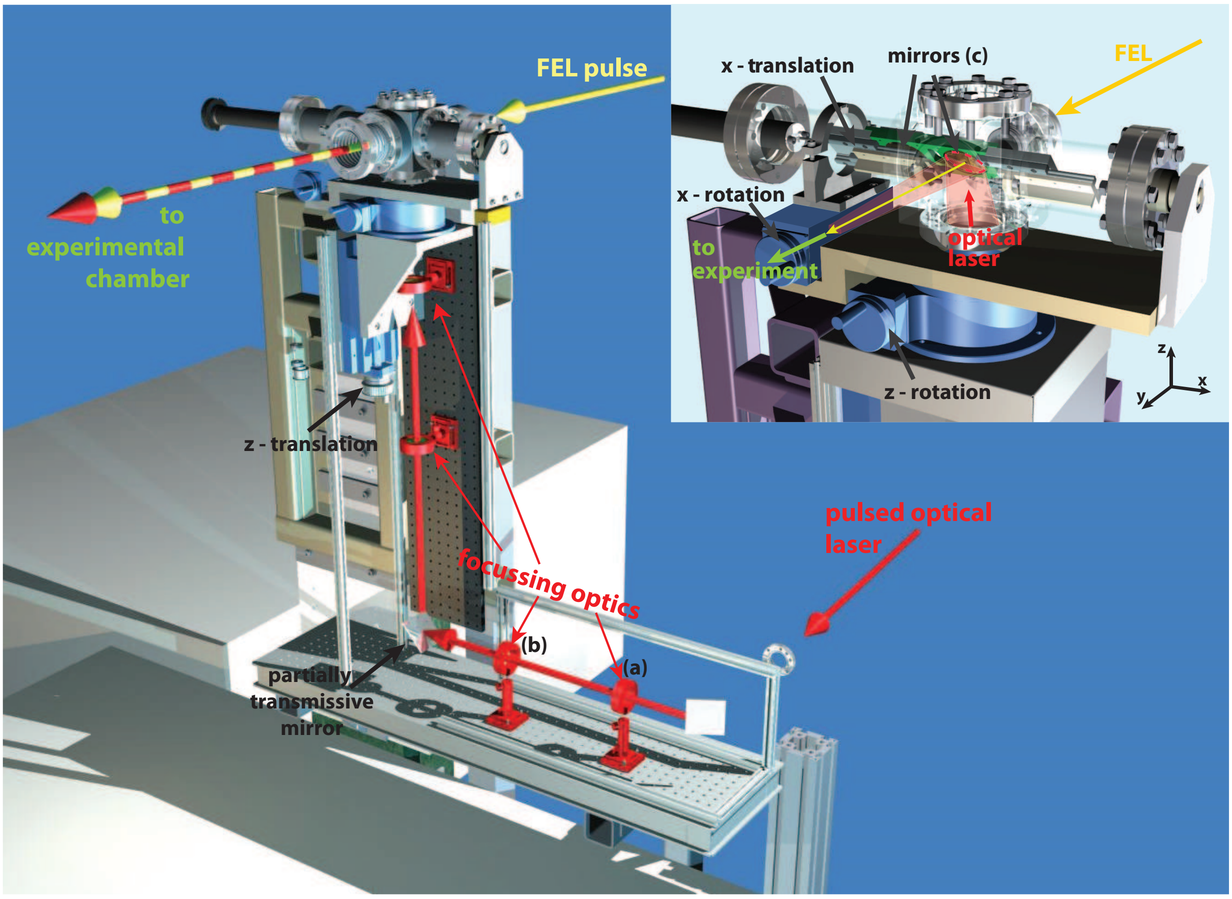

Figure 5.5: Setup for collinear injection of an optical laser pulse into the FEL radiation path: The first two lenses (a) and (b) on the horizontal optical bread board widen the optical laser with a wavelength of 800 nm (red). In the focus between both lenses an option for frequency doubling via a non–linear crystal is provided. A partially transmissive mirror reflects the laser radiation towards the vertical bread board, where two more lenses and one optical filter wheel are focusing the radiation onto the sample position and attenuate it up to several orders of magnitude, respectively. The laser radiation is finally reflected by a special mirror (c) with a 2 mm hole (for passing of the FEL beam) parallel to the FEL radiation. The inset shows the mirror chamber in more detail with several degrees of motional freedom in order to realize spatial overlap of both radiation beams on the surface.

5.2.2 Timing–tool for spatial and temporal overlap

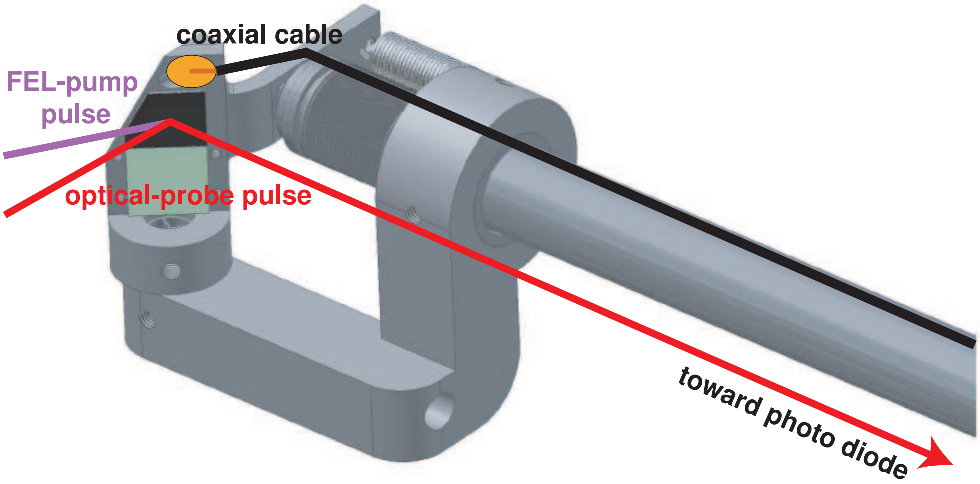

Figure 5.6: Illustration of the Timing–tool used for determination of the temporal overlap of optical pump and FEL probe pulse in time–resolved PES experiments (from [95]): The blank inner core of a coaxial cable is used in order to get a rough estimate of the temporal overlap by measuring the generated photo current. Then, the GaAs–crystal and its fast dynamics in the reflectivity (see [96], and Fig. 5.7) is used for a finer adjustment with an accuracy of a few femtoseconds.

In order to produce temporal overlap of the FEL pulses and the optical laser pulses, Wurth *et al.* developed a femtosecond X–ray/optical cross–correlator, the so called timing–tool, for time–resolved experiments at FLASH. In this device, the change in the reflectivity of a GaAs surface as a result of excitation with an intense EUV–pulse is utilized [96].
Figure 5.6 shows the main part of the timing–tool which can be moved into the sample position. To get a rough estimate of the temporal overlap, the spatially overlapping beams are at first focused onto the blank inner core of a coaxial cable. The cable is biased in order to guarantee the emission of photoelectrons due to the optical laser pulse ($h\nu \approx 1.5$ eV). The photocurrents of both pulsed beams are monitored with an oscilloscope, and by varying the delay a temporal overlap with an accuracy of some ten picoseconds can be achieved. In the next step, a GaAs sample is moved into the focus of the two beams. The fast dynamics in the optical reflectivity of a GaAs surface as a function of the delay between EUV–pump pulse and infrared–probe pulse can be used to achieve a considerably finer adjustment of the temporal overlap.

The intensity of the optical probe pulse is measured with photo diodes at two positions. The reference intensity is measured behind the partially transparent mirror of the collinear injection setup. The detection of the reflected optical laser pulse takes place behind a window of the UHV main chamber. During the procedure of finding the temporal overlap, the optical laser is operated with twice the repetition rate of the FEL (normally with 500 kHz). Thus, in the case of overlapping pulses one unaffected and one influenced reflectivity signal is subsequently measured, assuming that the excitation of the FEL pulse is already decayed within 2 μs.

The relative change in reflectivity of the pumped GaAs surface can be determined by $I_p = I^p_{D1}/I^p_{D2}$, where I^p_{D1} and I^p_{D2} are the signals of the reference diode and the diode

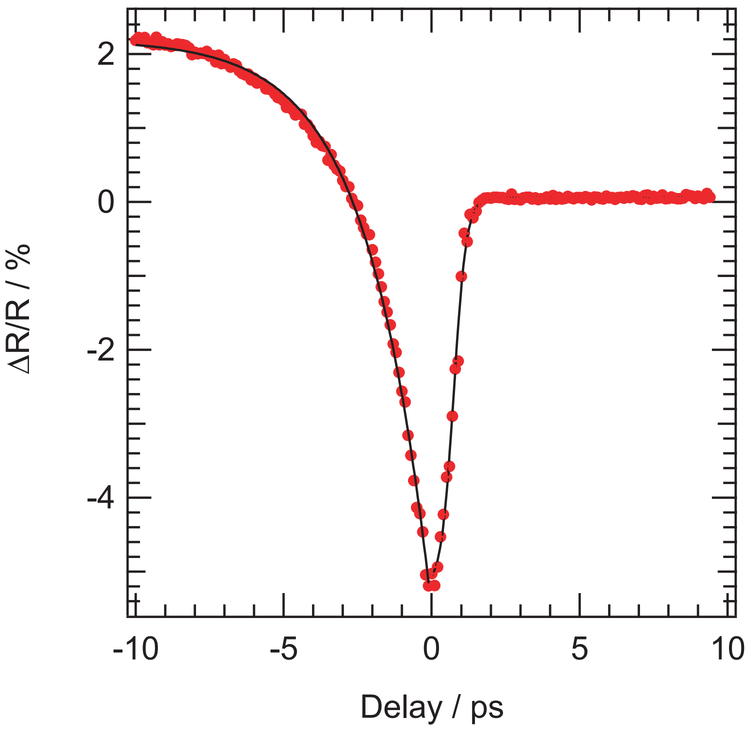

Figure 5.7: Reflectivity change of a GaAs–crystal in the timing–tool: The incident soft X–ray pulse of the FEL (50 eV, 120 fs) is changing the reflectivity of the crystal. The reflectivity of the crystal is measured by a photo diode as a function of delay between FEL and optical laser pulse ($\Delta t = t_{FEL} - t_{laser}$) measured with a streak camera [35].

measuring the reflected signal, respectively. Analog, the relative change in reflectivity for the unpumped crystal can be calculated by $I_u = I^u_{D1}/I^u_{D2}$. The resulting change in the reflectivity $\Delta R/R$ at a specific delay $\Delta t = t_{FEL} - t_{laser}$ is derived by:

$$\Delta R/R(\Delta t) = \frac{I_p - I_u}{I_u} \quad . \tag{5.6}$$

Via successive variation of the delay, the temporal overlap of optical laser pulse and FEL pulse can be determined with an accuracy of a few femtoseconds [96]. Figure 5.7 exemplarily shows the identification of the temporal overlap of an FEL–pulse (50 eV, 150 fs) and an optical laser pulse (1.55 eV, 120 fs) using the described procedure [35].

5.3 Experimental setups for intensity dependent PES at FLASH

The presented measurements of photoelectron spectra as a function FEL pulse intensity presented in chapter 7 were carried out during two beamtimes in the years 2005 and 2007 using two different experimental setups. These two experimental setups as well as the data acquisition will be presented in the following.

5.3.1 Setup for valence–band PES on $TiTe_2$

In 2005, first PES experiments at FLASH were carried out using an ultra–high vacuum (UHV) experimental chamber with a base pressure of $\approx 10^{-10}$ mbar. Cleaved TMDC samples in the UHV remained free from contaminants for several hours. The sample movement was realized with a standard manipulator with three translational and one rotational (around the perpendicular axis) degrees of freedom. Cooling of the sample was not possible. The adjustment of the UHV chamber with respect to the FEL beam was done by using a phosphorous screen with a cross hair in the direction of the beam.

The sample was electrically insulated to the grounded manipulator but contacted with an electrical feedthrough, where the generated sample current could be measured. The sample current signal was amplified with a Femto DHPCA–100 ultrafast current–to–voltage converter and stored as a direct measure for the FEL pulse intensity. This was necessary due to the absence of a calibrated intensity monitoring system behind the monochromator at beamline PG2 at this time.

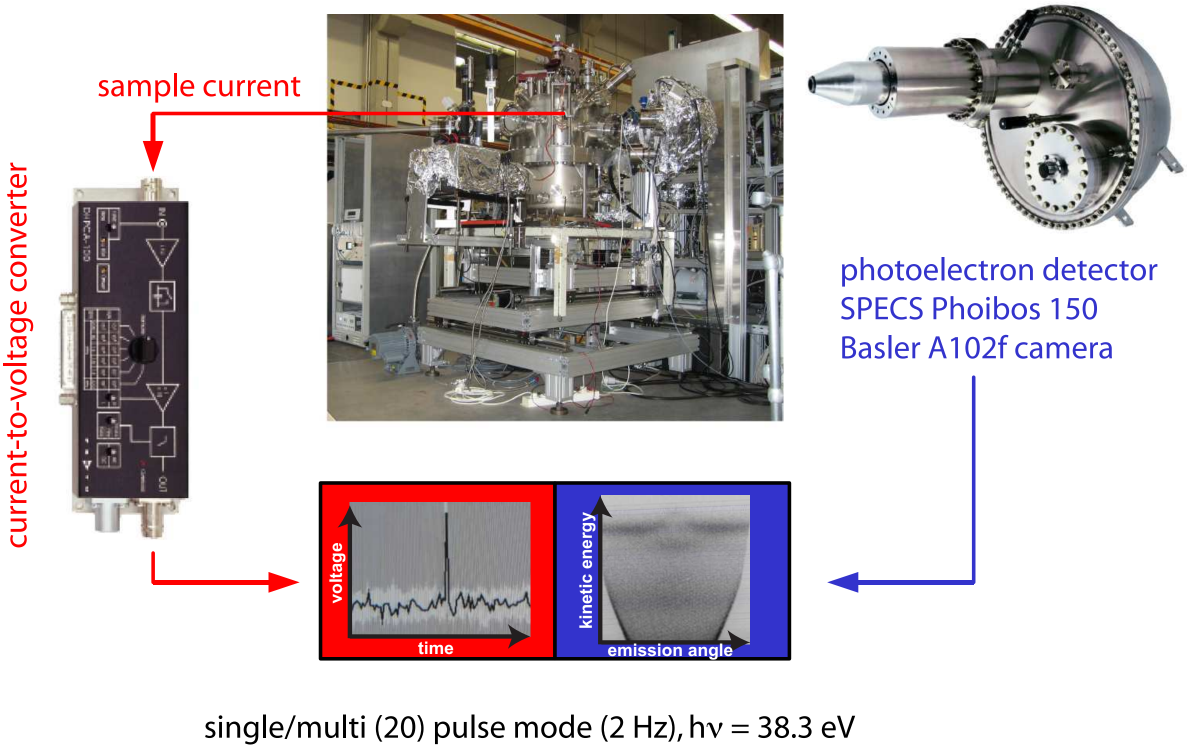

Figure 5.8: Experimental setup for first pulse–intensity dependent valence–band PES measurements at FLASH beamline PG2. The spectra and pulse intensities were measured via a SPECS Phoibos 150 photoelectron analyzer and the amplified (Femto DHCPA–100) sample current, respectively (from [97])

.

The angle and energy resolved PES data were measured with a hemispherical photoelectron analyzer (SPECS Phoibos 150) with a CCD–detector in the exit plane. At best, this analyzer can achieve an angular resolution of 0.05° and an energy resolution of ≈ 1 meV.

A wide–angle detection of ±13° in parallel is possible. The detector images were recorded with a Basler A102f 2D–CCD camera triggered by a TTL–signal delivered from the FEL machine.

The valence band photoemission data of the transition metal dichalcogenide $TiTe_2$ presented in chapter 7 were measured with an energy resolution of < 700 meV (E_{pass} = 200 eV, s_{ana} = 1 mm) using the wide–angle lense–mode. The FEL delivered VUV–radiation with a photon energy of 38.32 eV in the first harmonic with a repetition rate of 2 Hz. To get decent statistics in the resulting spectra, the FEL was run in the multi–pulse mode with 20 single pulses in one pulse train separated by 1 μs accepting the consequence of fluctuating intensity. In order to perform angle–resolved photoemission as a function of pulse intensity, the incident pulse–energy was tuned by varying the monochromator exit slit. The measured sample current and the taken CCD–images as well as every other relevant FEL–machine parameter were stored via the provided machine–control system DOOCS[3].

5.3.2 Setup for pulse intensity dependent core–level PES on 1*T*–TaS_2

The experimental setup for the core–level measurements presented in chapter 7 is summarized in figure 5.9. Again, a SPECS Phoibos 150 electron analyzer with a CCD–detector was used. The detector images were recorded with a PCO Sensicam qe CCD camera. Due to a cooled CCD–chip, this camera had a better signal–to–noise ratio than the previously used Basler camera.

A completely new experimental chamber was used with a base pressure of $\leq 10^{-10}$ mbar. The TMDC samples were adjusted to the measurement position via a new manipulator cryostat, a VG Cryoax 6. With this, all six motional degrees of freedom were possible to access within a limited extent. The samples could be cooled down to a minimum temperature of 30 K. Here, the pulse intensity measurements were done with the MCP–detector and the first version of the home built I–tube, monitoring the photo current generated in a high–transparent gold–plated copper mesh (T = 88 %, nominal aperture of 200 μm, Goodfellow GmbH). This was amplified with a Femto DHPCA–100 ultrafast current–to–voltage converter and measured by a digital storage oscilloscope LeCroy WaveRunner 6030A.

In contrast to the experimental setup in 2005, here, the main chamber was extended by an additional peripheral equipment connected to the main chamber by a transfer system under UHV conditions. With this, one was able to perform further sample characterization with an additional LEED system (low energy electron diffraction) for sample orientation. A He–gas discharge lamp (SPECS UVS–300) with a toroidal–mirror monochromator (SPECS TMM 302) was connected to the main chamber and delivered VUV–radiation with a photon energy of 21.22 eV. The incident angle of the VUV–radiation was the same as of the FEL radiation with respect to the analyzer. A special capillary (SPECS Surface Nano Analysis GmbH) focused this radiation to a nominal spot size of a few 100 μm at the measurement position. The photoemission measurements with the He–gas discharge lamp

---

[3] DOOCS is the abbreviation for distributed object control system [98]. It has been developed as a control system for the FEL as well as the planned XFEL in Hamburg, Germany. Furthermore, this control system is specialized in the acquisition and storage of the huge amount of generated data. These as well as several automatically collected operating parameters are stored in so–called root–files[4].

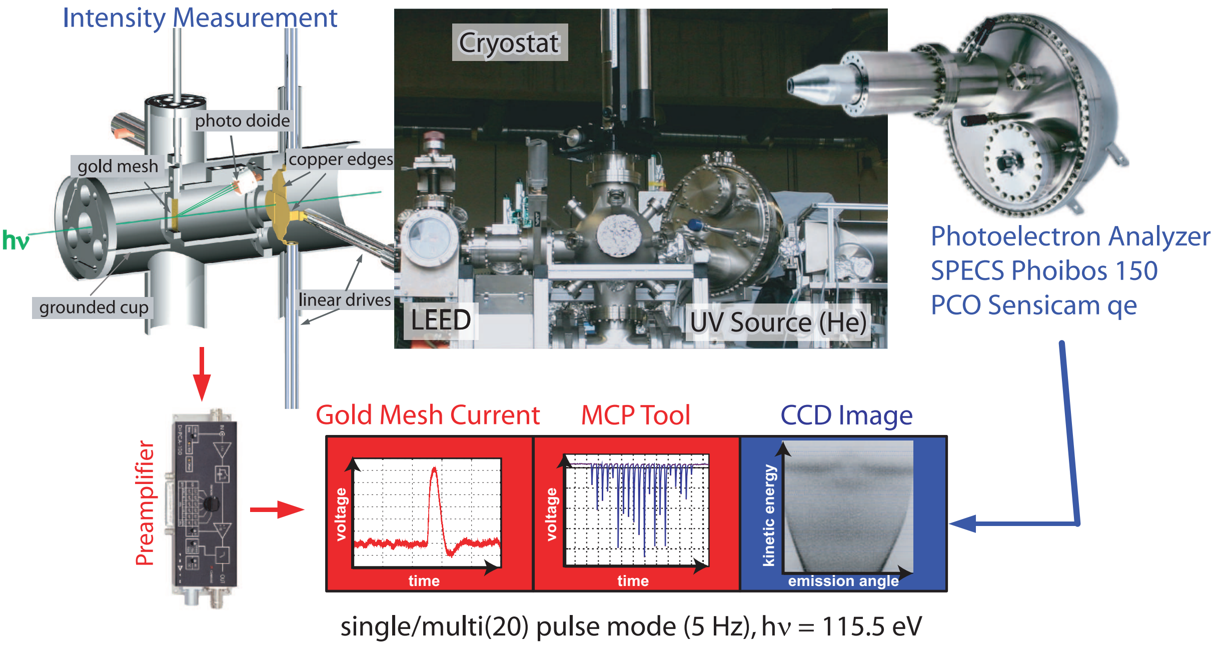

Figure 5.9: Experimental setup for photoelectron spectroscopy at FLASH beamline PG2 with main components: photoelectron analyzer with 2D–CCD detector, Cryostat, LEED, home built pulse–intensity measurement tool with preamplifier. Photon pulse intensities were measured by gold mesh current in the I–tube (see subsection 5.1.3) as well as with an MCP based tool (see subsection 5.1.2).

served as a reference representing PE measurements with a constantly strong electron signal and below the regime of SCEs.

Data acquisition was done in two parts. On the one hand, all relevant FEL parameters as well as the pulse intensity monitoring with the MCP detector were stored via DOOCS. The data were, again, stored in root–files, where each pulse train was marked with a unique 24–bit–timestamp. The first twenty bits stand for the current time in seconds, while the last four bits are used for a specific bunch number due to the fact that the FEL can be run with maximum repetition rate of 10 Hz. On the other hand, we built up a stand–alone–system were the measured sample gold mesh current as well as the images from the CCD–camera are recorded with the own measurement PC. Again, these data were stored with the reference 24–bit–timestamp delivered by the FEL machine. For this purpose the measurement PC was equipped with a PCI–card (NI PCI–6503) containing 24 digital I/O channels.

The measurement with the stand–alone–system was done as follows: The exposure of the CCD–camera as well as the acquisition of the oscilloscope were triggered by the FEL with the repetition rate of 5 Hz. The resulting CCD–image was transferred from the camera to the measurement PC. After the transfer of the image, the timestamp was read out and inquired by the oscilloscope. The measured gold mesh current and the CCD–image were stored on the measurement PC with this characteristic timestamp. Further details of the data acquisition software can be found in reference [93].

The following parameters were used for the core–level PES measurement as a function of the average pulse intensity presented in chapter 7. The FEL delivered VUV–radiation with a photon energy of 38.5 eV in the first harmonic and a repetition rate of 5 Hz.

Each pulse train consisted of 20 single pulses separated by 1 μs. For the measurement of the Ta 4*f* core levels the third harmonic was used with a photon energy of 115.5 eV and significantly lower pulse intensities. Further variation of the pulse intensity was done by varying the monochromator exit slit and using the gas absorber system behind the FEL undulator. The pulse duration was approximately 700 fs [100] limited by the plane grating monochromator. The photoelectron analyzer was run in the wide–angle lens mode and an energy resolution of better than 140 meV (E_{pass} =200 eV, s_{ana} = 0.2 mm) was achieved. The TaS_2 sample was cooled down to 140 K and has, therefore, reached the Mott–insulating phase.

5.3.3 Setup for time–resolved PES on 1*T*–TaS_2

In 2008, we carried out first time–resolved PES experiments on the TMDC TaS_2. For those, the HIXXS experimental chamber from the research group of Wurth *et al.* from the University in Hamburg was used. The principle setup is illustrated in figure 5.10. The UHV system consists of two main chambers. The first chamber next to the beamline is equipped with a SCIENTA SES 2002 photoelectron analyzer with a CCD detector in the exit plane and a Basler camera A102f taking images of the phosphorous screen with the repetition rate of the FEL. Furthermore, an X–ray spectrometer was part of this experimental chamber allowing for RIXS (resonant inelastic X–ray scattering) measurements. The timing–tool (see section 5.2.2) for finding the temporal overlap between pump and probe pulse was attached to an extra long manipulator for positioning into the sample position. Due to this extra long travers path the timing tool could be decoupled from the main chamber via an UHV valve. The whole chamber with all devices was rotatable around the sample position. The second chamber served as a load lock as well as for locking in and manipulation of the samples. The TaS_2 samples could be transferred into the measurement position within the first chamber via a long manipulator cryostat. With this, sample cooling down to 30 K with liquid Helium was achievable.

The system for collinear injection of the pulsed optical laser (λ =800 nm) (see section 5.2.1) and adjustment of the spatial overlap between pump and probe pulse was installed between the first experimental chamber and the beamline. The delay between both was set by a delay stage and measured with a streak camera installed in the FEL laser hutch. The delay was remote controlled via the FLASH control system. All relevant data were stored as root–files via DOOCS.

The following parameters were used during the first TRPES–measurements in 2008: The FEL delivered pulse trains containing 100 single pulses temporally separated by 2 μs and a repetition rate of 5 Hz. The fundamental wavelength was set to 7 nm and the single pulse duration in the first order of the monochromator was approximately 1.2 ps. The average pulse energy of $\approx 20\mu$J/pulse was attenuated with filter foils by about four orders of magnitude in order to prevent SCE induced spectral changes in the photoemission data. The energy resolution of the photoelectron analyzer was set to $\approx$ 100 meV (E_{pass} =50 eV, s_{ana} = 1.2 mm) and the "transmission mode" (no parallel detection of the emission angle) for high PES contrast was used. The optical laser was run in the "burst mode" delivering pulse trains containing 200 single pulses separated by 1 μs and with maximal single pulse energies of 14μJ/pulse (without considering losses within the optical path). The optical laser was focused to a spot size on the sample of 1.5 mm × 1.5 mm resulting in an incident

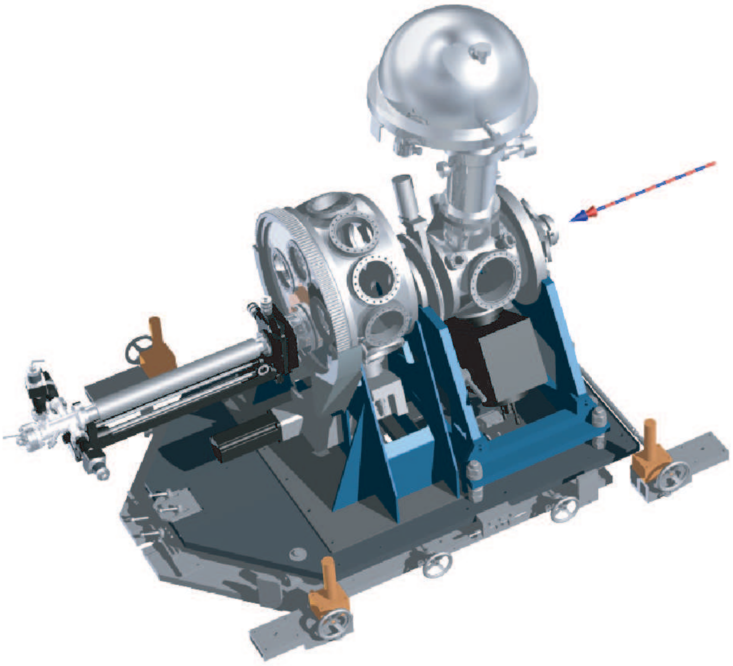

Figure 5.10: Experimental chamber for time–resolved core–level photoelectron spectroscopy at FLASH beamline PG2: The HIXXS experimental chamber from the research group of Wurth et al. from the University in Hamburg was used, additionally equipped with the timing–tool from section 5.2.2 and the setup for collinear injection of the optical laser from section 5.2.1 placed in front of the chamber.

energy density of $\approx$ $600\mu J/cm^2$ within a pulse duration of 150 fs. This, approximately, corresponded to the limit of $200\mu J/cm^2$ within a 50 fs–pulse, leading to a irreversible phase transition of the TaS_2 surface [56].
With the pulse duration of the FEL (1.2 ps), the temporal resolution of the streak camera (1 ps) and the temporal jitter of the single pulses within one pulse train (500 fs) a total temporal resolution of the experiment was determined to be ≈ 1.6 ps.
In order to reach the Mott–insulating phase, the TaS_2 samples were cooled with liquid Nitrogen via the cryostat.

6 Vacuum space–charge effect in solid–state photoemission

6.1 Introduction

For probing electronic states in atoms, molecules or solids, modern photoemission techniques are very efficient. One powerful example is angle–resolved photoelectron spectroscopy (ARPES). This method serves typically for determining the electronic structure and, in particular, the Fermi surface of solids, e. g., searching for indications of many–body effects identifiable in opening gaps or kinks in the band dispersion. Beyond that, the development of pulsed photon sources with ultrashort pulse lengths attracts the attention towards measuring dynamical non–equilibrium processes in the electronic structure via time–resolved photoemission spectroscopy (TRPES). Furthermore, the possibility of focusing brilliant light sources in the soft X–ray regime to the submicrometer range enables photoemission spectromicroscopy for spatially resolved investigations of solid surfaces.

To further promote these photoemission methods, improvements on the instrumentation side is essential. On the one hand this was achieved by the development of very efficient photoelectron analyzers (now able to simultaneously measure a distinct energy and angle range in parallel) delivering an energy and angular resolution of < 1 meV and < 0.05 °, respectively. On the other hand and for this chapter of major interest are the enhancements of the photon source. Modern third–generation synchrotron–radiation sources generate short (some 10 ps) photon pulses with high spectral brightness in the extreme ultraviolet (EUV) and soft X–ray regime by using undulators. Photon pulses with even shorter pulse lengths (a few fs) in the UV to EUV regime can be achieved in the laboratory with ultrafast laser systems employing high–harmonic generation (HHG). Using such short–pulsed photon sources in photoemission experiments can lead (at todays achievable energy resolution) to spectral shifts and broadenings in the photoemission spectrum, the so–called vacuum space–charge effect (SCE). Here, photoelectrons are emitted from the solid within a relatively short timescale producing an electron cloud with a high electron density in front of the surface. According to the intensity of the photon pulse and, thus, the number of emitted electrons in the cloud, those are mutually influencing each other by repulsive Coulomb forces on their way to the detector. Finally, this process leads to a broadening and shift of the initially emitted electron–energy and angular distribution worsening the effective experimental energy and angular resolution. Vacuum space–charge effects, resulting in an energy broadening and shift of an initial spectral feature in the order of ≈ 10 meV have already been studied at a conventional third–generation synchrotron–radiation source delivering $\approx 10^4$ photons within pulse lengths of ≈ 50 ps [22]. This is a clear signal, that in future experiments at even more intense photon sources, the instrumentally achievable resolution will not be the only limiting factor any more.

In terms of UV and X–ray sources, the development is still going on towards higher peak brilliance (see chapter 4) causing SCEs in photoemission to be even more relevant. Particularly, the enhancements in upconversion techniques like HHG and the construction of free–electron lasers (FELs) (also declared as fourth–generation synchrotron–radiation source) pave the way for time–resolved core level PES in the fs–regime; but with photon densities of $> 10^7$ within a short pulse, SCEs will lead to energetic broadening and shift in the eV regime, making the interpretation of the measured spectra very difficult.

Therefore, performing photoemission experiments at such brilliant light sources make a precise understanding or, at least, a sufficiently accurate description of SCEs influencing the photoemission spectrum very important and the question arises: Where are the SCE–inflicted limits in PES with regard to photon source parameters? There is an extensive literature dealing with this topic for years, e.g., in thermal electron emission, ultrafast electron diffraction [101–105], photoemission microscopy [106], as well as several works on (TR)PES using photon pulse in the ps and fs range [22–24, 107–111]. SCEs are very sensitive with regard to the initial electron distribution in momentum and real space and, therefore, in PES mainly on the parameters of the photon source, such as intensity, spot size, pulse duration and photon energy. In addition to those, material specific parameters will contribute to the initial electron distribution. At least, parameters like intensity, spot size, pulse duration and photon energy can vary by orders of magnitude, depending on the used photon source, and consequently, the extremely differing starting parameters are causing a strong variation in the observed SCEs. In the recent past, different groups have described the influence of space–charges on the initial electron–energy distribution by simple numerical simulations or simple analytical models with quite some success. Though, these have mainly been successful within their experiment specific parameters, but are not universally applicable. Thus, in some cases the spectral broadening is found to be proportional to the square root of the number of photoemitted electrons per pulse [23, 105], while other groups have reported a linear functional dependence [22, 24]. Therefore, a variety of questions concerning SCEs are still not satisfyingly solved, i.e. beside the dependence of the spectral broadening and shift as a function of photoelectrons, the possible influence of mirror charge (at least for metallic surfaces), as well as the question of the influence of SCEs on the angular resolution. A clear restriction on a valid parameter range for the used simulations or models is still missing as well as an easy rule of thumb providing assistance in future PES experiments, where SCEs may occur. This will be given in the following as well as in [25].

In the following, the influence of SCEs on the photoemission spectrum as a function of the source parameters will systematically be examined in a more universal manner and as realistic as possible. For this purpose a molecular–dynamical model for numerical simulations of N–body problems is introduced. Here, the propagation dynamics of the electrons on their way from the surface to the detector is followed, and the influences of several parameters on the initial electron–energy distribution are studied in detail with relatively short simulation times. The parameters are chosen to reproduce the ones of typical pulsed photon sources used for photoemission experiments. To get an idea of the applicability of this numerical approach, the simulations are tested for three chosen experimental parameters from the literature, where SCEs are studied under extremely different source parameters, and the results are compared with the experimental ones. Furthermore, the simulations are done for a wide range of the most relevant parameters to find a functional dependency of the space–charge induced energetic broadening and shift of the photoemission spectra as well as the influence on the angular resolution. Two simple analytic models are compared with the gained results and the area of validity of those models is proven. Finally, the delivered insight into SCEs in PES will be discussed in terms of future photoemission experiments at modern pulsed light sources.

6.2 Computational model

The solid–state photoemission process using a pulsed photon source is schematically illustrated in figure 6.1. The incident photon pulse is absorbed by the electrons in the sample. Electrons will leave the sample in case of having enough energy at the surface to overcome the vacuum level. An electron cloud is successively created in front of the sample surface within the pulse duration. The photoelectrons in this cloud have specific distributions in the six–dimensional phase space (three–dimensional distributions in the real and momentum space), that are dependent on several parameters. These are (on the instrumentation side) the number of photons per pulse, the pulse duration, the spot size on the sample surface and the photon energy as well as some material dependent aspects influencing the photoemission process like the quantum efficiency and the kinetic–energy and emission–angle distribution. The electrons in the cloud are interacting with each other due to their electric charge after the Coulomb's law. Here, the total force $\vec{F_i}$ on the i^{th} electron is calculated by the following relation:

$$\vec{F_i}(t) = \sum_{j=1, j\neq i}^{N_C} \frac{e_0^2(\vec{r_i}(t) - \vec{r_j}(t))}{4\pi\epsilon_0 \left|\vec{r_i}(t) - \vec{r_j}(t)\right|^3} , \tag{6.1}$$

where N_C is the number of electrons in the cloud, e_0 the unit charge, ϵ_0 the vacuum permittivity and $\vec{r_i}(t)$ the time–dependent position vector of the i^{th} electron. Therefore, the electrostatic forces on the electrons will be stronger the more electrons contribute to the cloud, in turn resulting in more pronounced SCEs in the photoemission experiment.

In our numerical simulations of SCEs the electron cloud is built up gradually in discrete time steps Δt during the interaction time of the photon pulse with the sample surface. The electrons are emitted from random position and random time defined by the two–dimensional spot profile and temporal pulse profile, respectively. The random kinetic energies and the emission angles of the photoelectrons are generated by using specific distributions somehow determined experimentally or considered theoretically. For the temporal as well as the lateral pulse profiles, Gaussian distributions with widths of τ_0 and d_0 (full width at half maximum (FWHM)) are assumed, respectively. Furthermore, in the numerical simulations presented in this chapter, the number of electron N_C are varied ranging from 4 to 5 × 10^6 per pulse.

To calculate the mutual Coulomb interactions of the propagating cloud electrons, we performed self–consistent N–body numerical simulations using the so–called "Barnes & Hut Treecode Algorithm". This algorithm was originally developed to simulate planetary motions or collisions of galaxies. Here, in each time step the current position and velocity of the electrons as well as the effective Coulomb forces are calculated. For the numerical integration of the differential equations of motion the leapfrog method [112] is used. The leapfrog integration is a second order method and, therefore, more accurate than the first order Euler integration. Furthermore, it is time–invariant and consequently assures energy conservation. The basic principle and efficiency of the Treecode Algorithm lies in the way to calculate the Coulomb forces on each single electron. Here, the space occupied by the cloud electrons is iteratively divided into a hierarchical tree structure and center–of–mass approximations are performed. Figure 6.2 will help to understand this principle in more detail. In figure 6.2(a) the propagation of the photoelectrons (blue dots) from the sample to the detector at a specific time is illustrated. In the first step of creating the hierarchical

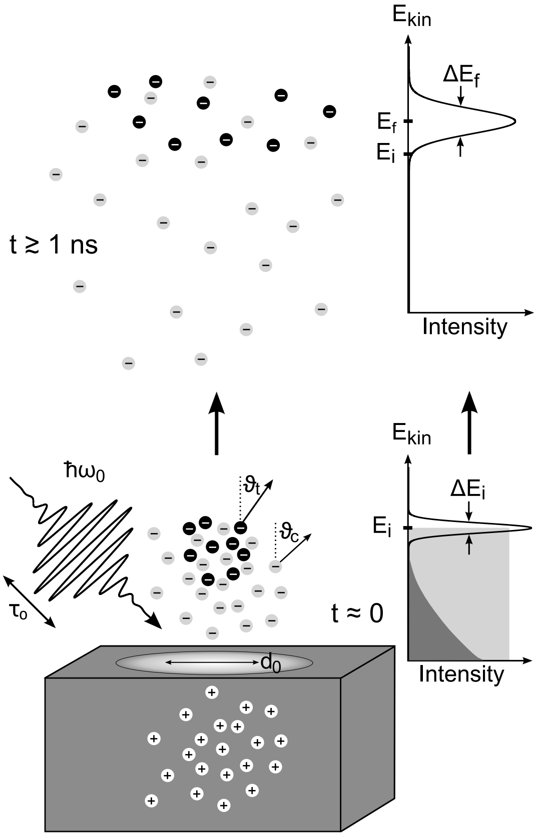

Figure 6.1: Schematic of a solid–state employing a pulsed photon source. A light pulse with energy $\hbar\omega_0$ and duration τ_0 impinges on the surface area of characteristic width d_0 and creates photoelectrons. In the numerical simulations, the photoelectrons are divided into cloud electrons (gray dots) and test electrons (black dots), both having specified initial kinetic energy (E_{kin}) and emission angle (ϑ_c, ϑ_t) distributions depending on the source parameters and sample properties. For the test electrons, a sharp Gaussian energy distribution (mean position E_i and width ΔE_i) is typically selected. The gray energy areas in the energy spectrum depict simple energy distributions for the cloud electrons. Positive mirror charges in the bulk of the sample (white dots) are generally included in the simulation. The propagation of the electrons toward the detector is influenced by mutual Coulomb interaction. After about 1 ns, when the total Coulomb energy has become negligible, the final energy spectrum of the test electrons is obtained. In general, it will be shifted and broadened with respect to the original spectrum ($E_f \neq E_i, \Delta E_f > \Delta E_i$). (from Ref. [25])

tree structure, the "root cell" (violet cube), framing the whole relevant space, is divided into eight subcells. Each of the subcells is related to a center of mass determined by the containing electrons. If these subcells contain more than one electron the subdivision is continued until each generated cell is filled by one electron at most. For a better visualization, in figure 6.2(a) only the root cell and the subcells containing one electron (the "leafs" of the tree structure) are plotted. Figures 6.2(b) and (c) illustrate the efficient force calculation of the Treecode Algorithm by means of a simplified two–dimensional electron cloud. In this case, all subcells of the hierarchical tree structure are plotted in figure 6.2(b) as well as 17 electrons (blue dots). The total force on the red marked electron (cf. figure 6.2(c)) is to be calculated in this example. For this, a technical parameter called "opening angle θ" is introduced acting as an accuracy parameter. Considering the ratio of the width of one subcell s and the distance l between the relevant electron (red dot) and a center of mass of a subcell, the force calculation is carried out as follows, beginning with the subcells of the root cell:

1. If $\frac{s}{l} < \theta$: The partial force on the electron is calculated by approximating a point charge in the center of mass of the subcell, according to the number of containing electrons.

2. If $\frac{s}{l} \geq \theta$ and more than one electron in the subcell: No partial force is calculated. The eight subcells of the next level have to be taken into account for the calculation of the partial force and again condition 1 has to be checked for them.

3. If $\frac{s}{l} \geq \theta$ and one electron in the subcell: The partial force is calculated by the exact electron–electron interaction.

After calculating the partial forces these are summed up to the total acting force on the electron. In figure 6.2(c), $\theta = 1$ is used for the force calculation. Therefore, three center–of–mass approximations containing 10 electrons are applied as well as 6 exact force calculations for the residual electrons.

The runtime for exact numerical N–body simulations is proportional to $\mathcal{O}(N^2)$, and for very large numbers of particles it is not feasible any longer. Using the Treecode Algorithm for SCE simulations deliver results with reasonable accuracy and requires only $\mathcal{O}(NlogN)$ operations. Mean–field models, approximating the charge distributions to a field configuration and calculating the forces on each electron due to this field, even need less computational time ($\mathcal{O}(N)$), but are only suitable for simple configurations and, therefore, not universally applicable. Ref. [113] serves for more detailed information about the Treecode Algorithm concerning error and runtime analysis.

A typical simulation run ends, when the major part of the initial Coulomb energy in the electron cloud is transferred into the kinetic energy of the electrons. Usually, this is the case after a few ns, mainly dependent on initial electron density as well as the initial momentum distribution of the electrons. In the end, the final kinetic–energy and momentum distribution are determined. With simulation time steps of $\Delta t = 20\ ps$ and an accuracy parameter of $\theta \approx 1$ an energy conservation of better than 99.9 % is achieved in our simulations.

The numerical simulation of the propagating and space–charge influenced electrons is repeated several times to avoid falsified results due to initially inappropriate randomly generated starting conditions. To additionally increase the statistics, so–called test electrons are introduced in our simulations (typically $\approx 10^4$). These "virtual" electrons are generated in

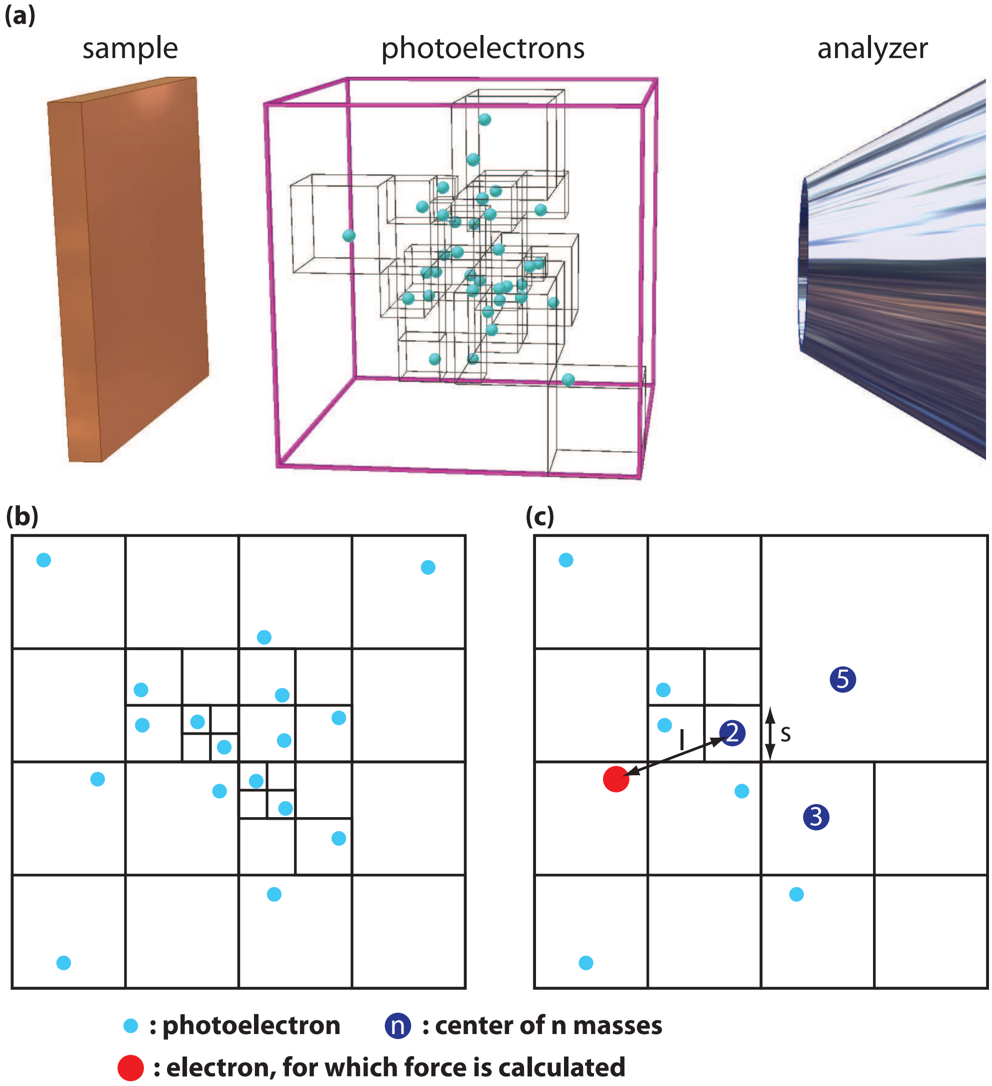

Figure 6.2: Illustration of the propagation of photoelectrons (light blue) from the sample surface to the photoelectron analyzer at a specific time (a), as well as visualization of the calculation of the total force on one single electron using the hierarchical Treecode Algorithm [26]. (a) The three–dimensional space occupied by the electrons is iteratively divided into subcells until each generated cell contains one electron at the most. For simplification only the root cell (magenta) and the subcells containing one electron are depicted. (b) Illustrates the hierarchical Treecode structure in two dimensions, and (c) exemplarily shows the calculation of the total force on the red marked electron due to the surrounding with the Treecode Algorithm. Here, direct electron–electron interactions (light blue) contribute to the total force as well as center–of–mass approximations (dark blue) in the case of a given opening angles $\theta > \frac{s}{l}$.

the same way as the other "real" cloud electrons, but generally with a narrower kinetic–energy and emission–angle distribution. The test electrons feel no mutual Coulomb forces and do not contribute to the force calculation of the cloud electrons, but they are influenced by the cloud electrons. Hence, the cloud electrons and their distributions in the phase space represent the whole amount of electrons generated in the photoemission experiment (incl. secondary electrons). However, the test electron distribution act as a specific part of the whole distribution (typically with a narrow Gaussian kinetic–energy distribution) propagating towards the detector (with a narrow emission–angle distribution). Finally, mainly the influence of the cloud electrons on the test electrons is analyzed and the spectral broadenings and shifts are quantified using the resulting test electron spectra.
For our general analysis of SCEs on photoemission spectra in sections 6.3 and 6.5 we used Gaussian shaped kinetic–energy distributions for the test electrons. In most cases the simulated final test electron spectra could be fitted by Gaussian profiles as well. Finally, the space–charge induced spectral shift ΔE_{shift} and broadening ΔE_{broad} are determined in the following way:

$$\Delta E_{shift} = E_f - E_i \tag{6.2}$$

$$\Delta E_{broad} = \sqrt{(\Delta E_f)^2 - (\Delta E_i)^2} \qquad , \tag{6.3}$$

where E_f and E_i are the final and initial mean energies and ΔE_f and ΔE_i the final and the initial FWHM width of the test electron energy spectrum. In the case, that a strongly distorted kinetic–energy distribution can not be fitted by a Gaussian profile any longer, the mean and the variance are used for the calculation of the energetic shift and broadening, respectively. Such distorted spectra will be presented in section 6.3. In some cases, the kinetic–energy gain of a few electrons exceed a multiple of the width of the final energetic spectrum caused by short–range interactions of the electrons in the cloud. The percentage of the whole amount of electrons normally does not exceed 0.1 % and can, thus, be neglected in the determination of ΔE_{shift} and ΔE_{broad}. The error of calculating E_f and ΔE_f using the Treecode Algorithm for the simulations of SCEs, we specify to be ≈ 10 %.
Finally, the influence of a metallic surface (at $z = 0$, where z indicates the direction perpendicular to the surface) can be considered in our numerical simulation of the propagation dynamics as well. On the one hand, back scattered electrons hitting the surface are immediately absorbed and do not contribute to the space charge any longer. On the other hand, a perfectly metallic surface has to be treated as an equipotential surface. This fact is considered in electrodynamic calculations by introducing virtual mirror charges. Here, each electron in front of the metallic surface with $\vec{r_i}$ = (x,y,z) creates a positive mirror charge inside the solid with $\vec{r'}_i$ = (x,y,-z). Mirror charges can be taken into account in our simulations. They are typically affecting the cloud and test electrons by attractive Coulomb forces and are, therefore, influencing the space–charge induced spectral shifts and broadenings. The influence of stationary created photoholes in nonconducting samples is not examined here.

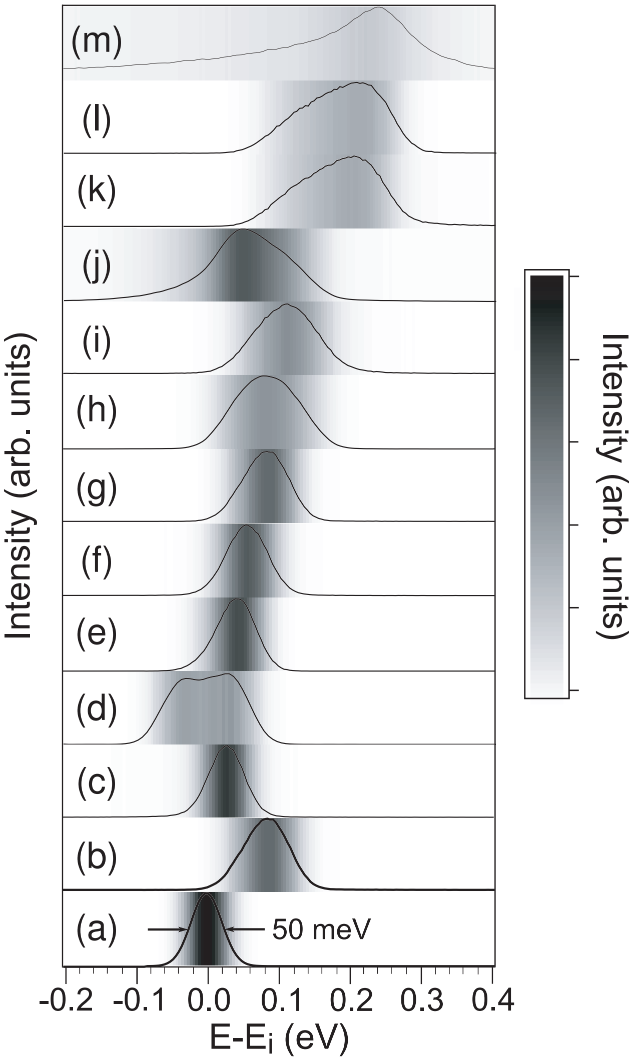

Figure 6.3: Influence of various simulation parameters on a Gaussian test electron spectrum with mean position E_i = 30 eV and ΔE_i = 50 meV FWHM [spectrum (a)]. The basic parameters of the numerical simulation, leading to spectrum (b), are number of cloud electrons per pulse $N_c = 10^4$, spot size diameter d_0 = 200 μm, pulse duration τ_0 = 50 fs, homogeneous energy and isotropic emission–angle distribution of the cloud electrons (E_c = 0–30 eV, ϑ_c = 0°–90°), normal test electron emission (ϑ_t = 0°), mutual Coulomb interactions between cloud electrons, and interactions with mirror charges included. Changing individual parameters results in the following spectra: (c) E_i = 15 eV; (d) τ_0 = 200 ps, and $N_c = 2\times10^4$; (e) τ_0 = 50 ps; (f) ϑ_t = 45°; (g) no Coulomb interaction between cloud electrons; (h)–(j) Gaussian cloud electron spectra with 50 meV FWHM and mean energies of 1, 30, and 900 eV; (k) no mirror charges; (l) ϑ_c = 0°–45°; and (m) d_0 = 50μm and Gaussian cloud electron spectrum with 50 meV FWHM and mean energy 30 eV (from Ref. [25]).

6.3 Relevant parameters

The results of our SCE simulations are dependent on several parameters. These are on the one hand technical parameters such as the opening angle θ, the simulation stepsize Δt and the simulation duration, and on the other hand the physical parameters with regard to the photoemission process. The technical parameters will not be discussed here, but they are treated in reference [114] in more detail. Typically, a timestep $\Delta t < 20$ ps and an opening angle $\theta = 1$ is chosen. Instead of the technical parameters, we present the influence of the initial phase–space distribution (directly dependent on the photon source and material parameters) of the cloud electrons on the photoemission spectrum in this section. For this, we start with an example, that may be representative for a photoemission experiment using a short–pulsed photon source delivering monochromatic VUV light. The illuminated area on the surface is circular shaped with a FWHM width of $d_0 = 200$ μm. The pulse duration is $\tau = 50$ fs and $N_C = 10^4$ cloud electrons are emitted from the sample within this time. The test electrons are emitted in normal direction ($\vartheta_t = 0°$) with a Gaussian kinetic–energy distribution with a mean energy of $E_i = 30$ eV and a FWHM width of $\Delta E_i = 50$ meV. The cloud electrons on the other hand leave the sample isotropically ($\vartheta_C = 0°...90°$) and with a rectangular kinetic–energy distribution in the interval from $0 - 30$ eV. Mirror charges are considered due to the metallic nature of the surface. The initial test electron spectrum as well as the simulated, space–charge influenced one are shown in figure 6.3 (a) and (b), respectively. A distinct broadening and shift towards higher kinetic energies is observable. In the following, the successively variation of single parameters will qualitative demonstrate the influence of the different relevant parameters on the initial test–electron energy–distribution.

6.3.1 Number of electrons per pulse

The number of cloud electrons N_C is one of the most relevant parameters contributing to SCEs. Apparently, the effects are getting stronger the more electrons are emitted from the surface per pulse. Also striking is the fact, that even with quite moderate electron numbers of $\approx 10^4$ per pulse SCEs have been observed at 3^{rd} generation synchrotron radiation sources [22]. Until now, the exact functional dependency of the space–charge induced broadening ΔE_{broad} is not clear. While Zhou et al. found a linear behavior of ΔE_{shift} and ΔE_{broad} as a function of N_C using EUV pulses of some ten ps duration [22], Passlack et al. report on a $\sqrt{N_C}$–dependency of ΔE_{broad} performing photoemission experiments with fs–short pulses in the UV regime [23]. In section 6.5 a systematic and more quantitative analysis of functional N_C–dependence of SCEs will be given.

6.3.2 Pulse duration and spot size

Two more important parameters for the SCE simulations directly result from the characteristics of the incident photon pulse, namely the pulse duration τ_0 and the width of the spot size d_0 at the sample surface. These parameters determine the volume of the electron cloud in front of the surface immediately after leaving the sample and, therefore, directly contribute to the initial electron density. Here, the length scale perpendicular to the surface is dependent on the pulse duration as well as the velocity v_0 of the fastest electrons in this direction, while the lateral dimension is defined by the spot size. Taking into account these parameters, we are able to distinguish between two extreme cases:

1. The **short–pulse limit** (if $\tau_0 << d_0/v_0$): In this limit, the electron cloud can be treated like a quasi–two–dimensional disc. The average distance between the electrons in this disc is proportional to $d_0/\sqrt{N_C}$. Hence, SCEs are independent on the pulse duration but strongly dependent on the spot size. In our first example (cf. figure 6.3 (b)), the maximum kinetic energy of the electrons is 30 eV (conforming with a velocity of v_0= 3.2 mm/ns) and they are emitted from a spot with $d_0 = 200$ μm. The pulse duration of $\tau_0 = 50$ fs is a lot shorter than d_0/v_0= 62 ps and, therefore, this example lies in the short pulse limit. Comparing figure 6.3(b) with an example at the boarder of the short pulse limit 6.3(e) ($\tau_0 = 50$ ps), one identifies the weak dependency on the pulse duration compared to the change of the pulse duration of three orders of magnitude. In contrast, figure 6.3(i) ($d_0 = 200$ μm) and (m) ($d_0 = 50$ μm) serve to illustrate the strong influence of the spot size on the space–charge induced broadening.

2. The **long–pulse limit** (if $\tau_0 >> d_0/v_0$): In this limit, the average distance between the cloud electrons is proportional to τ_0/N_C. Accordingly, the broadening effects are no longer dependent on the spot size, but strongly dependent on the duration of the photon pulse.

While ultrafast laser sources usually fall in the category of the short–pulse limit, one would classify quasicontineous light sources as to be in the long–pulse limit. 3^{rd} generation synchrotron radiation sources (τ_0 = some 10 ps) are situated somehow in between these cases as long as the spot size is not too small. Though, we will not further discuss the long–pulse limit case in this chapter, figure 6.3(d) serves as an example using a quite long pulse duration of $\tau_0 = 200$ ps.

6.3.3 Kinetic–energy distribution

The influence of space–charges on the test electrons is strongly dependent on the kinetic–energy distribution of the cloud electrons. The more both electron distributions resemble each other and the narrower they are, the more pronounced are ΔE_{broad} and ΔE_{shift}. In other words, the higher the spectral density is in the interesting and simulated spectral range, the stronger will be the SCEs. In the first instance, this is caused due to the increased interaction time of the electrons on their way to the detector having a narrow–band energy distribution. The comparison of figure 6.3(b) (wide distribution) and (i) (narrow distribution) underlines this statement.

Using a wide kinetic–energy distribution for the cloud electrons, the SCEs on the initial test electron spectrum are different depending on whether the initial mean energy E_i lies somewhere in between the cloud electron distribution or near the boundary of the energy interval. The space–charge induced broadening and shift is more pronounced for a mean energy near the maximum kinetic energy of the cloud electrons (cf. figure 6.3(b), $E_i = 30$ eV) than for an energy in the middle of the interval (cf. figure 6.3(c), $E_i = 15$ eV). This is due to the reorganization of the electrons on their way to the detector due to the differing kinetic energies. For example, the fastest electrons are propagating in front of the electron cloud most of the time. Therefore, they are additionally accelerated by the precursory ones nearly the whole time.

Finally, we present the influence of the average kinetic energy of the electrons on the SCEs. For this, the mean kinetic energy of the Gaussian test– and cloud– electron–energy distributions is varied over three orders of magnitude. The results are shown in figure 6.3(h) ($E_i = 1$ eV), (i) ($E_i = 30$ eV) and (j) ($E_i = 900$ eV) and the influence seems not to be very significant in comparison of the strong mean energy variation.

6.3.4 Emission–angle distribution

Two further parameters, playing an important role in the numerical simulations of SCEs, are the emission–angle distribution of the test electrons ϑ_t as well as the one of the cloud electrons ϑ_c. However, it is very difficult to experimentally determine the emission–angle distribution of the photoelectrons, because this requires a reference photoemission measurement over the whole hemisphere. The effect of using different distributions is clarified in figure 6.3(f) and (l). On the one hand, a distinct forward–focusing of the cloud electrons (cf. 6.3(l), $\vartheta_c = 0° - 45°$) results in an enhancement of SCEs on the test electron spectrum. On the other hand, isotropically emitted cloud electrons as well as the emission of the test electrons in off–normal direction leads to a considerably weaker effect (cf. 6.3(f), $\vartheta_t = 45°$). Because of the difficulties in the determination of the real emission–angle distribution of the photoelectrons, one has to assume a distribution for the SCE simulations. For this, a cosine–distribution generally works very well considering the electron mean free path in the solid but neglecting any matrix–element effect.

6.3.5 Mirror charges

Zhou et al. already reported that mirror charges may play an important role in the description of SCEs in photoemission of metallic samples [22]. Apparently, mirror charges always reduce the final kinetic energy of the test electrons. This can be illustrated using the following two extremal examples. In the case of an electron located behind the cloud and, therefore, in between the mirror charges and the rest of the cloud electrons, both are contributing to a deceleration of this electron. An electron propagating in front of the electron cloud is indeed additionally accelerated, but the positive mirror charges again have an decelerating effect that is absent when neglecting these attractive charges. Figure 6.3(k) shows the simulated spectrum in the case of not included mirror charges. The spectral test electron distributions is strongly shifted and broadened and has got an asymmetric character in comparison to the spectrum where mirror charges are included (cf. figure 6.3(b)). This demonstrates that mirror charges can partly compensate induced SCEs.

6.3.6 Coulomb interaction between cloud electrons

In the simple numerical simulations in reference [22], the cloud electrons are propagating on straight trajectories because of neglected mutual Coulomb interactions of the cloud electrons. This approximation can be justified by our simulated examples using a moderate number of electrons per pulse ($N_c = 10^4$). Figure 6.3(b) (mutual Coulomb interactions considered) and (g) (mutual Coulomb interactions switched off) show no distinct change in the influenced test electron spectrum. However, in the case of significantly higher electron densities accordingly with higher N_c or when $\Delta E_{broad} \approx E_i$ the mutual Coulomb interactions have to be taken into account.

In conclusion, in this section we have learned with the help of qualitative examinations, that one has to consider a lot of different parameters in the numerical simulation of vacuum space–charge effects in solid–state photoemission, because those are all influencing the final kinetic–energy distribution in a characteristical way. Consequently, to quantitatively understand the appearance of SCEs in a specific photoemission experiment one has to know these parameters as accurate as usual and one does not get around performing microscopic simulations as realistic as feasible.

6.4 Comparison with experiments

Lately, the ongoing improvements of experimentally achievable energy (sub–meV) and angular resolution (below 0.1 °) on the spectrometer side [37, 38] and peak brilliance on the photon source side have led to the necessity to address more attention to SCEs in photoemission experiments. To validate our numerical approach using the Treecode Algorithm for simulating space–charge induced spectral changes, we have compared simulation results for three different parameter sets with the experimental results of photoemission measurements possessing SCEs reported in three recent publications [22–24]. The experiments are performed employing three different light sources: a 3^{rd} generation synchrotron radiation source, an ultrafast laser system and a free–electron laser. Therefore, the experimental parameters as well as the observed SCEs vary over several orders of magnitude and can consequently serve to reveal the universal applicability of our numerical simulations of SCEs in photoemission.

6.4.1 Synchrotron radiation source with 60 ps EUV pulses

Zhou et al. extensively studied the influence of vacuum space–charge as well as mirror–charge effects employing a 3^{rd} generation synchrotron radiation source (the ALS in Berkeley) delivering EUV light (hν = 34 eV) with a pulse duration of 60 ps FWHM [22]. They showed that even at such relatively moderate numbers of photoelectrons of up to $N_c \approx 2000$ per pulse, the resulting spectral distortions ($\approx$ 10 meV) can be the limiting factor of the achievable experimental energy resolution in high–resolution ARPES. The measurements were performed using a polycrystalline gold sample cooled down to a temperature of 20 K to obtain an intrinsic photoemission spectrum (cf. figure 6.4(a) with a sharp Fermi edge at $E_i = 29.38$ eV). The spot size on the sample was about 0.43 × 0.3 mm^2 and the emitted photoelectrons were detected at an angle of $\vartheta = 45°$. Zhou et al. [22] found a linear dependence of the energy broadening and shift on the number of photoelectrons. First simple Monte–Carlo simulations agree with the observed linear behavior as well as with the importance of considering mirror–charge effects in metallic samples.

For our numerical simulations we used the parameters of the publication and assumed a cosine emission–angle distribution for the cloud electrons considering the electron inelastic mean free path in the solid. The initial kinetic–energy distribution of the test electrons was

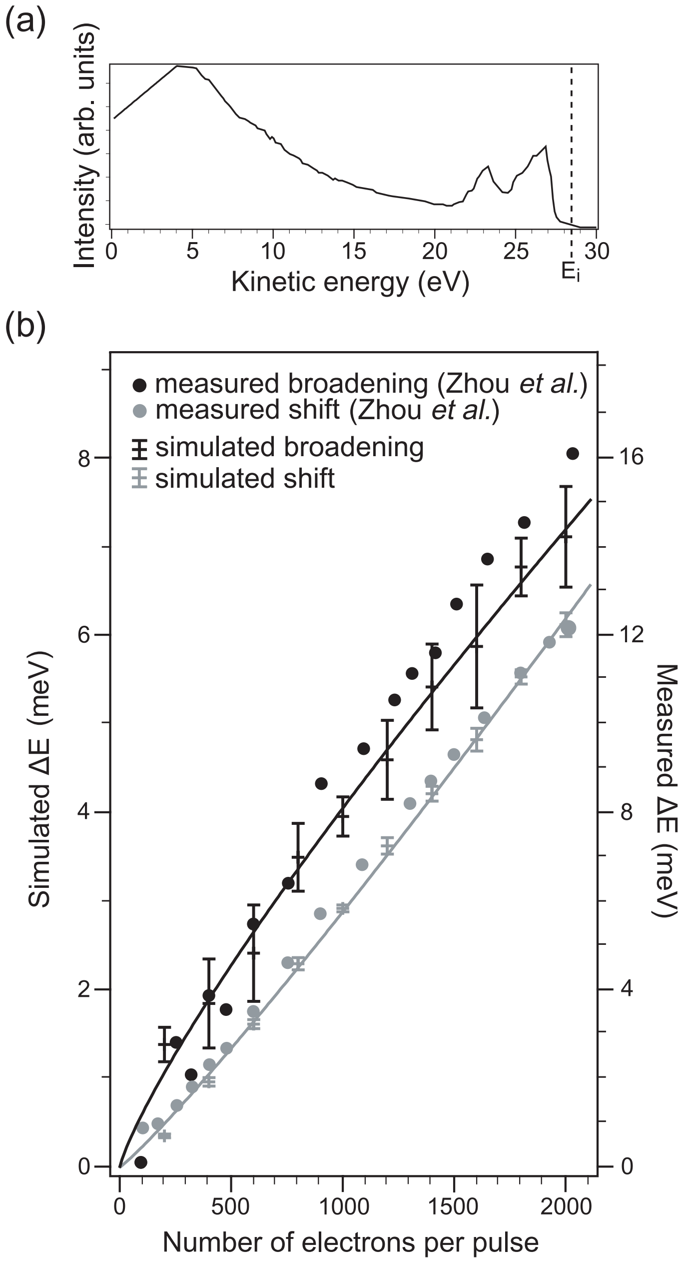

Figure 6.4: Space–charge effects on the photoemission spectrum of a polycrystalline gold sample under irradiation with $\tau_0 = 60$ ps, $\hbar\omega_0 = 34$ eV photon pulses. (a) Typical energy distribution curve with the Fermi cutoff at 29.38 eV (taken from [22]). (b) Comparison between simulated and measured [22] Fermi edge shifts and broadenings in the range of (0–2000)e^- per pulse. Note the different scales of the vertical axes. Power–law fits to the simulated energy shift and broadening serve as guides for the eyes ($\Delta E_{shift} \propto N_c^{1.11}, \Delta E_{broad} \propto N_c^{0.83}$). The spot size is 0.43×0.3 mm^2 and the test electrons are emitted with an angle of 45°. In the simulation, a cosine distribution of the cloud electron emission angles is used (from Ref. [25]).

Gaussian with a mean energy of $E_i = 29.38$ eV and $\Delta E_i = 18$ meV FWHM accordingly to the Fermi edge in the experiments. The energy broadening and shift of the test electron spectrum were calculated as a function of N_c and can be compared with the experimentally determined one from Zhou et al. [22] in figure 6.4(b). A nearly linear dependence of ΔE_{shift} and ΔE_{broad} can be observed in both, the experiment and our simulations. Furthermore, the tendency of ΔE_{shift} being smaller than ΔE_{broad} is reproduced as well. For normal emission ($\vartheta_t = 0°$) this tendency would have been reversed, indicating that the space–charge induced energetic shift is affected stronger by an increasing off-normal emission than the broadening. The difference by a factor of 2 between the simulated and the experimental results (cf. the different scales on the vertical axes in figure 6.4(b)) does not necessarily mean, that our simulations do not describe the experiment sufficiently well. A slightly reduced experimental spot size or a more forward directed emission of the electrons lead to a nearly perfect description of the space–charge induced effects, showing the importance of knowing the experimental parameters for a quantitative analysis as good as possible.

6.4.2 Ultra violet laser source with 40 fs pulses

Passlack et al. [23] performed two–photon photoemission experiments on the sharp Shockley surface state of Cu(111) using a low repetition, high intensity femtosecond Ti:sapphire laser ($\tau_0 = 40$ fs, h$\nu = 3.1$ eV). They investigated the occurring space–charge broadening effects for up to 80000 electrons emitted in normal direction and with very low kinetic energies ($E_i = 0.912$ eV). A typical energy distribution curve at low pulse intensity is shown in figure 6.5(a) (solid curve). The experimental spot size on the sample was 1.15×0.9 mm^2 FWHM. Unlike Zhou et al. [22], Passlack et al. did not find a linear behavior for the energy broadening, rather a square root dependence on the number of photoelectrons.

Beside the considerably lower kinetic energies of the photoelectrons, the photoemission experiment of Passlack et al. differs from the one of Zhou et al. significantly due to the dispersion of the surface state as a function of the emission angle. As in [23], only the intrinsic kinetic–electron distribution in normal direction is presented, we have had to do additional assumptions for our SCE simulations, therefore being the major source of uncertainty in our investigations. These are the following ones:

1. The secondary electrons are emitted isotropically over the hemisphere with an emission–angle independent kinetic–energy distribution similar to the one in figure 6.5(a) (dark grey). The best results were delivered using a ratio of the number of electrons coming from the surface state N_{surf} to the number of secondary electrons N_{sec} of $N_{surf}/N_{sec} = 0.5$. This value critically affects the simulated SCEs.

2. For the kinetic–energy distribution of the photoelectrons the dispersion relation of the Shockley surface state of Cu(111) is taken from reference [115]. The binding energy E_B of the surface state as a function of the parallel momentum $\vec{k_{\|}}$ can be described by:

$$E_B(\vec{k_{\|}}) = E_0 + \frac{\hbar^2 \vec{k_{\|}}^2}{2m^*} \qquad , \tag{6.4}$$

   where $E_0 = -0.39$ eV is the binding energy at the Γ–point and $m^* = 0.41 m_e$ the effective electron mass [115] (which is related to the curvature of the parabolic shaped

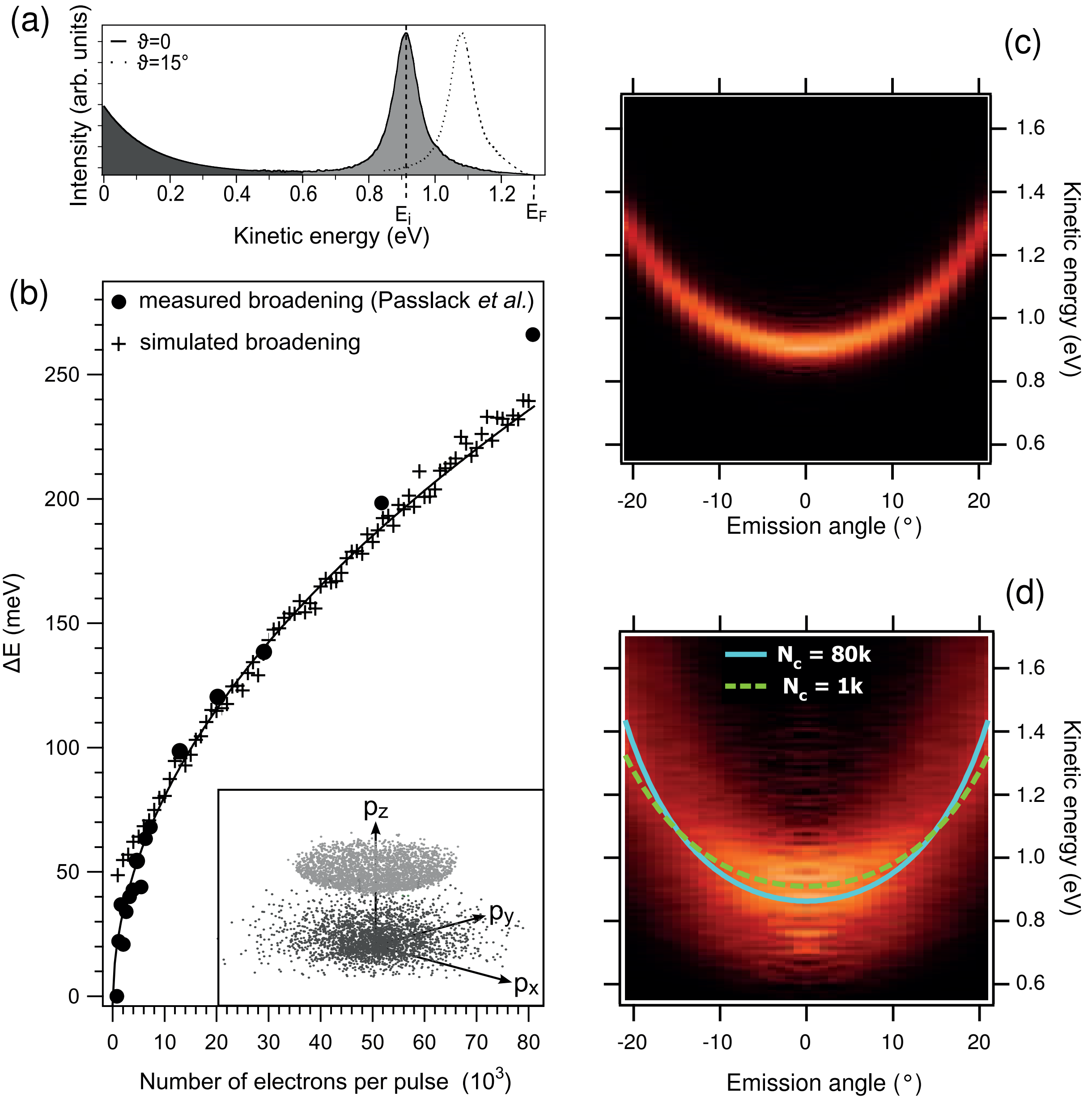

Figure 6.5: Space–charge effect on the two–photon–photoemission spectrum of a Cu(111) surface under irradiation with intense $\tau_0 = 40$ fs, $\hbar\omega_0 = 3.1$ eV photon pulses. (a) Typical energy distribution curves of the Shockley surface state for emission angles of $\vartheta_t = 0°$ (solid curve) and $\vartheta_t = 15°$ (dotted curve), respectively (taken from Ref. [23]). In the case of normal emission, the surface–state photoemission peak (light gray) is located at a kinetic energy of 0.912 eV and is followed by a characteristic secondary electron background (dark gray). (b) Comparison between our simulated and the measured [23] energy broadenings of the surface–state peak in the range of $(0\text{–}80000)e^-$ per pulse. The simulated broadening shows a power–law behavior $\Delta E_{broad} \propto N_c^{0.5}$ (solid line). The spot size is $1.15 \times 0.9\ \mathrm{mm}^2$ and the test electrons are emitted in the normal direction. In the simulation, an angular distribution of the cloud electrons is assumed that accounts for the parabolic energy–momentum dispersion relation. The inset illustrates the distribution of surface–state (light gray) and secondary electrons (dark gray) in momentum space (from Ref. [25]). The diagrams on the right hand side compare the intrinsic angle resolved photoemission spectrum of the surface state ($N_c = 1000$, (c), with parameters from [115]) with the one, influenced by SCEs ($N_c = 80000$, (d)), both calculated with the our simulation algorithm.

electronic state). Finally, the transformation of (6.4) leads to the kinetic–energy distributions as a function of the emission angle ϑ_t:

$$E_{kin}(\vartheta_t) = \frac{2h\nu - \phi_0 + E_0}{1 - \frac{m_e}{m^*} sin^2(\vartheta_t)} \quad . \tag{6.5}$$

With the absorbed energy within the two–photon–photoemission process of $2h\nu = 6.2$ eV and the work function of Cu(111) of $\phi_0 = 4.9$ eV the position of the Fermi energy can be calculated to be $E_F = 1.3$ eV. The electrons in our numerical simulations are consequently isotropically emitted according to relation (6.5) within $\vartheta_t = \pm 20.8°$. Here, the surface state crosses the Fermi energy. Figure 6.5(a) shows the spectrum at $\vartheta_t = \pm 15°$ (dotted line) additionally to the one in normal emission.

3. Further intensity dependent variations due to matrix–element effects in the photoemission process are neglected in our simulations.

The inset in figure 6.5(b) illustrates the distributions of the surface–state electrons (light grey) as well as of the secondary electrons (dark grey), in momentum space clearly separated from each other.

Using the experimental parameters from reference [23] for our numerical simulations and the additional assumptions mentioned above the results are in an excellent agreement with the experimentally found space–charge broadening in the range of 0 – 80000 cloud electrons per pulse (cf. figure 6.5(b)). Only small deviations are observable for the lowest and highest numbers of electrons. Consequently, fitting the simulated spectral broadening with a power law $\Delta E_{broad} \propto$ leads to a $\sqrt{N_c}$–dependence. Such a square–root behavior is characteristic for very low kinetic energies (≤ 1 eV) and can not be extrapolated for higher energies. In section 6.5 this will be discussed further.

Finally, we have also investigated the space–charge induced shifting of the energy spectra dependent on the emission angle as a function of N_c. While Passlack et al. reported of a negligible shift up to 40000 electrons per pulse in normal direction [23], our simulation results rather show an increased shift to lower kinetic energies ($\approx$-1.5 μeV per cloud electron). With increasing emission angle this negative shift is contineously compensated and switches to a shift towards higher kinetic energies at the border of the parabolic dispersion relation. The parabolic surface state is effectively stretched due to the SCEs (cf. figure 6.5(c) and (d)). This can be explained by an additional decelerating of the slower electrons emitted from the valley of the parabola by the faster ones and the analogously accelerating influence on the faster surface state electrons at higher polar angles. The space–charge induced shift ΔE_{shift} especially depends on the chosen electron energy distributions in the whole momentum space as well as on the ratio of N_{surf} to N_{sec}. The discrepancy of our findings to the experimental results of Passlack et al. can therefore be overcome by a better knowledge of these critical parameters.

6.4.3 Free–electron laser with 40 fs pulses

Free–electron lasers, like the one opened for users access in Hamburg in 2005, deliver ultrafast photon pulses in the UV to X–ray regime and have the potential to make time–resolved core–level PES by default feasible. Pietzsch el al. were the first who reported on studies of SCEs at core–level photoemission using a 40 fs short EUV free–electron laser

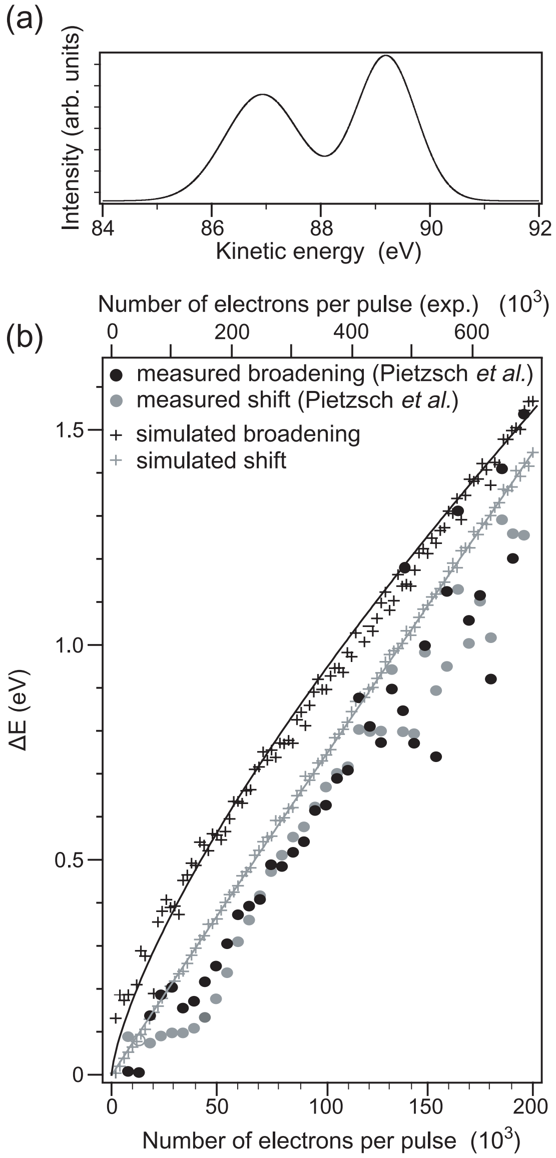

Figure 6.6: Space–charge effects on a W $4f$ core–level spectrum under irradiation with τ_0 = 40 fs, $\hbar\omega_0$ = 118.5 eV photon pulses. (a) Typical energy distribution curve with photoemission peaks at kinetic energies of $\sim$ 87 eV and $\sim$ 89 eV (taken from Ref. [24]). (b) Comparison between simulated and measured [24] peak shifts and broadenings in the range of (0–200000)e^- per pulse. Note the different scales of the axes for the simulated (bottom axis) and measured (top axis) SC–induced energetic shifts and broadenings. Power–law fits to the simulated energy shift and broadening serve as guides for the eyes ($\Delta E_{shift} \propto N_c^{0.98}, \Delta E_{broad} \propto N_c^{0.73}$). The spot size is 0.27 × 0.4 mm^2. In the simulation, a cosine distribution of the cloud electron emission angles is used and the test electron acceptance angle is set to 13° (from Ref. [25]).

(FLASH in Hamburg) [24]. They performed a photoemission experiment on the W 4*f* core levels at a photon energy of hν = 118.5 eV and a spot size on the sample of approximately 0.27 × 0.4 mm^2. An example of the spin–orbit splitted W 4*f* lines measured with PES at low pulse intensities is shown in figure 6.6(a).
We adopted the experimental parameters from the publication and additionally assumed a cosine emission–angle distribution of the cloud electrons as well as emission angles of the test electrons in the range of $\vartheta_t \leq 13°$ in accordance with the acceptance angle of the electron analyzer. In figure 6.6(b) the results of our numerical simulations and the experimental ones from Pietzsch et al. [24] are compared, showing a plot of ΔE_{shift} and ΔE_{broad} averaged over the two W 4*f* peaks as a function of N_c. The linear dependence of ΔE_{shift} as well as the nearly linear behavior of ΔE_{broad} observed in the experiment are again very well reproduced by our numerical approach, though a huge discrepancy by a factor of approximately 3 in the number of cloud electrons leading to comparable space–charge induced effects is obvious (note the different scales of the horizontal axes in figure 6.6(b)). However, in the experiments the number of emitted electrons per pulse was determined very indirectly by measuring the number of photons per pulse N_{ph} with a microchannel–plate–based tool (MCP–tool) and calculating the theoretically emitted photoelectrons using values for the photoionization cross section and the electron mean free path from the literature. Furthermore, the MCP–tool was calibrated for a photon energy of 38.5 eV and the conversion to hν = 118.5 eV again was done by using tabulated values [89]. So, we have to assume a quite large error in the experimentally determined number of electrons N_c, and our quantitative results become more reasonable.

The following major conclusions can be drawn from this section. Our numerical simulations show very good qualitative agreements of ΔE_{shift} and ΔE_{broad} as a function of N_c with the performed photoemission experiments for all three strongly varying parameter sets. For experiments using relatively high photon energies in the EUV or X–ray regime and consequently measuring electrons with kinetic energies larger than some eV this functional dependency seem to be quite linear, while for $E_{kin} < 1$ eV a square–root like behavior is found. Quantitatively, our numerical results are conform with the corresponding experiment within a factor of three. This can mainly be deduced to uncertainties of experimental parameters. Especially the emission–angle distribution as well as the number of electrons per pulse critically contribute to the observed SCEs but are, on the other hand, hard to be measured accurately. To conclude, our numerical simulations using the Treecode Algorithm describe the experimentally observed SCEs quite realistic, making this approach a universally applicable tool for understanding effects on the photoemission spectra using modern and highly intense photon sources.

6.5 General limits

The successful reproduction of the space–charge induced spectral changes in three considerably differing photoemission experiments makes it reasonable to investigate this effect more quantitatively and for a wider parameter range, even in between the parameter sets of the three examples of section 6.4. The goal of this section will be to deliver the experimenter a rule of thumb for the resolution limits of their specific photoemission experiments due to SCEs. To achieve this, we introduce two simple analytic models from the literature, both trying to describe the energetic broadening due to Coulomb interactions within propagating, high dense electron clouds. Thereupon, we address the issue of SCEs in photoemission for a wide parameter range in two experimental situations, both differing with regard to the kinetic–energy distribution of the electrons on the one hand and the interesting energy scale on the other hand. In core–level spectroscopy most of the emitted electrons are energetically located within a narrow energy interval and the relevant energy scale lies roughly within a few 100 meV. In the second case, the valence–band spectroscopy, the electrons are emitted from an energetical regime of very narrow bandwidth (e. g. the Fermi–energy) propagating in front of a wide (some eV) electron background. Here, the energy scale is typically smaller than 10 meV. Furthermore, the effects on the momentum resolution are indeed from great interest for angle–resolved valence–band spectroscopy.

6.5.1 Simple models for the space–charge induced spectral broadening

In the literature, the following two analytical approaches [105, 111] are adopted to model the propagation dynamics of electron packets in photoemission experiments using pulsed photon sources as well as to estimate the onset of space–charge induced spectral broadening ΔE_{broad}. In both models ΔE_{broad} is described as a function of the three main parameters: the number of electrons per pulse N_c, the spot diameter d_0 and the initial kinetic energy E_i.

Model of Long *et al.*

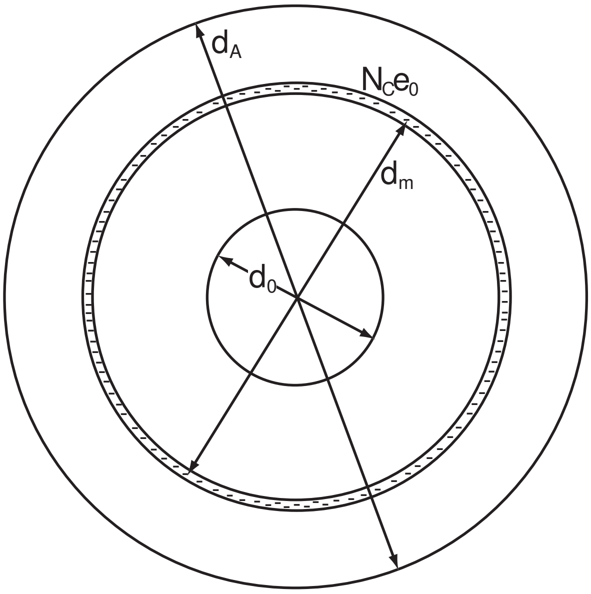

Figure 6.7: Schematic of the analytical model developed by Long *et al.* (from [111]). The inner shell with the diameter d_0 represents the illuminated area on the sample. The outer shell with the diameter d_A corresponds with the position of the grounded electron analyzer. The narrow spherical shell with the diameter d_m containing all photoelectrons N_ce_0 propagates from the inner to the outer one. It is assumed that the pulse duration is very small compared to the transit time to the detector.

In the model of Long *et al.* the sample is approximated by a sphere with a diameter d_0 (cf. figure 6.7). The photoelectrons propagate within an expanding spherical shell of negligible thickness. This assumption is legitimated, when the pulse duration τ_0 is very short compared to the transit time to the detector. The energetic broadening is determined by the difference between the energy gain of the precursory electrons and the energy loss of the following ones. Finally, the following relation is obtained:

$$\Delta E_{broad} = \frac{N_c e_0}{\pi \epsilon_0 d_0} \approx 6 \times 10^{-6} \frac{N_c e_0}{d_0} \qquad , \tag{6.6}$$

where ΔE_{broad} is given in eV and the diameter d_0 in mm. This relation is independent on the main kinetic energy E_i and the pulse duration τ_0, in agreement with the short pulse limit, introduced earlier in section 6.3. Relation (6.6) also correspond with the Coulomb energy of an electron located on a homogeneously charged disk or on the surface of a charged sphere each with the diameter d_0 and total charge of $N_c e_0$. Therefore, an easier approach to obtain relation (6.6) for the energy broadening would have been the consideration of simple electrostatic models for the electron cloud as well as energy conservation as has been done in [116].

Model of Siwick *et al.*

Originally, this "mean–field–model" quantifying the energy broadening as a function of N_c, d_0 and E_i was developed by Siwick *et al.* [105] to describe the propagation dynamics of electron bunches of fs duration in terms of ultrafast electron diffraction experiments. Later, Passlack et al. transfer this model to their observed SCEs in two–photon–photoemission experiments using an ultrafast and high intense laser system [23] (see section 6.4.2). The model assumes a pancake shaped electron distribution whose lateral dimension (given by the spot diameter d_0) exceeds the one in the direction perpendicular to the surface by at least one order of magnitude. The space–charge induced kinetic–energy bandwidth for such an electron distribution is assumed to be proportional to the group velocity of the electron bunch v_0 as well as to the elongation rate of the electron bunch in the propagation direction $\Delta v = dl/dt$. This leads to the approximation for ΔE_{broad} of [105]:

$$\Delta E_{broad} \approx m v_0 \Delta v = m v_0 \frac{dl}{dt} \qquad . \tag{6.7}$$

Finally, considering energy conservation and consequently a transfer of the initial potential Coulomb energy into kinetic energy (which is directly related to the elongation rate in this model) the following relation for the energy broadening in units of eV can be approximated:

$$\Delta E_{broad} \approx C \sqrt{\frac{E_i N_c}{d_0}} \qquad . \tag{6.8}$$

Here, d_0 has to be inserted in mm and the prefactor C ranges between 0.002 and 0.005 [23, 105, 114] depending on how the potential Coulomb energy in the quasi–two dimensional disc is approximated.

In contrast to the model of Long et al., this mean–field–model predicts a square–root dependency on the number of emitted electrons N_c and the inverse spot diameter

$1/d_0$, but also a proportionality to the square root of the mean kinetic energy E_i, while in relation (6.6) no E_i–dependence is suggested.
In what follows, these simple analytical models are compared with our numerical simulations for a wide parameter range and the range of reliability and applicability in terms of typical core–level and valence–band photoemission experiments is tested.

6.5.2 Core–level spectroscopy

Here, we present the investigations on SCEs in core–level spectroscopy (also known as X–ray photoelectron spectroscopy or electron spectroscopy for chemical analysis) by simulating a simplified but representative electron distribution. As already mentioned, in core–level spectroscopy most of the photoelectrons are emitted within a very narrow energy interval. Therefore, for the numerical simulations the kinetic–energy distribution of the cloud electrons as well as of the test electrons is chosen to be Gaussian with a width of ΔE_i =100 meV FWHM (corresponding with the preferred energy resolution in core–level spectroscopy) and a main energy of E_i. The cloud electrons are emitted isotropically over the hemisphere while the test electron emission angle is set to $\vartheta_t = 0°$. A couple of parameters are varied over a considerable range to obtain results as general as possible. Beside the most important simulation parameter – the number of cloud electrons N_c, which is varied between 100 and 500000 e^- per pulse – these are the spot diameter d_0 (0.1 mm, 0.4 mm, 1 mm), the pulse duration τ_0 (20 fs, 1 ps, 50 ps) and the initial mean kinetic energy E_i (1 eV, 10 eV, 100 eV, 1000 eV). Even though considering a kinetic energy of 1 eV is quite unrealistic in core–level spectroscopy due to dominating secondary electrons in this regime, this mean energy was included in the simulations due to possible similarities to valence–band spectra measured by using very low photon energies as discussed in section 6.4.2.

Figure 6.8 shows the simulation results using the Treecode Algorithm. The energetic broadening ΔE_{broad} and shift ΔE_{shift} are plotted as functions of the linear electron density N_c/d_0. The error bars represent the standard deviation of the result from the multipely repeated simulations with varying parameters d_0, τ_0 and E_i. One has to note, that the simulation results for $\tau = 50$ ps shows a significantly lesser shift of the initial spectrum as well as a substructure in the spectral shape (cf. figure 6.3(d)) also observed in the recent experiments by Reed et al. [103]. The solid lines in figure 6.8 represent fits of a power law to the numerically determined space–charge induced broadening and shift. The following proportionalities are found:

$$\Delta E_{broad} \propto (N_c/d_0)^{0.98} \text{ and } \Delta E_{shift} \propto (N_c/d_0)^{0.98},$$

and, therefore, a linear dependency of the observed vacuum space–charge effects on the linear electron density, at least for high electron densities. In this regime the energy broadening calculated by the simple model of Long et al. [111] (see relation (6.6)) deviates from the simulations by a factor of 3, but describes the linear behavior very well. Again, the reason for this behavior can be found in the conversion of Coulomb energy into kinetic energy. In pulsed photoemission experiments a pancake–like electron bunch is emitted from the sample. In such an electron distribution the potential energy for one electron is proportional to N_c/d_0. Therefore, the initial potential–energy spread of the electron cloud is proportional to N_c/d_0 as well. Finally this leads to a $\Delta E_{broad} \propto (N_c/d_0)$, as predicted by Long et al. [111]. For lower electron densities ($N_c/d_0 < 10^4$ e^-/mm) ΔE_{broad} strongly

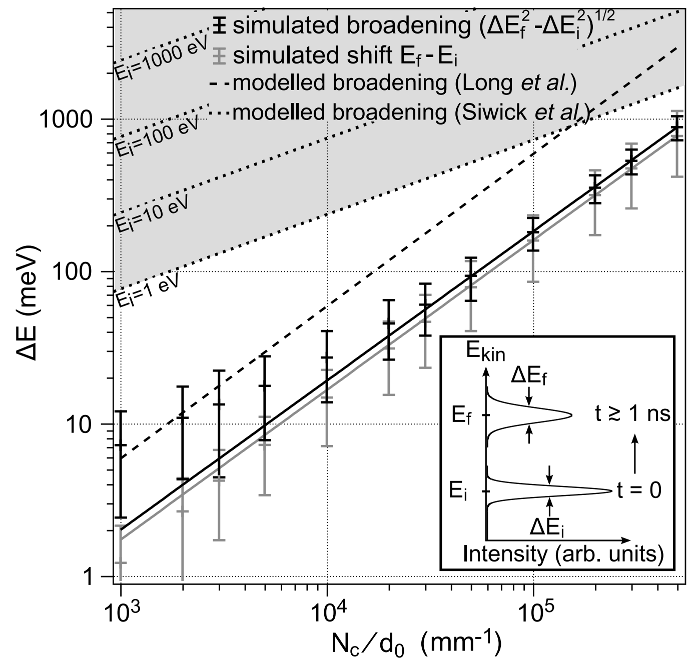

Figure 6.8: Simulated energy shift (gray data points) and energy broadening (black data points) as functions of the cloud electron density N_c / d_0 for a situation similar to core–level photoemission spectroscopy. The error bars result from a systematic variation of the light spot diameter d_0 (0.1, 0.4, and 1 mm), mean energy E_i (1, 10, 100, and 1000 eV), and pulse duration τ_0 (20 fs, 1 ps, and 50 ps). In the simulation, identical initial Gaussian energy distributions for cloud and test electrons with 100 meV FWHM are used. The cloud electrons are emitted isotropically over the hemisphere; the test electrons are emitted in the normal direction. The solid lines represent power–law fits to the simulated data [$\Delta E_{shift} \propto N_c^{0.98}, \Delta E_{broad} \propto N_c^{0.98}$]. The dashed line corresponds to relation (6.6) [111]; the dotted lines plotted over the area highlighted in gray are calculated from relation (6.7) for the different mean energies E_i [24, 105]). The inset illustrates the space–charge effects on an energy spectrum (from Ref. [25]).

deviates from the linear relation and tends to an absolute value of approx. 10 meV. This is due to the calculation of the space–charge induced broadening by the deconvolution of two Gaussian profiles. Assuming an initial peak width of 100 meV FWHM, the simulations are not sufficiently accurate to follow the trend of space–charge broadening arbitrarily down to lower electron densities.

While relation (6.6) describes the situation of space–charge induced energy broadening in core–level spectroscopy quite well, the situation predicted by Siwick et al. [105] (see relation (6.8) and dotted line in figure 6.8) overestimates the energy broadening by far. Here, ΔE_{broad} is strongly dependent on the initial main kinetic energy as well as on the square root of the linear electron density. So, the model of Siwick et al. [105] can not be applied in describing SCEs in core–level spectroscopy.

The following rule of thumb can be drawn from this section and directly from figure 6.8: For core–level spectroscopy one usually needs relatively moderate experimental energy resolution. Therefore, the linear electron density in the experiment may not exceed 10000 e^-/(pulse mm) to keep the space–charge induced energy broadening below $\sim$50 meV. Within a factor of 2 this value agrees well with experimentally determined onsets for the broadening effects reported in [111, 117, 118] as well as with the example discussed in section 6.4.2 [23].

6.5.3 Valence band spectroscopy

In high–resolution angle–resolved photoelectron spectroscopy the situation is significantly different from the one in core–level spectroscopy. Here, great interest lies on fine details of the electronic structure near the Fermi energy. For this, a photoemitted cloud of electrons – secondary electrons as well as valence band electrons – with kinetic energies of 0 to E_F is studied with high energy and angular resolution. To represent this situation within the simulations, a test electron energy spectrum with a mean energy at E_i and 5 meV FWHM is used. The kinetic–energy distribution of the cloud electrons is rectangularly reaching from 0 eV to E_i, and they are emitted isotropically. As done for the simulations for core–level spectra in the previous section, the test electrons are followed only in the forward direction. To gain results as general as possible, different simulation parameters are varied over several orders of magnitude; these are the number of cloud electron N_c (4 to 40000), the spot diameter d_0 (0.04, 0.1, 0.4 mm), the mean energy of the test electrons E_i (1, 10, 100 eV) and the pulse duration τ_0 (10 fs, 10 ps).

Figure 6.9(a) shows the general trend of the space–charge induced shift ΔE_{shift} and broadening ΔE_{broad} obtained by the numerical simulation with the Treecode Algorithm as a function of the linear electron density. The error bars are received by the variation of the mean energy as well as the pulse duration and result in an accuracy of a factor of two. Though, a nearly proportional behavior (solid lines in figure 6.9(a)) for the shift ($\Delta E_{shift} \propto \frac{N_c}{d_0}^{1.02}$) and broadening ($\Delta E_{broad} \propto \frac{N_c}{d_0}^{0.98}$) is found for $\frac{N_c}{d_0} > 1000\ e^-/mm$. Once more, for lower electron densities the saturation of the broadening at a finite value below the initial width of 5 meV comes due to the determination by deconvolution. In addition to the simulation results, the model of Long et al. [111] is displayed as a dotted line in figure 6.9(a). Again, the linear behavior agrees very well with our calculations, but the model overestimates our numerical simulation by a factor of three. The main reason for this lies in the different energy distributions. While the distribution used in the model of Long et al. is nearly

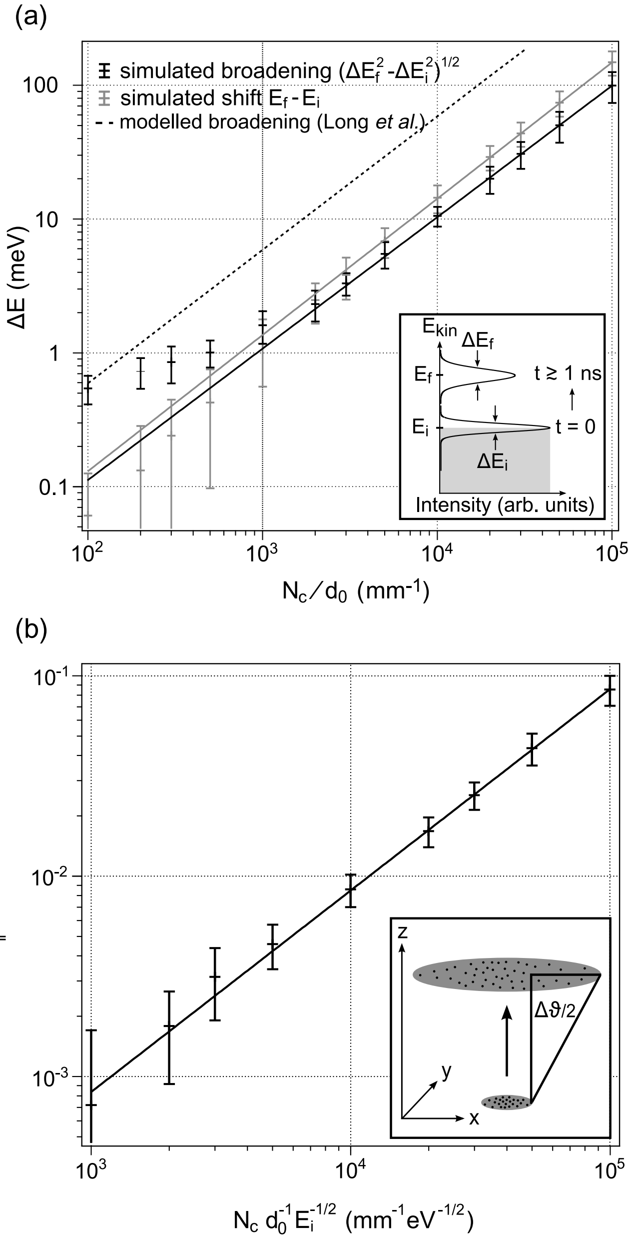

Figure 6.9: (a) Simulated energy shift (gray data points) and energy broadening (black data points) as functions of the cloud electron density N_c/d_0 for a situation corresponding to angle–resolved valence–band spectroscopy. The error bars result from a systematic variation of the light spot diameter d_0 (0.04, 0.1, and 0.4 mm), mean energy E_i (1, 10, and 100 eV), and pulse duration τ_0 (10 fs and 10 ps). In the simulation, an initial Gaussian test electron energy spectrum with mean energy E_i and 5 meV FWHM is used together with a rectangular distribution of the cloud electron energies in the interval $0..E_i$ (see inset). The cloud electrons are emitted isotropically over the hemisphere; the test electrons are emitted in the normal direction. The solid lines represent power–law fits to the simulated data [$\Delta E_{shift} \propto \frac{N_c}{d_0}^{1.02}, \Delta E_{broad} \propto \frac{N_c}{d_0}^{0.98}$]. The dashed line corresponds to relation (6.6) [111]. (b) Simulated momentum broadening as a function of $N_c/(d_0\sqrt{E_i})$. The same parameter sets as in (a) are used, except that the mean energies E_i are now 1, 25, and 100 eV. The inset illustrates the space–charge–induced divergence of the electron distribution in real space (from Ref. [25]).

mono–energetic, in the simulations for valence band spectroscopy a broad and constant distribution between 0 eV and E_i is used and, therefore, the electron density in phase space is less. As expected, the model of Siwick et al. [105] overestimates our simulation results by far and is thereby not included in the diagram.

From the presented findings concerning space–charge induced worsening of the experimental energy resolution in valence band spectroscopy the following rule of thumb can be drawn: A tolerable energy resolution of ≤ 5 meV can be achieved by delivering a one dimensional electron density $\frac{N_c}{d_0}$ of 3000 e^-/mm. This corresponds quite well with the report of Zhou et al. [22], where 600 electrons emitted from a spot with a diameter of 0.37 mm lead to a broadening of the Fermi edge of roughly 5 meV.

Beside the need of an extremely good energy resolution in ARPES experiments, a sufficiently well momentum resolution is essential. A lot of interesting effects in solid state physics, e.g. phase transitions in highly correlated materials, can be followed in distinct changes of the dispersion relation $E_B(k_\parallel)$ of the valence bands. The wave vector $k_\parallel$ is connected with the measured kinetic energy E_{kin} of the photoelectrons and the emission angle ϑ by

$$k_\parallel = \sqrt{\frac{2m_0}{\hbar^2}E_{kin}} \cdot sin(\vartheta) \qquad . \tag{6.9}$$

From this directly follows a worsening of the momentum resolution $\Delta k_\parallel$ by a loss of experimental angular resolution $\Delta\vartheta$, e.g. due to the Coulomb forces in the electron cloud and the resulting lateral expansion of the electron distribution. From 6.9 and considering only electrons emitted perpendicular to the surface the linear relation between momentum resolution and angular resolution is obvious:

$$\Delta k_\parallel \approx \sqrt{\frac{2m_0}{\hbar^2}E_{kin}} \cdot \Delta\vartheta \propto \Delta\vartheta \qquad . \tag{6.10}$$

To study the space–charge effect induced momentum broadening and especially the influence of the kinetic energy of the electrons in the numerical simulations with the Treecode Algorithm the same parameter variation is executed as for the energy resolution, but for three different mean energies E_i (1 eV, 25 eV, 100 eV). Then, the resulting loss of angular resolution $\Delta\vartheta$ is determined from the lateral expansion of the test–electron cloud – formally emitted in normal direction – as illustrated in the inset of figure 6.9(b). Here, the SC–induced momentum broadening $\Delta k_\parallel$ is plotted against $\frac{N_c}{(d_0\sqrt{E_i})}$ and a linear function is fitted to the data (solid line).

This linear behavior can be explained as follows: The angular spread can obviously be approximated by $\Delta\vartheta \approx \Delta v_\parallel / v_0$, where $\Delta v_\parallel$ is the velovity gain of the electrons parallel to the surface due to Coulomb forces and v_0 the group velocity of the test electrons corresponding to the mean energy E_i. Together with the reasonable assumption $v_0\Delta v_\parallel \propto \Delta E_{broad} \propto N_c$, the SC–induced angular broadening becomes $\Delta\vartheta \propto \frac{N_c}{E_i}$ and finally, via formula 6.9, the following relation for the momentum broadening:

$$\Delta k_\parallel \propto \frac{N_c}{\sqrt{E_i}} \qquad . \tag{6.11}$$

With the simulations concerning momentum broadening, we can give an estimate for the upper limitation for the electron density before SCEs become relevant for the momentum resolution. In modern ARPES experiments total experimental energy resolution of better than 0.01 $\mathring{A}^{-1}$ is achieved and also requested. So, one is limited to an electron density of approximately 10000 $e^-/(mm\ eV^{\frac{1}{2}})$. This means for experimental conditions as described by Zhou et al. ($d_0 \approx 0.4$ mm, $E_i = 30$ eV): As long as the number of photoelectron per pulse does not exceed 22000, one can neglect space–charge induced momentum broadening effects. Furthermore, energy broadening effects occur much earlier than momentum broadening, and thus will normally be the limiting factor in ARPES.

6.6 Summary and conclusion

In photoelectron spectroscopy the influence of SCEs on the experimental energy resolution will become more and more relevant, especially in connection with modern, highly brilliant photon sources such as free–electron lasers. In this chapter the magnitude of SCEs is studied as a function of various parameters (number of electrons, spot size, pulse duration, kinetic energy and emission angle distribution) using a molecular–dynamics simulation. Herein, a special interest lies in high electron densities and the resulting interaction–induced changes in phase space. Our choice for realizing the investigations is a full N–electron simulation using a modified Treecode Algorithm for sufficiently fast and accurate calculations.

This simulation algorithm was tested on three recent experimental cases, all differing in the basic experimental conditions. The experiments are reproduced by the simulations well and the appearing discrepancies could be attributed to uncertainties in the underlying experimental parameters. Therefore, our approach will serve for a better understanding of experimental situations, where SCEs occur and allows a discussion of more general aspects of SCEs in PES.

These general aspects are discussed in detail for the two distinct PES experiments, the core–level spectroscopy and the valence–band spectroscopy (e. g. ARPES). Within a wide parameter range the focus was laid on the most crucial parameters, the spot diameter and the number of electrons, in other words: the linear electron density. The pulse duration (as long as smaller than 100 ps) as well as the kinetic energy is of much less importance for SCEs. Predominantly, in the simulations an isotropically emitted electron cloud is assumed. More forward directed emission angle distributions lead to larger effects in energy shift and broadening. Especially, a cosine distribution would cause an increase of SCEs of 20 % – 30 %. The influence of mirror charges in the SC simulations is a more compensating one. The neglection of mirror charges would increase the effect by about 50 %.

Two models from the literature trying to explain the found SCEs in recent PES experiment are compared with our simulation results. The model of Long et al. works reasonably accurate for the energy broadening and reflects the linear dependency from the linear electron density very well, though deduced from quite simple assumptions. The mean–field model from Siwick et al. turns out to be valid only for very low kinetic energies (≤ 1 eV) and for fs–pulses, but seems not to be sufficiently correct and adaptive for higher kinetic energies. Finally, a number of rules of thumb are given for the experimentator to work with:

1. For XPS and required energy resolutions of ≤ 50 meV the linear electron density should always be less than 10000 e^-/mm.

2. In case of high resolution ARPES experiments with energy resolution of smaller than 5 meV the limit to relevant SCEs lies at ≈ 3000 e^-/mm.

3. The momentum broadening effect in ARPES experiments due to Coulomb forces is less critical and can additionally be prevented by using higher kinetic energies due to the inverse proportionality of the effect to the square root of E_{kin}. For a momentum resolution better than 0.01 $\mathring{A}^{-1}$ and a spot diameter of 1 mm the limit lies at 10000 e^- per $\sqrt{eV}$.

In conclusion, Coulomb interactions between electrons can be the limiting factor in PES with regard to the energy resolution and (to a lesser degree) to the momentum resolution. The ongoing development of photon sources towards higher intensities and sharper foci makes these effects even more relevant and problematic for the experiment. Flux variations common for 3^{rd} generation synchrotron sources without top–off mode and FELs with SASE make PES experiments additionally complicated due to intensity dependent and thus varying measured spectra. To prevent these problems the following approach seems to be obvious for PES experiments free from SCEs: One has to combine high–repetition, low–pulse–intensity laser sources with high–resolution spectrometers. To further improve the detection efficiency – and thereby compensating the loss due to the lower pulse intensities – the detection of a wide energy range and solid angle in parallel is beneficial.

7 First photoemission experiments at FLASH

7.1 Introduction

In the last decades, the experimental method of photoelectron spectroscopy (PES) evolved into one of the most powerful tools to study the electronic structure of atoms, molecules and solids [1]. Especially the ongoing developments in the area of photon sources, electron spectrometers and techniques for sample preparation as well as variations to the originally used PES technique, only measuring the kinetic energies of the emitted electrons over the whole hemisphere, helped to understand a variety of mechanisms in solid–state physics. These are for example angle–resolved photoemission (ARPES) [115,119–122], time–resolved pump/probe [123, 124] or spatially–resolved experiments [125, 126]. Today, on the spectrometer side energy resolutions down to sub meV and angular resolution < 0.05 ° are reached [37, 38]. Conventional 3^{rd} generation synchrotron radiation sources deliver polarized, partly coherent photon pulses with pulse lengths of several 10 ps and repetition rates in the sub GHz regime. To perform time–resolved photoemission, modern laser systems exceed the parameters of synchrotron radiation sources concerning pulse length (fs regime), coherence and peak intensity, but are limited in the photon energy. Photon energies in the EUV range can be achieved by using the generation of higher harmonics in a nonlinear medium at the cost of intensity and energy resolution [6–9].
Free–electron lasers (FELs) – such as FLASH (**F**ree **E**lectron–**Las**er in **H**amburg) or the LCLS (**L**inac **C**oherent **L**ight **S**ource) in Stanford, USA – are sources connecting the advantageous characteristics of synchrotron radiation sources and modern laser systems within one facility. Currently, FLASH is regarded as the most brilliant (peak brilliance: 10^{29}–10^{30} photons/(s mrad^2 mm^2 0.1 % bandwidth) synchrotron radiation source in the vacuum ultra violet range (wavelength range of the fundamental: 4.12 – 30 nm) [11, 127]. The machine produces very intense ($\approx 10^{13}$ photons per pulse) and ultra short (some ten fs) light pulses of nearly total transverse coherence using the principle of Self Amplified Spontaneous Emission (see subsection 4.1) [10, 128–130].
These outstanding pulse characteristics of FEL pulses are well usable for the following photoemission experiments:

- **Time–resolved pump/probe experiments:** The photon energies up to the X–ray regime (950 eV with the fifth harmonic) provide the opportunity to do ultrafast pump/probe core–level spectroscopy. By now, ultrafast pump/probe core–level spectroscopy was only possible by using higher–order harmonic generation (HHG) of ultrafast and intense laser radiation delivering discrete photon energies < 100 eV [110, 131–135] (and with significant loss of intensity up to 280 eV [8]) . Furthermore, for ARPES higher photon energies and, thus, higher kinetic energies of the electrons mean that a larger area in the reciprocal space is reachable for temporal studies.
- **Nano–ARPES:** Focusing the coherent and intense free-electron laser radiation down to the nano–scale by using diffraction optics like Fresnel zone plates [19] or photon sieves [20, 21] delivers the possibility to perform spatially– and angle–resolved photoemission spectroscopy in order to study the electronic structure of heterogeneous surfaces.
- **Time–resolved nano–ARPES:** Also a combination of the two above mentioned techniques is thinkable. At the moment, it is not practicable because the number

of pulses delivered by the machine are too few (< 4000 per second), making time–resolved experiments with sufficiently high temporal resolution too time consuming.

- **Photoemission at high fields:** A further interesting research field is to study the influence of high photon intensities on the momentum resolved electronic structure as well as on the photoemission process itself. Furthermore, it has to be considered that Fermi's Golden Rule might not be valid any longer, because for this approximation the assumed perturbation has to be small.

To realize the photoemission experiments mentioned above, one has to deal with one major problem. The huge amount of photons at FLASH are emitting as many electrons from the solid surface that their interaction can not be neglected any longer. The resulting space–charge effects (SCEs) are influencing the spectra in an observable way [22–24]. Specific spectral features are broadened and are typically shifted to higher kinetic energies. Dependent on the material properties, one also has to take into account mirror charges or a possible positive charging of the sample for metals and insulators, respectively.
The phenomenon of space–charge effects are intensively observed and studied in the field of developing electron guns for time–resolved electron diffraction experiments [101–105]. In photoelectron spectroscopy, space–charge effects have also been studied for more than a decade [22–24, 108–111]. The observed effects ranged from $\approx$ 10 meV at 3^{rd} generation synchrotron radiation sources [22], over $\approx$ 100 meV with femtosecond intense laser systems [23] up to $\approx$ 1 eV in first reported photoemission experiments on solid surfaces at FLASH [24]. Several approaches of describing the measured energetic shifts and broadenings of spectral features have been made in the literature, going from a mean–field model, assuming a homogeneously charged disc as the electron distribution [23, 105], over a simple Monte–Carlo based simulation [22], to N–body simulation, e. g. using the Astra (A Space Charge Tracking Algorithm) code [24], originally developed for tracking relativistic electron bunches travelling through a synchrotron radiation beamline [136]. All these approaches conform with the experimental data quite satisfactory, but they are either too time–consuming (like the N–body simulation), or do not model the experimental situation in a physical realistic way (like the electron disc, only valid for electron guns). Thus, they are not universally applicable.
In [25], we have demonstrated a practicable solution, on the one hand, to investigate general limits for specific photoemission experiments for avoiding vacuum space–charge effects, and on the other hand, to describe SCE distorted spectra sufficiently well and within acceptable computational time. This is done by using a modified self-consistent N-body simulation based on the Barnes & Hut Treecode Algorithm [26], originally developed for gravitational N–body problems (stellar motions), where the computational time needed for a simulation grows as $\propto \mathrm{N} \log \mathrm{N}$ and not with N^2.
In the following, selected results of our first photoemission experiments at FLASH will be presented. First of all, we will answer the question if our used samples will suffer any damages caused by the high pulse intensities of FLASH during our photoemission measurements. Furthermore, we will demonstrate that, in general, angle–resolved photoemission at FLASH is possible up to an intensity limit, determined by the occurring SCEs and the spectral features, one wants to resolve. Finally, we will show by means of core–level spectra, measured as a function of photon density, that our modified Treecode Algorithm [25] describes the SCE–influenced data very well; and hence, with these numerical simulations applied to valence band measurements spectral changes due to physical processes inside the

solid can be separated from the changes caused by the Coulomb repulsion outside the solid. Therefore, future time–resolved pump/probe experiments at FLASH could be performed in a regime, where SCEs start to be pronounced. Furthermore, applying this method opens the door to study the influence of high excitation intensities in angle–resolved photoemission, where SCEs will definitely be present.

7.2 Experimental setup

Our photoemission experiments were performed at the plane grating monochromator PG2 at FLASH [78, 79, 137] delivering highly intense monochromatic VUV–pulses (see Fig. 5.8). FLASH was operated in the multi pulse mode, generating pulse trains containing 20 micro pulses of 7–50 fs duration (before monochromatizing) separated by 1 μs and with pulse energies up to 100 μJ. The fundamental photon energy was set to 38.5 eV with a bandwidth of 0.5 % to 1 %. After monochromatizing, the delivered photon energy resolution was better than the energy resolution of the used electron spectrometer mode and due to a pulse stretching within the monochromatizing process in the plane grating monochromator the pulse length was increased to about 700 fs [78, 100]. For our valence band and core–level measurements, we have used photon energies of 38.32 eV and 115.5 eV (3^{rd} harmonic of FLASH), respectively.

One experimental challenge for performing PES at FLASH lies in the principle of the generation of FEL radiation by SASE itself: Every single FEL pulse is different due to the start up of the amplification from noise, i.e., one has to deal with pulse intensity fluctuations as well as with varying photon energies within the bandwidth of 1 %. Due to that, monitoring of FEL pulse intensities for every single shot is essential. This was done for the core–level measurements either by monitoring the photocurrent generated in a gold mesh positioned in front of the experimental chamber, or by the MCP detector described in subsection 5.1.2. Here, the latter was used to approximate the number of photons within every micro pulse with an accuracy of ± 79 % (cp. subsection 5.1.2). The large error is due to systematic uncertainties in the calibration procedure as well as the fact that the MCP–tool was calibrated for a different photon energy of 38.5 eV [89].

The photoemission spectra were taken with a SPECS PHOIBOS 150 electron analyzer equipped with a 2D–CCD detector for parallel detection of electron energy and emission angle. The CCD camera (Basler A102f for ARPES, PCO Sensicam qe for core–level PES) was synchronized with the FEL repetition rate and took pictures of the phosphor screen for every pulse train. This means, that every CCD image actually is a sum of 20 spectra belonging to different single pulse intensities. Thus, it was only possible to sort the images according to their average pulse intensity within one pulse train. We have also performed PES in the single pulse mode, i.e., one pulse train consisted of one single photon pulse. But because of the intrinsically low repetition rate of the FEL (5 Hz), one hardly got acceptable statistics for selected intensity intervals. The total energy resolution was limited to the resolution of the electron analyzer. In order to get a sufficient counting rate on the CCD detector, the energy resolution was set to < 700 meV (E_{pass} = 200 eV, s_{Ana} = 1 mm) and < 140 meV (E_{pass} = 200 eV, s_{Ana} = 0.2 mm) for ARPES measurements and core–level spectroscopy, respectively. The photoemission spectra as well as the intensity information are saved via the FEL data acquisition system DOOCS (**d**istributed **o**bject **o**riented **c**ontrol **s**ystem) with a so–called "timestamp", that is unique for every pulse

train. Afterwards the spectra had to be sorted according to the photon intensity and were summed to obtain acceptable statistics.
As samples, we used the layered transition metal dichalcogenides (TMDCs) $1T$–TiTe$_2$ at room temperature (semi–metal) and $1T$–TaS$_2$ cooled down to ≈ 140 K using a manipulator cryostat (VG Cryoax 6) for cooling with liquid helium. Both TMDCs crystallize in the $1T$–CdI$_2$ structure (space group D^3_{3d}). A clean sample surface is delivered by cleaving the crystals under ultra high vacuum condition with a base pressure of $< 10^{-9}$ mbar. $1T$–TiTe$_2$ has an extensively studied valence band structure [60–66], so comparisons with the results from angle–resolved photoemission at the FEL might be easy. $1T$–TaS$_2$ is a very interesting charge–density wave (CDW) system, showing a metal–to–insulator phase transition by cooling below 180 K [46, 55, 56, 138] or by adsorption of alkali metals [54]. Recently, interesting time-resolved pump/probe PES experiments have been performed on insulating $1T$–TaS$_2$, inducing a transient transition into a metallic phase by pumping the sample with 800 nm fs–laser laser light [55, 56]. The induced dynamics (CDW–oscillations) were predominantly studied by valence band photoemission spectroscopy with frequency doubled fs–lasers as well as by reflectivity measurements [70, 71]. Now FLASH, reaching photon energies in the VUV regime with pulse widths of some 100 fs, delivers the possibility to perform core–level photoemission on Ta $4f$ core–levels, giving further insights into the mechanism of the observed CDW–oscillation and its influence on the Ta atom position.

7.3 Radiation damage

In order to exclude, that the samples suffered any severe radiation damage during the photoemission measurements with the highly intense FEL radiation, we took images of each sample with an optical microscope afterwards. The samples without indications of radiation damage were treated very carefully with moderate intensities in the monochromatized first order light of 38.5 eV or at even lower intensities in the third harmonic of the FEL radiation. In figure 7.1(a) the microscopic image of a $1T$–TiTe$_2$ sample, illuminated by zero order FEL light ($1 - 10$ μ J pulse energy) for several hours, is presented showing indications of radiation damage. The observed triangular structures have had typical edge dimensions of about 10 μm and have been found only on samples, which were exposed to zero order light and high pulse energies. Additionally, Laue diffraction measurements revealed that the triangular structures are aligned with the high symmetry directions representing the threefold symmetry of these crystals. Furthermore, the microscopic image shows an agglomeration of the triangles at step edges or cracks of the crystal. Thus, structural defects seem to be the preferred site for the formation of these triangular structures.

The nucleation and growth of submicron complex structures on TMDCs have been observed and discussed in a variety of publications, all using the technique of scanning tunneling microscopy (STM) [140–144] or atomic force microscopy (AFM) [139]. In case of NbSe$_2$ [140] and WSe$_2$ [139, 142–144] subsequent growth of triangular holes have been found under normal scanning conditions of typically $0.6 - 1.5$ V negative tip bias and 0.1 – 5 nA tunneling current in ambient air. The nucleation seemed to prefer defects, already present on the surface or being induced by short voltage pulses of $5 - 7$ V negative tip bias and pulse widths ranging from 10 ns to 10 μs. In figure 7.1(b), the evolution of triangles on WSe$_2$ of monolayer depth (approximately 6.5 $\mathring{A}$) is shown by AFM with an applied bias voltage of 1.2 V [139].

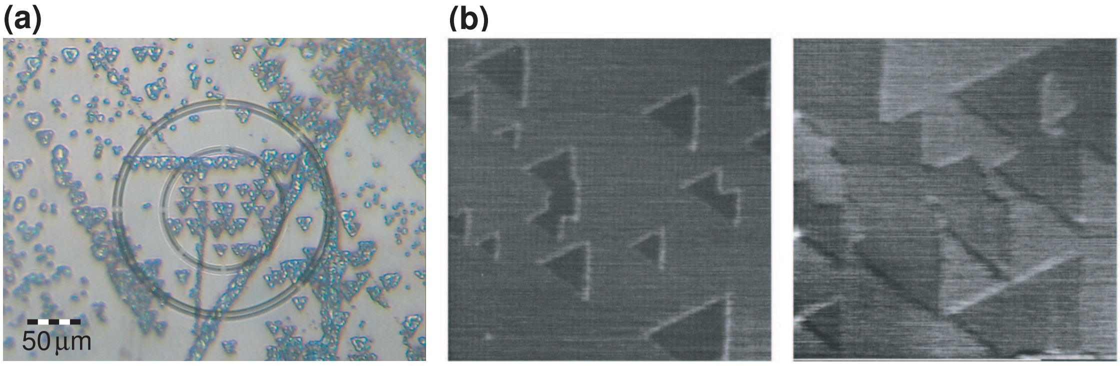

Figure 7.1: (a) $1T$–TiTe$_2$ after 10 h exposure to zero order FEL radiation (pulse characteristics: E$_{pulse}$ = $1 - 10$ μJ, some fs pulse duration, hν = 38.5 eV, 40 pulses per second). (b) AFM image of a triangular defect structure on WSe$_2$ induced by scanning with an applied bias voltage (image sizes: 500×500 nm^2) (from [139]). The triangles were growing during the scanning procedure.

Parkinson *et al.* specified four reasonable mechanisms for explaining the growth of holes as an etching process on $2H_a$–NbSe$_2$. A fifth possible mechanism was added and intensified by several publications about WSe$_2$ [139, 143, 144]:

1. Radicals are generated from organic impurities on the surface due to the electric field and current flow. The favorable reaction site of these radicals are defects and step edges.

2. The etching is related to the heat or power dissipation in the tip region. Calculations for more extreme tunneling conditions (2V and 10 μA) have shown a distinct increase in the surface temperature of up to a few 100 K [145].

3. The electronic bonds are strongly influenced by the electric field leading to field assisted evaporation of atoms or molecules. This process is exploited in ion microscopy using field strengths of several V/$\AA$ [146–148]. In STM, one would estimate a value of some tens of V/$\AA$. However, evaporation of atoms from ionic NaCl crystals have been observed even with electric fields of $< 3\times10^{-5}$ V/$\AA$ supported by heating the sample to approximately 800 K [149]. Therefore, the temperature has an effect on the evaporation rate constant k according to the Arrhenius formula [150]:

$$k = A \cdot e^{-E_A/k_B T} \tag{7.1}$$

   where A is a prefactor, E_A is the activation energy, k_B the Boltzmann constant and T the temperature in Kelvin.

4. Direct contact between the tip and the sample abrases the surface.

5. Boneberg et al. [143] ascribe the subsequent growth of triangular holes on WSe$_2$ to a corrosion process due to water molecules on the surface as well as holes (h^+) created by the positive sample bias leading to the following reaction formula:

$$WSe_2 + 9H_2O + 14h^+ \rightarrow WO_3 + 2SeO_3^{2-} + 18H^+$$

> This corrosion reaction prefers non van–der–Waals surfaces, which is given for example by defects or step edges. Further studies of Enss et al. [144] and Böhnisch et al. [139] affirmed this etching mechanism.

Though, the experimental conditions for the above mentioned STM / AFM measurements are quite different from the conditions in our experimental chamber, they can help to understand the processes leading to similar observed triangular structures, even if these are two orders of magnitude larger at the FEL. Mechanism (4) can obviously be excluded due to the absence of a tip in our experiment. Because of cleaving the samples in ultra high vacuum and, thereby, getting surfaces nearly free from contaminations, mechanisms (1) and (5) are not very probable as well. In the following, we will check the influence of sample heating (mechanism (2)), field assisted evaporation (mechanism (3)) or other possible mechanisms leading to the observed triangular structures on $TiTe_2$. To this end, we will generally follow the processes in the solid from excitation with a highly intense and some ten femtosecond long FEL radiation pulse to relaxation within 1 μs until the next micro pulse arrives during the multi pulse mode.
The $TiTe_2$ sample shown in figure 7.1(a) was illuminated by zero order FEL radiation for several hours. The pulse energy E_{pulse} of the micro pulses could reach up to 1 – 10 μJ. With an assumed Gaussian spot size of 395 μm × 274 μm [79] and a temporal pulse width of 10 – 100 fs, an energy flux of 10^{10} – 10^{12} W/cm^2 was possible at PG2. Accordingly to the time–averaged magnitude of the Poynting vector $\langle S \rangle$, representing the energy flux,

$$\langle S \rangle = \frac{\epsilon_0 c}{2} E_0^2 \quad ,$$

where ϵ_0 is the electric constant, c is the speed of light, and E_0 is the maximum of the electric field in the propagating electromagnetic wave, a maximum amplitude of the electric field of 27.5 –275 mV/$\AA$ during the excitation could be delivered. This value is comparable to the values approximated in [140] for STM induced hole growth on $NbSe_2$. During the STM measurements, the electric field was constantly present and the growth process took place in terms of minutes and hours. Due to the pulsed character of FEL radiation, the electric field was only present at the surface for at most 10^{-11} of that time in the multi pulse mode (40 photon pulses with 100 fs duration). So, it is quite improbable, that field assisted evaporation is the only mechanism for hole growth on our $TiTe_2$ surfaces. Another mechanism must assist the development of holes up to μm–size with such ultra short pulses.
One possible answer to this question can be found in the deposited pulse energy within a small region at the surface. The incident photons are typically absorbed by the electronic system. Calculating with an average photo ionization cross section of ≈ 2.088 Mb for $TiTe_2$ at 38.5 eV [151] and an atomic density of $\approx 3.75 \times 10^{28}$ m^{-3} [152], one gets a penetration depth of the radiation of approximately 127 nm. Photoelectrons with enough energy are able to leave the sample with a certain probability determined by the electron inelastic mean free path [153]. The remaining majority of excited carriers are gradually redistributing their energy via different processes like carrier–carrier and carrier–phonon scattering. Finally, phonon thermalization results in an increased lattice temperature within the first 10 ps after excitation with the FEL pulse [2, 154, 155].
In figure 7.2(a) the calculated heating ΔT of the sample per μJ incident pulse energy is shown in a cut through the x–z–plain (z depicts the direction of the surface). For this, a Gaussian spot size of 400 μm × 300 μm, a penetration depth of 128 nm and a classical heat capacity of $3 \cdot R$ is assumed, where R is the ideal gas constant. Moreover, the total

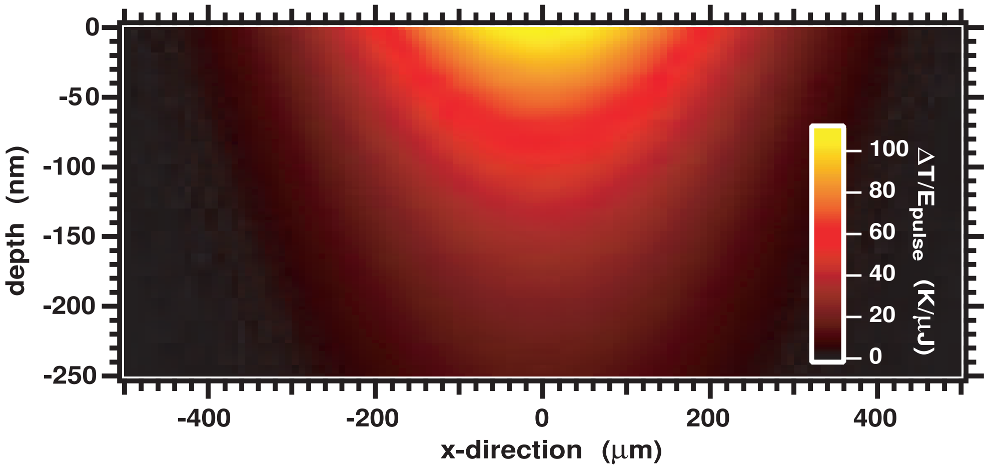

Figure 7.2: Simulated heating of a $TiTe_2$ sample per incident pulse energy ΔT / E_{pulse} (cut through the x–z–plane) assuming a penetration depth of the photons of 128 nm, a two–dimensional Gaussian spot of 400 μm × 300 μm FWHM, a heat capacity of $3{\cdot}R = 25$ J/(mol·K) and a complete relaxation of the deposited energy into thermal energy.

incident energy is assumed to dissipate into heat by the above mentioned processes. Carrier diffusion in the solid, occurring on longer time scales (up to a few 10 ps), can be neglected. Loss of energy due to photoelectrons leaving the solid can be neglected as well. This would affect the first few layers because of their short inelastic mean free path and thus, would only smoothen the temperature distribution at the surface. The calculations delivered that at the given spot size and a pulse energy of 1 μJ one can reach an increase of temperature of about 100 K near the surface in the center region of the spot. Thus, the $TiTe_2$ sample could be heated up to 1000 °C taking into account the maximum pulse energy of 10 μJ. The melting point of $TiTe_2$ is estimated to be 1200 °C [152] though, evaporation of Te atoms was observed at even lower temperatures (≈ 800 °C). Obviously, melting and recrystalization of the solid can not be achieved by only one single pulse. Non–thermal evaporation of atoms, molecules or clusters from the surface, also referred to as ablation [156,157], seems not to be the mechanism for triangular hole growth either, because ablation typically leaves a crater at the surface with the shape of the lateral spot profil.

Finally, the use of several pulses in one pulse train separated by 1 μs has to be taken into account in terms of successive sample heating. For this, one has to follow the temporal evolution of the induced temperature distribution by thermal diffusion. The diffusion of heat from regions of high temperature to regions of low temperature can be described by the following differential equation:

$$\frac{\partial}{\partial t}T(x,y,z,t) = \nabla(D_T \nabla T(x,y,z,t)) \tag{7.2}$$

where $T(x,y,z,t)$ is the time and spatial dependent temperature distribution and D_T is the thermal diffusion constant. The thermal diffusion constant can be determined by

$$D_T = \frac{\lambda}{\rho\ c_p} \tag{7.3}$$

using the thermal conductivity λ, the specific heat c_p and the mass density ρ. As can be seen in figure 7.2, the temperature gradient and, consequently, the thermal diffusion is

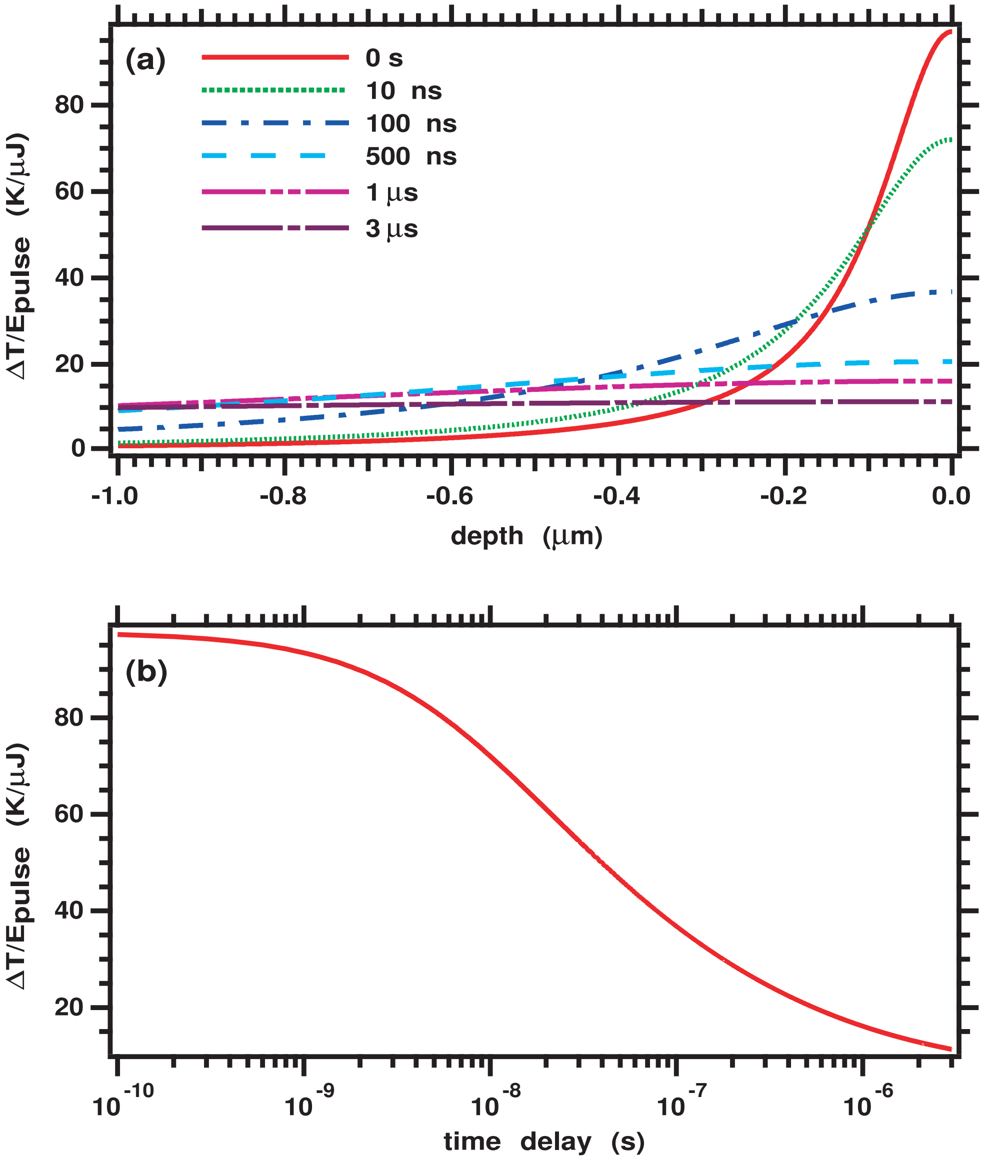

Figure 7.3: (a) Simulated temporal evolution of the initially FEL pulse induced heating distribution (from figure 7.2) in z–direction of the $TiTe_2$ sample using the differential equation (7.2) with the thermal diffusion constant of 0.35×10^{-6} m^2 / s and a slightly varying initial Lorentzian depth profil. (b) Temporal evolution of the sample–surface heating in the center of the FEL spot $\Delta T(0,0,0,t)/E_{pulse}$ as a function of delay time.

stronger perpendicular to the surface. For simplification, we will limit our considerations to this dominant direction. Due to the metallic behavior of $TiTe_2$, one can approximate the thermal diffusion constant perpendicular to the surface to $\approx 0.35 \times 10^{-6}$ m^2 / s, taking into account an electrical resistivity parallel to the surface of $10.4{\cdot}10^{-5}$ Ωcm(from [60]) and the Wiedemann–Frantz law, as well as an anisotropic relation between the electrical resistivities parallel and perpendicular to the surface of approximately 40 [66]. In figure 7.3(a), the evolution of the pulse induced heating distribution in z–direction is shown as a function of time, while in figure 7.3(b) the evolution of $\Delta T(0,0,0,t)/E_{pulse}$ can be followed. Here, a Lorentzian start–temperature distribution was chosen, matching the exponential decay into the solid best, but smoothened at the surface. The result of the calculation is an obvious diffusion of heat into the depth of the solid, continuing up to more than 1 μs. At $t = 1$ μs, still more than 10 % of the initial heating is left at the center of the impact spot; i. e., for the operation with 20 micro pulses, a successive heating of the sample up to several 100 °C and even higher than the melting point of TiT_2 is thinkable (e.g. 20 micro pulses with 10 μJ pulse energy each). This would increase the evaporation rate due the strong fields of the later pulses in the pulse train by several orders of magnitude considering the Arrhenius formula (7.1). Furthermore, melting and recrystalization seems to be possible as well. For both mechanisms, structural defects like step edges would be expected as preferred reaction sites, as observed in the microscope image in figure 7.1(a) as well.

To conclude, two mechanisms are possible candidates for the growth of triangular structures on the surface of TiT_2 due to irradiation with highly intense FEL radiation: On the one hand, field assisted evaporation additionally supported by a successive heating of the solid surface, and on the other hand, superheating followed by transient melting and recrystallization. As a consequence for our PES measurements, we can say, whatever causes the triangular structures, it can be prevented by using moderate and monochromatized FEL radiation, anyway essential for solid–state photoemission.

7.4 Space–charge effects in angle–resolved photoemission

We have performed intensity dependent ARPES measurements on $TiTe_2$ in the single pulse mode as well as in the multi pulse mode at FLASH [27]. Here, only the angle-resolved data from the measurements in the multi pulse mode will be presented due to the better statistics. The light intensity was in first approximation controlled via the monochromator exit slit width d; nonetheless, because of intensity fluctuations within one pulse train, the resulting spectra consist of a mixture of differently space–charge influenced single spectra. The monochromator exit slit width was changed between 32 μm and 72 μm with steps of 5 μm.

The results of our first valence–band PES are shown in figure 7.4. At lowest intensity (d = 32 μm), three bands are visible in normal emission (0 eV, 2 eV, 4 eV) as well as a weak electron signal from the Fermi level (dashed circle in the angle integrated spectrum). These bands agree very well with the Te 5p derived bands around the high–symmetry point A of the Brillouin zone gained from band structure calculations [65]. As a guide to the eye, the corresponding bands are plotted in the first and the last angle–resolved spectra in figure 7.4. With increasing average pulse intensities, respectively larger exit slit width, a strong broadening of the spectral features and a continuing shift towards lower binding energies, corresponding with higher kinetic energies, can be observed. At d = 57 μm, the bands are no longer separable and the spectrum is shifted by more than 1 eV.

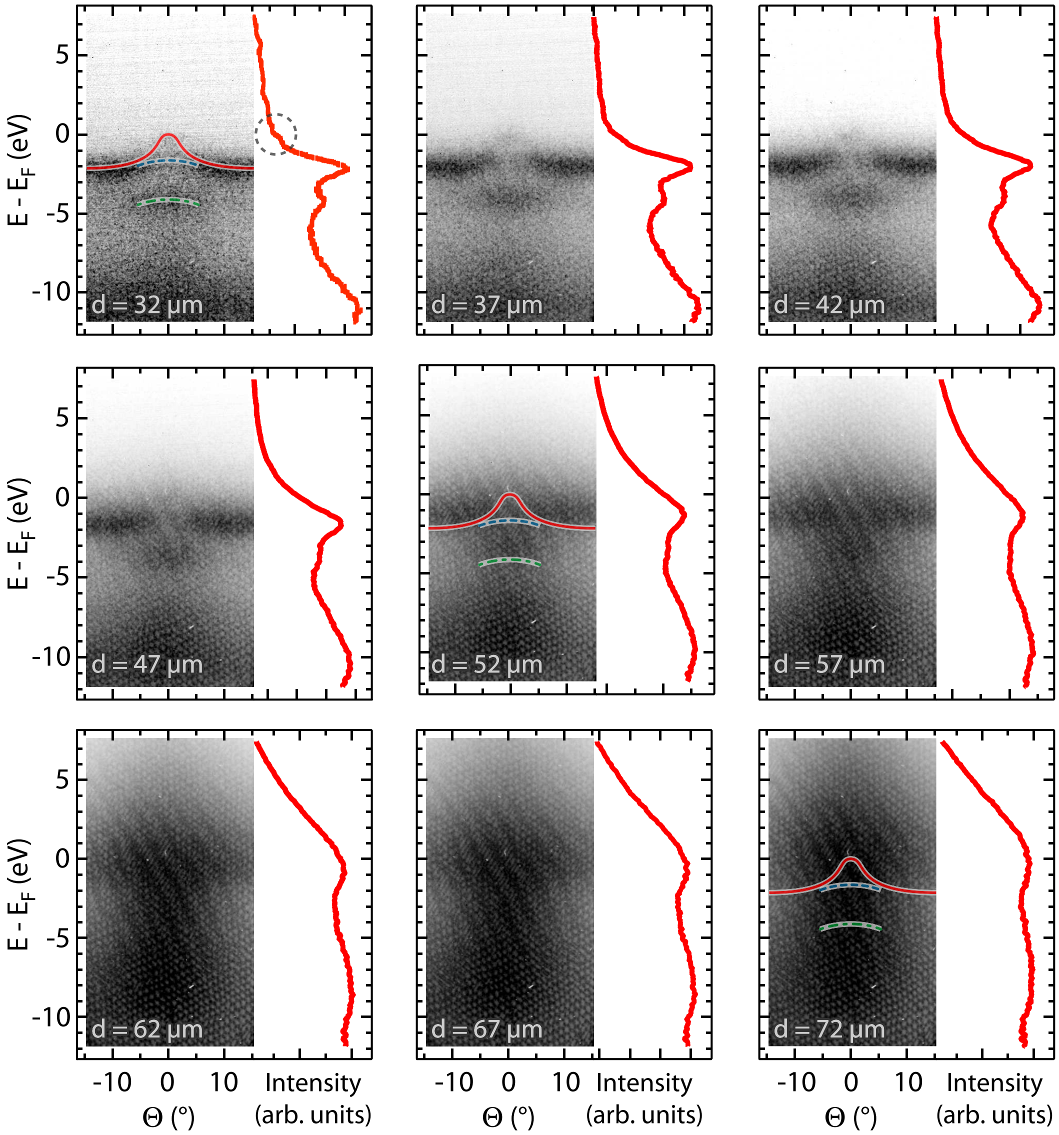

Figure 7.4: Angle–resolved valence band spectra (hν = 38.32 eV) of 1*T*–TiTe$_2$ measured with 20 micro pulses per FEL bunch, sorted by different monochromator exit slit widths d (from Ref. [27]). Illustration by gray scale image (black indicates high intensity). Beside each angle–resolved spectra the angle–integrated spectra (solid red lines) are shown. Additional lines in the first (d = 32 μm) and the last (d = 72 μm) gray scale image indicate the Ti 3d$_{z^2}$– and two Te 5p–derived bands (solid red, dashed blue, and green lines, respectively). The gray circle in the first image indicates the position of the Fermi edge.

Further increase of intensity leads to totally blurred and shifted spectra with no more useful information about the original band structure. The reason for the observed effects on the photoemission spectra are Coulomb interactions between the emitted electrons. The amount of photoelectrons, produced by the intense FLASH pulse, is so huge, so that space–charge as well as mirror–charge effects can not be neglected any longer. The observed energetic shifts and broadenings of the spectral features of up to several eV is comparable to core–level PES measurements on tungsten at FLASH, reported by Pietzsch *et al.* [24]. Further quantification of space–charge effects on the valence band photoemission spectra of $TiTe_2$ seems not to be reasonable, because no accurate intensity information of the radiation pulses behind the monochromator were available at that time (first beamtime period at FLASH).

The presented valence band PES measurements show, that ARPES at FLASH is feasible. However, this is particularly true if the intensity monitoring, developed during this thesis, is used to sort single spectra according to the photon pulse intensities delivered by FLASH. For meaningful interpretations of the spectra in future experiments, a practicable handling and a good understanding of vacuum space–charge effects is essential. Then, the necessary requirements for performing time–resolved pump/probe photoemission experiments at FLASH and studying the influence of high fields on the valence band structure are given.

7.5 Space–charge effects in core level photoemission

In addition to our valence band photoemission measurements on $TiTe_2$ presented in the previous section, using the newly developed intensity monitoring tools (see chapter 5.1) we have also performed core–level spectroscopy at FLASH on TaS_2 to study the influence of high photoelectron densities on the measured spectra more quantitatively. In contrast to valence bands, core–levels are ideal candidates for testing the general feasibility of simulations presented in [25] because of their non–dispersive and, thus, more simple character. The final goal is, to develop a method for the recursive reconstruction of the initial photoelectron spectrum from the one distorted by SCEs.

7.5.1 Experimental data

The measurements were performed on TaS_2 and the Ta $4f$ core–levels were analyzed, while the sample was cooled by liquid helium to a temperature of about 140 K. Below ≈ 180 K, $1T$–TaS_2 is in the insulating, commensurate charge–density wave phase, resulting in a clearly separable four–peak structure of the Ta $4f$ core–levels. In addition to the common spin–orbit splitting into Ta $4f_{5/2}$ and Ta $4f_{7/2}$ of about 1.93 eV at room temperature in the metallic phase [46], in the insulating CDW phase two more peaks with the same splitting are present in the core–level spectrum shifted by about 700 meV to higher binding energies [46, 138]. This is due to the periodic lattice distortion of the Ta atoms in this phase, and, therefore, emerging different chemical environments. This characteristic CDW–splitting can be seen in fig. 7.5(a) in the spectrum with lowest intensity.

In Fig. 7.5 the results of our core–level measurements are presented. Due to the differing character (mainly due to pulse–to–pulse intensity fluctuations) of every FEL pulse train, it was essential to record two types of data. On the one hand, we took photoemission data of TaS_2 for every single FEL shot, i.e., we took 5 CCD images per second because of the bunch repetition rate of 5 Hz. On the other hand, we had to measure the intensitiy of every single pulse in the corresponding pulse train with the MCP–tool, to have a criterion for sorting the CCD images dependent on the average pulse intensity afterwards. The angle of incidence of the photons was set to 45° (p–polarized) and the total number of photons per micro pulse determined by the MCP–tool ranged between 7×10^5 and 7×10^7 ($\pm 79\%$).

The intensity sorted core level measurements show the similar trend as the valence band spectra discussed before (see fig. 7.5(a)). From the spectrum with lowest intensity (bottom spectrum) up to the spectrum with highest intensity (top spectrum), a contineous shift of the spectral features to lower binding energies as well as an increased blurring is observable with increasing amount of photoelectrons. The average number of electrons, displayed on the ordinate, was added after fitting the simulated data to the experimental ones (see below). The primarily sorting into different intensity intervals was done by the raw MCP–data, which are approximately proportional to the number of photons in each pulse.

A quantitative analysis of the energetic shift and broadening by fitting every single peak by Gaussian profils as done by Pietzsch *et al.* [24] for W $4f$ core–levels, seems not to be the method of choice, here: First of all, the Ta $4f$ core–levels show a distinct asymmetry. Therefore, an asymmetric lineshape has to be used. Even more critical is the fact that every summed spectrum consists of a mixture of single pulses with different intensities (though sorted by comparable average intensities). This has to be taken into account in the quantitative analysis of the space–charge influenced spectra.

The mixture of different single intensities can be followed in the 2D–histogram shown in figure 7.5(b). Here, the relative amount of single intensities contributing to the according spectra plotted in 7.5(a) are shown, as well as the average number of electrons in the experiment (gray squares) together with the associated standard deviation (gray error bars). The latter is increasing with increasing average pulse intensity, reflecting the strong intensity variations within every single pulse train. The 1D–histogram on the right side of figure 7.5(b) delivers insight into the required measurement time to get decent statistics. This will be especially interesting for performing time–resolved pump–probe photoemission experiments at pulse intensities, where SCEs can be neglected. The effective measurement time for each intensity channel was less than 15 minutes (except for the first intensity channel) for good statistics in the low intensity regime, taking into account the number of summed micro pulses and the usage of 100 micro pulses per second. Further development of the FEL machine will result in more stable pulse intensities (by seeding [74–77] or by running in saturation) as well as some thousand pulses per second. This will significantly reduce the measurement time, making FLASH a prominent light source for time–resolved PES in the future.

7.5.2 Simulations

The understanding of space–charge induced spectral broadenings and shifts in PES at high photon fluxes is of essential interest, e.g., in the investigation of high–field effects, or the usage of focused radiation to sub micrometer regime in order to study spatially dependent phenomena at the sample surface. In [25], we presented a numerical method to the simulate the propagation dynamics of photoelectrons to the detector. The comparison of these

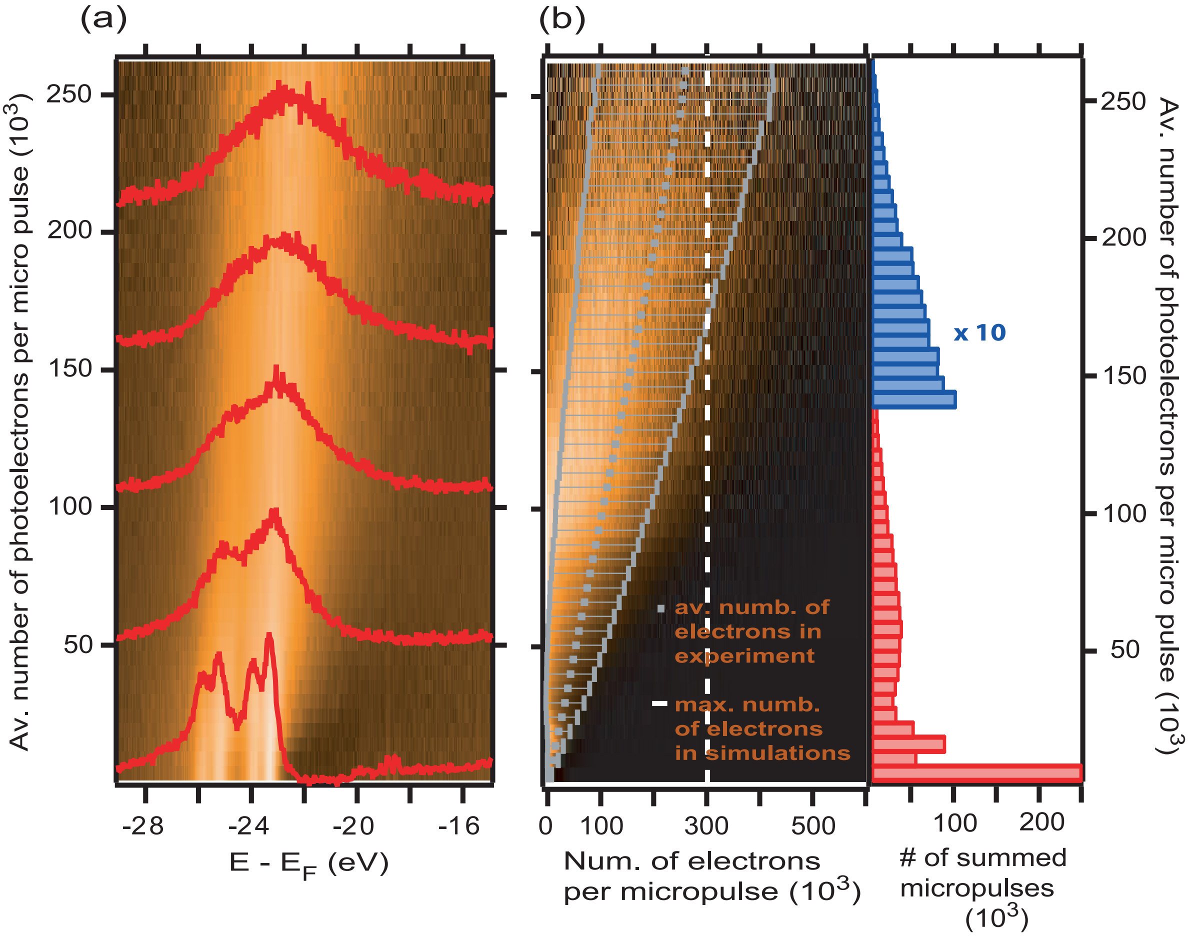

Figure 7.5: Vacuum space–charge effects on a Ta 4*f* core–level spectrum of 1*T*–TaS$_2$ in the commensurate insulating charge–density wave phase (T = 140 K), measured with 20 micro pulses per FEL bunch (hν = 115.5 eV, 3^{rd} harmonic of FEL). (a) Measurements are sorted by the average number of photoelectrons $\langle N_C \rangle$ (determined by the simulations afterwards) per micro pulse going from low (bottom) to high (top) pulse intensities (white indicates high spectral intensity). Additionally, some representative spectra are plotted in red ($\langle N_C \rangle = 3.5k, 53k, 107k, 161k, 213k$). (b) 2D–histogram of micro pulse intensities (false color image) and total number of micro pulses (bar diagram in the right graph) contributing to the spectra in each intensity channel. The average number of electrons per micro pulse as well as the standard deviation are plotted in the 2D–histogram (gray squares with error bars). The dashed white line indicates the maximum number of electrons, simulated with the modified Treecode Algorithm from [25].

simulations were very satisfactory with regard to accuracy as well as universal applicability. In the following, the computational model will be introduced briefly, before the simulation results for the Ta $4f$ core–levels are presented. Finally, the quality of the simulation results will be identified by comparing those with the experimental data taking into account the mixing of spectra with different pulse intensities regarding the 2D-intensity histogram in fig. 7.5(b).

In a typical solid-state photoemission experiment, the photon pulse is absorbed in a certain volume near the surface of the sample. Photoelectrons are emitted from the surface into the vacuum, and successively a cloud of electrons is created in front of the sample. The phase-space distribution of the emitted electrons is determined by the parameters of the light pulse, these are the number of photons, the pulse duration, the pulse profil and the photon energy. Together with material specific aspects of the photoemission process the result is an initial kinetic–energy and angular distribution of the electrons in the cloud starting their propagation to the detector.

In our simulations of space–charge effects we have to handle a huge amount of photoelectrons (up to some 10^5). The Barnes & Hut Treecode Algorithm [26] (originally developed for gravitational N–body problems) enables us to reduce the computational time as much as possible while simultaneously delivering quite accurate results. This self-consistent N–body algorithm computes the interaction between particles and the resulting propagation dynamics using leap–frog integration. The computational time needed for simulation grows as $\propto$ N log N and not with N^2. This is due to the partitioning of space into a hierarchical tree structure and calculating the mutual Coulomb forces by center–of–mass approximation. (More details concerning the computational model are given in [25].) In [25] we have reported of the implemented modifications to use this algorithm for simulating vacuum space–charge effects in photoemission and showed the applicability to already performed space–charge influenced photoemission experiments as well as general limitations to PES due to SCEs.

In the simulations of space–charge effects, a cloud of a specific number of electrons ("cloud electrons") is created within the pulse duration $\tau_{h\nu}$. The electrons are generated at random times during $\tau_{h\nu}$, from random position in the spot size on the surface and with random kinetic–energy and angular distribution. The temporal and spatial spot profils are mostly assumed to be Gaussian with width of $\tau_{h\nu}$ and d_{0x} (and d_{0y}, if the spot profil is elliptical) [full width at half maximum (FWHM)], respectively. The kinetic–energy ($E_{kin,cloud}$) and angular (ϑ_{cloud}) distribution of the starting cloud electrons are chosen as realistic as possible. This is mainly dependent on experimental parameters and their influence on the photoemission process itself, e.g., the photon energy, polarization, incident angle of the light wave, and of course the electronic band structure of the sample. For this, it might be useful to measure a complete set of angle–resolved PE data as a reference and use these for the simulations.

To increase the simulation efficiency and, thereby, to get better statistics for one specific space–charge influenced part of the spectrum, we introduced "test electrons" in addition to the cloud electrons. The number of these "virtual" electrons is typically about 10^4 per simulation run. They are generated in the same way as the cloud electrons, but with differing kinetic energy $E_{kin,test}$, dependent on the region of interest in the spectrum) and angular ((ϑ_{test}), typically in forward direction to the detector) distributions. Furthermore, the test electrons have no contribution to the space charge, i.e., they neither influence the cloud electrons nor themselves by Coulomb forces, but they are influenced by the cloud electrons.

Table 7.1: Parameters for the simulations (with the modified Treecode Algorithm from [25]) of space–charge influenced Ta 4*f* core–levels as a function of the number of photoemitted electrons per pulse. The simulation results are shown in figure 7.6.

Simulation parameters:	
spot size $d_{0x} \times d_{0y}$	$270 \times 400\ \mu m^2$ (FWHM) [a]
pulse duration τ_0	700 fs (FWHM) [b]
($E_{kin,cloud}$)–distribution	TaS_2 spectrum measured at MAXLAB with $h\nu = 120$ eV, T = 300 K, $\vartheta = 47.5°$; spectrum shifted -4.5 eV and secondary electrons estimated as shown in 7.5(b).
(ϑ_{cloud})–distribution	cosine function by simple estimations considering the electron inelastic mean–free path.
($E_{kin,test}$)–distribution	spectrum with lowest average intensity in fig. 7.5(a)
(ϑ_{test})–distribution	detection angle of the spectrometer : ± 13°
photon energy $h\nu$	115.5 eV
number of cloud electrons per pulse N_C	1000 – 300000; $\Delta N_C = 1000$
mirror charges	neglected!

[a] from Ref. [79]
[b] from Ref. [100]

As found out by Zhou et al. [22], mirror charges seem to contribute to the spectral distortion as well, at least for metallic surfaces. These mirror–charge effects can optionally be regarded in the numerical simulations.

The simulation run is stopped, when the total Coulomb energy in the electron cloud becomes negligible. Then the final kinetic–energy and momentum distributions are achieved. Finally, the simulation procedure is repeated several times to avoid errors due to accidentally unfavorable starting conditions.

To simulate the photoemission measurements of the Ta 4*f* core levels at FLASH, we have chosen simulation parameters as realistic as possible, though we have not had the possibility to experimentally check the real spot size, pulse duration and energy– and momentum distribution of the photoelectrons over the complete hemisphere. Nevertheless, we have shown in [25] that the space–charge induced spectral broadening and shift can be assumed to be proportional to the number of photoelectrons per pulse N_C, while the other parameters are kept constant. Thus, the resulting numbers of electrons in our photoemission experiment in fig. 7.5(a), determined by the simulations in the following, may differ from the real one. This will not downgrade the principle applicability of our numerical simulations to the experimental dataset. The real number of photoelectrons during the experiment may solely differ by a constant factor.

The used simulation parameters are summarized in table 7.1. The spot size on the sample is assumed to be $270 \times 400\ \mu m^2$ (FWHM) [79] while the pulse duration for the used monochromator settings was calculated to be 700 fs (FWHM) [100]. For the kinetic–energy distribution ($E_{kin,cloud}$), a photoemission spectrum was chosen measured with a photon energy of 120 eV and a detection angle of 47.5° at room temperature. The spectrum was shifted by 4.5 eV towards lower kinetic energies before using it in the simulations (photon energy in our experiment: 115.5 eV) and a slightly increasing secondary–electron background was assumed. The cloud–electron energy distribution is shown in figure 7.6(b) and was emitted over the whole hemisphere. Matrix–element effects and the dispersion of valence bands are neglected here, but the energy–distribution was weighted by a (ϑ_{cloud})–distribution proportional to the cosine of the polar angle ϑ_{cloud}, obtained by simple estimations from the inelastic mean–free path of the electrons in the sample. For the test electrons, we used the experimental spectrum with lowest average intensity from figure 7.5(a) as the starting kinetic–energy distribution ($E_{kin,test}$) and we are only interested in the electrons propagating to the detector in a cone of $\vartheta_{test} = \pm\ 13°$. As we are measuring the Ta 4*f* core–levels of TaS_2 in the insulating phase, we turned off mirror charges in the simulations. Finally, the simulations are performed with 1000 – 300000 cloud electrons per pulse in steps of 1000.

The results of our simulations with the Treecode Algorithm are shown in figure 7.6(a). Again, starting with small numbers of electrons per pulse (bottom), with increasing N_C the characteristic shift and broadening of the Ta 4*f* core–levels are observed. The additionally displayed spectra in the false color image clearly show the tendency from the still resolved four–peak structure at low intensities, over a blurred and shifted two–peak structure at medium intensities, finally ending in one broad peak shifting with increasing N_C at highest intensities.

Now, further quantitative investigations of the simulated space–charge effect are possible, because every simulated spectrum results from a specific number of mutual influencing electrons and no longer from a mixing of strongly varying intensities. The position and width of every single peak are still not easy to determine, neither by fitting simple Gaussian lineshapes as done by Pietzsch et al. [24] nor by more complex asymmetrical lineshapes, especially for the spectra with higher electron intensities. Furthermore, every single Ta 4*f* peak is probably shifted in a slightly different way, because a spatial sorting of the electrons gradually takes place along the way to the detector due to their different kinetic energies and generation at different times during the excitation pulse. Electrons coming from the core–level with lowest/highest binding energy, respectively highest/lowest kinetic energy, will be shifted more/less than the electrons coming from Ta 4*f* core–levels with higher/lower binding energy, because they are additionally accelerated/decelerated by the following/precursory. On the other hand, the electrons from the central core–levels spend the longest time in the interaction region and thus, are expected to become slightly more broadened than the others. Due to these points, we decided to follow the development of the whole 4–peak structure. Integrating each spectrum results in a steplike distribution containing minor structures caused by the single peaks. The energetic "width" ΔE_f (FWHM) and "position" E_f of each 4–peak structure is determined by fitting a Sigmoid function to these steplike distributions. Finally, the space–charge–induced energetic broadening and shift are calculated via $\Delta E_{broad} = \sqrt{(\Delta E_f)^2 - (\Delta E_i)^2}$ and $\Delta E_{shift} = E_f - E_i$, where ΔE_i and E_i are the energetic width and position of the initial test–electron spectrum, respectively.

The dependence of the spectral broadening and the energetic shift on the number of emitted electrons using this procedure is shown in figure 7.6(c). The best fits to the resulting data are given by the linear functions:

$$\Delta E_{broad} = (9.81 \pm 0.11)\ \mu eV \cdot N_C \tag{7.4}$$

$$\Delta E_{shift} = (12.57 \pm 0.02)\ \mu eV \cdot N_C, \tag{7.5}$$

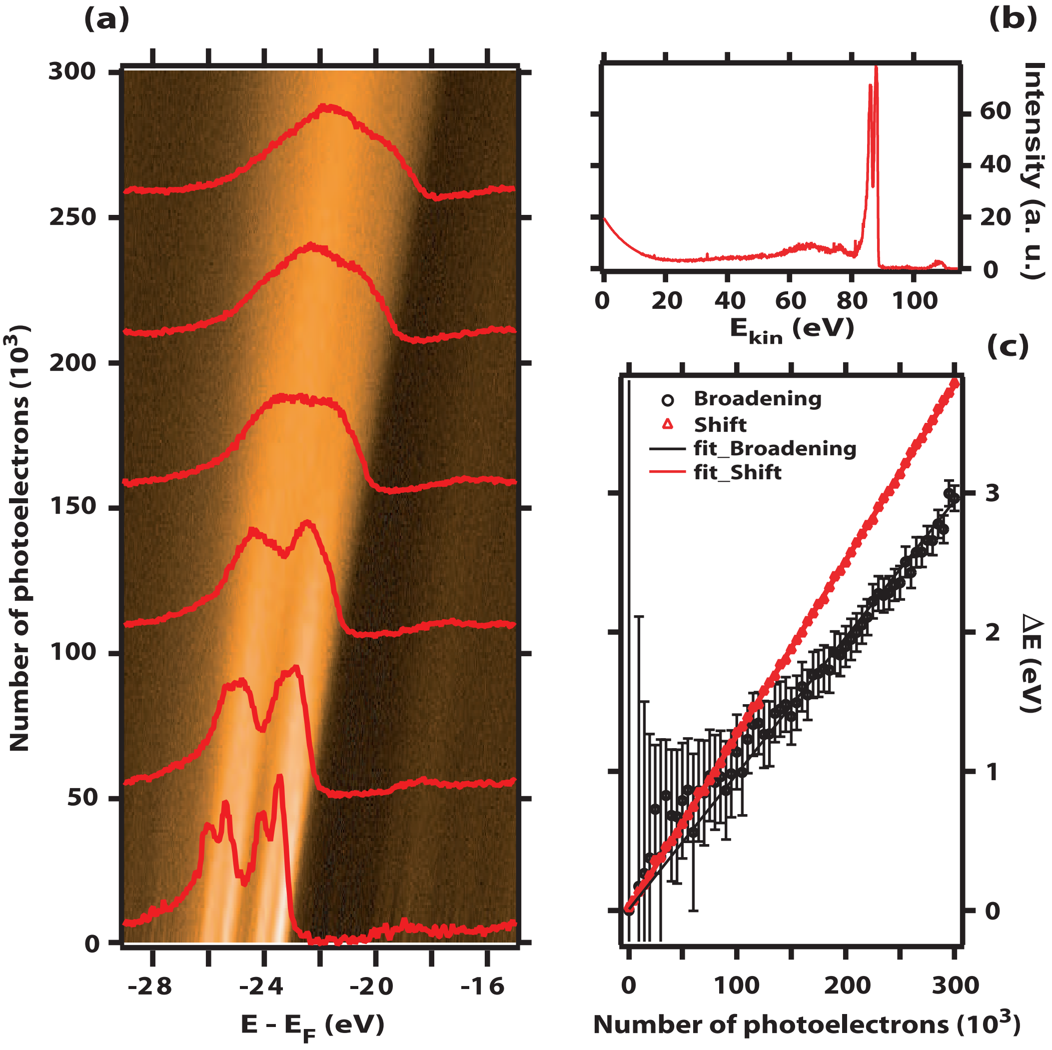

Figure 7.6: (a) Simulated vacuum space–charge effects on a Ta $4f$ core–level spectrum of $1T$–TaS$_2$ as a function of the number of cloud electrons N_C, illustrated in a false color image (white indicates high spectral intensity). The simulation parameters are listed in table 7.1. Additionally, some representative spectra are plotted in red ($N_C = 3.5k, 53k, 107k, 161k, 213k, 259k$). (b) The energy distribution plotted in (b) was used for the cloud electrons. (c) The space–charge induced energy broadening and shift of the initial spectrum show linear behavior: $\Delta\text{E}_{broad} = (9.81 \pm 0.11)\ \mu\text{eV} \cdot \text{N}_C$, $\Delta\text{E}_{shift} = (12.57 \pm 0.02)\ \mu\text{eV} \cdot \text{N}_C$.

consistent with the calculations in [22, 25]. This also confirms earlier results which found a linear behavior of the space–charge–induced broadening and shift as a function of the number of photoelectrons in this kinetic–energy regime.
The main question to answer is now: Do these numerical simulations fit with our experimental data measured at FLASH? For this, we have had to mix the simulated spectra according to their relative amount contributing to the averaged spectrum (see figure 7.5(b)) and compare the result with the appropriate experimental spectrum.
Figure 7.7 serves to establish a better understanding of this procedure. For simplification, four Gaussian–shaped peaks are used instead of the simulated space–charge influenced spectra from figure 7.6(a), approximating the real Ta $4f$ core–level spectrum best. To simulate the space–charge–induced broadening for each number of photoelectrons these peaks are convolved with the space–charge broadening ΔE_{broad} from (7.4) as well as shifted by ΔE_{shift} from (7.5). In figure 7.7 a representative set of photoemission spectra $a_{N_C}(E-E_F)$ for different numbers of electrons ($N_C = 1$, 50000, 100000, 150000, 200000) is depicted. Furthermore, a frequency distribution of these spectra $H_{\langle f_0 \cdot N_C \rangle}$ (blue curve in the middle) belonging to a virtual mixed spectrum of an average number of electrons per pulse ($\langle N_C \rangle = 80000$) (red curve on the right) is plotted. In the experiment, the frequency distributions for every different intensity channel were originally determined by measuring the number of photons per pulse N_{Ph} with the MCP–tool. Assuming a photoemission process, where the number of photoelectrons is proportional to the incident photons, leads to $N_C = \frac{1}{f_0} \cdot N_{Ph}$ ($\langle N_C \rangle = \frac{1}{f_0} \cdot \langle N_{Ph} \rangle$), where $\frac{1}{f_0}$ can be seen as the conversion efficiency (number of emitted photoelectrons per incident photon) for TaS_2 at the given experimental parameters and will serve as the most important fit parameter in the following. In addition to the weighting of the different spectra $a_{N_C}(E-E_F)$ by the frequency distribution $H_{\langle N_{Ph} \rangle} = H_{\langle f_0 \cdot N_C \rangle}$, one has to take into account that at higher pulse intensities more electrons will hit the detector and, therefore, contribute to the measured spectrum. This is considered by additionally multiplying each summand by the appropriate number of electrons per pulse (see fig. 7.7, left column). Finally, the averaged spectrum $A_{\langle N_{Ph} \rangle}(E-E_F)$ is obtained by the following relation:

$$\begin{aligned} A_{\langle N_{Ph} \rangle}(E-E_F) &= A_{\langle f_0 \cdot N_C \rangle}(E-E_F) \\ &= \sum_{N_C} \big(N_C \cdot H_{\langle f_0 \cdot N_C \rangle}(f_0 \cdot N_C) \cdot a_{N_C}(E - E_F + f_1 + f_2 \cdot N_C) \big) \end{aligned} \tag{7.6}$$

The sum is running over each number of electrons per pulse N_C, for which a simulated spectrum a_{N_C} exists. Here, two more fit parameters, f_1 and f_2, are introduced for correcting an over– or underestimation of the energetic shift in the numerical simulations. This over– or underestimation is expected to be linear, because of the linearity of the space–charge effect as a function of the number of electrons [25].
In the simplified example in figure 7.7 one can clearly observe the influence of the mixing of spectra of different pulse intensities. If one compares the profil shape of the mixed spectrum $A_{\langle f_0 \cdot N_C \rangle}$ with $\langle N_C \rangle = 80000$ on the right hand side with the set of simulated spectra on the left side, one would estimate the number of photoelectrons per pulse to be between 100000 and 150000. This is likely to be the major reason for the discrepancy by about a factor of 3 between the experimental results for the space–charge broadening of W $4f$ core–levels at FLASH in [24] and the comparisons of these results with our

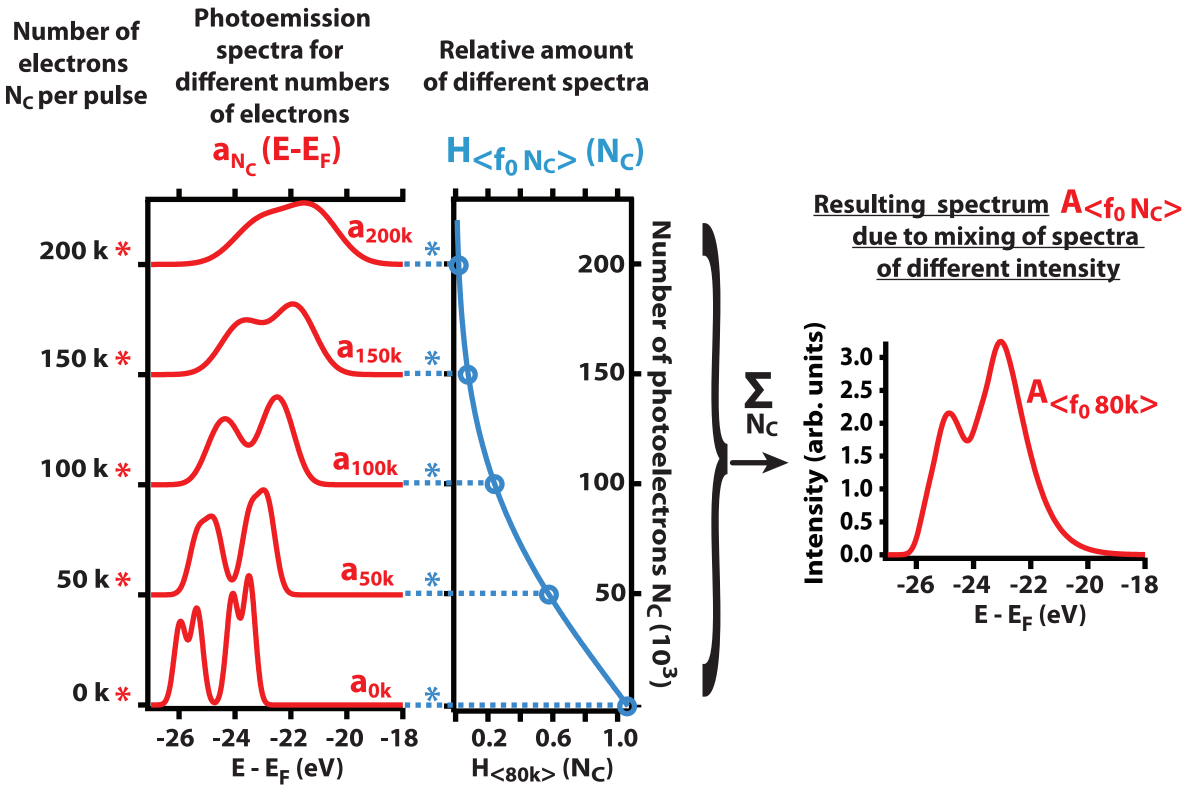

Figure 7.7: Illustration of the procedure of fitting the simulated space–charge influenced spectra (from figure 7.6) to one single experimental one (from figure 7.5), described by relation (7.6). This is necessary due to the mixture of spectra with different intensities using the FEL with strongly fluctuating pulse intensities within one pulse train. The spectrum for an average number of photoelectrons per micro pulse $A_{\langle f_0 \cdot N_C \rangle}$ is determined by summing the simulated spectra a_{N_C} weighted by their relative frequency $H_{\langle f_0 \cdot N_C \rangle}$ (measured with the MCP–tool) and their intensity (given by the number of simulated cloud electrons). The fit parameter stands for the proportion of the FEL pulse intensity N_{Ph} to the number of cloud electrons N_C and serves as the main fit parameter.

simulations in [25].

Now, the ambition was to find constant fit parameters reproducing the experimental spectra sufficiently well. In figure 7.8 the results of fitting the simulated spectra (fig. 7.6(a)) to the experimental data (fig. 7.5(a)) by varying the fit parameters f_0, f_1 and f_2 are shown. Here, the value for f_1 and f_2 were kept constant at zero and for the conversion efficiency a value of $\frac{1}{f_0} = (0.387 \pm 0.376)$ % was determined. The huge inaccuracy again is a consequence due to the pulse–intensity measurement with the MCP–tool. Nevertheless, the mean value of 0.387 % is in good agreement with a conversion efficiency of (0.511 ± 0.1) % obtained by estimations from the atomic subshell photoemission cross sections [151] and the inelastic electron mean free path [153] calculated for TaS_2. Finally, figure 7.8(b) shows the excellent agreement of the fitted simulations and the experimental spectra. With these results, the scales for the number of photoelectrons were added in the graphs in Fig. 7.5.
To conclude, the presented approach of reproducing measured core–level spectra influenced by SCE with simulations with the modified Treecode algorithm will in particular work for metallic surfaces due to the almost immediate neutralization of the photoholes between to subsequent photon pulses. Therefore, PES near the space charge limit or even beyond will be possible in order to detect and study possibly occurring high–field effects in the measured spectra. For ARPES in this intensity regime, the conditions are more complicated due to momentum–dependent band dispersions of the valence and conduction bands and, thus, non–constant electron energy levels. To realize the reproduction of space–charge influenced ARPES spectra by the presented approach, knowing of the experiment specific parameters as well as the generated photoelectron distribution under "normal conditions" (without SCEs) as accurate as possible is essential.

7.6 Summary and conclusion

The microscopic analysis of TMDC crystals after illumination with high–intense and ultra–short FEL radiation shows that, in principle, photoemission experiments at FLASH are feasible using monochromatized and, therefore, moderate pulse intensities without suffering radiation damage. Employing non–monochromatized pulse trains containing 20 pulses with energies of 1 – 10 μJ and pulse durations of some ten fs lead to triangular hole growth at the crystals surface. This is presumably due to successive heating of the surface during a pulse train and field–assisted evaporation.
The valance–band photoemission data of TiTe_2 in the multi pulse mode reveal the general feasibility of measuring the band structure near the Fermi energy with ultra–short FEL pulses in an intensity regime free from space charges. For the interpretation of the PE data at higher intensities the description of SCEs by numerical simulations as practicable and realistic as possible is essential. For this, the used Treecode Algorithm can be an ideal tool. Future measurements with the here developed intensity monitoring tools allow to sort the spectra more precisely with regard to the photon pulse intensities and will help to better understand SCEs in PES.
Until now, only metals have been experimentally and numerically investigated with regard to the influence of space–charges to the spectra, discovering the importance of the mirror–charges contributing to the SCE. For these experiments our simulations have worked very well [25]. Our core–level measurements and the corresponding simulations for the Ta $4f$ core–level spectra of $1T$–TaS_2 in the Mott–insulating CDW phase, presented here, affirm

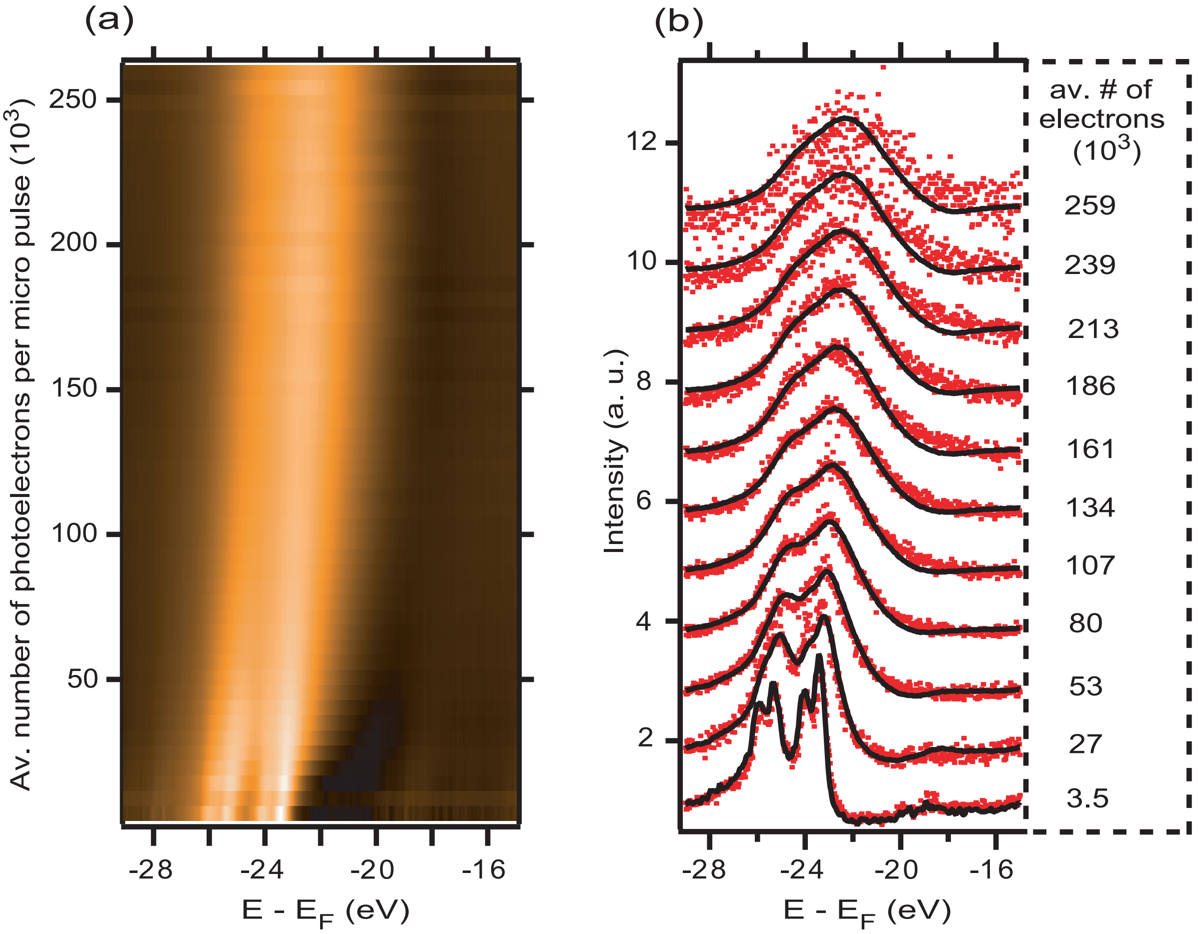

Figure 7.8: Comparison of the simulated space–charge effected spectra from figure 7.6 with the experimentally gained spectra from figure 7.5 by fitting the simulations to the experiment according to formula (7.6). (a) Result of the fit with a fixed ration between the number of photoelectrons in the simulations and the micro pulse intensity ($1/f_0 = 0.387$) given by the MCP–tool. The 2D–intensity histogram from figure 7.5 (b) is used and no additional energy shift per number of photoelectrons has been taken into account ($f_1 = f_2 = 0$). (b) Direct comparison of the fit (solid line) with the experimental spectra (red squares) for some chosen average numbers of electrons $\langle N_C \rangle$.

the validity of our simulations with the Treecode Algorithm even for non–metallic samples without mirror charges.

Altogether, our first experiments at FLASH demonstrate the potential of this light source for core–level as well as valence–band PES. Further taking advantage of the short pulse durations and the nearly total transverse coherence will allow for time–resolved, angle–resolved and/or space–resolved PES in a wide photon energy regime. The adequate description of SCEs by numerical simulations, as done by the modified Treecode Algorithm, and the possibility to deconvolute these contributions in the spectra, may lead to the possibility of even identifying high–field effects in PES in a photon pulse intensity regime, where SCEs are unavoidable, in the near future.

8 Time–resolved PES at FLASH – First Experiments

8.1 Introduction

Angle–resolved as well as core–level PES are powerful methods in order to measure the electronic structure of solids and their surfaces. With the development of laser sources delivering ultra short photon pulses down to the sub–femtosecond regime the investigation of dynamical processes in solids got into the focus of research. Time–resolved pump–probe PES experiments can resolve relaxation processes after photoexcitation of crystals, delivering insight into correlations between the electronic and the phononic system in order to understand physical effects like superconductivity, the formation of CDWs, etc. The main channels for energy relaxations are electron–electron, electron–phonon and phonon–phonon interactions taking place on a femtosecond (1 fs to 100 fs), a picosecond (100 fs to 1 ps) and some ten picosecond timescales (1 ps to 100 ps), respectively.

Typically in the laboratory, time–resolved PES experiments are performed using ultra–short pulsed (some fs) IR laser ($h\nu$ =1.5 eV) sources and generating high harmonic femtosecond EUV pulses from its fundamental wavelength afterwards, e.g., in an argon–filled waveguide. With this setup, photon energies of up to 100 eV are reached, however at the cost of intensity and energy resolution [6–9]. Rohwer *et al.* for example studied the photoexcited, ultrafast breakdown of long–range charge order in the CDW system $1T$-TiSe$_2$ at 125 K using time– and angle–resolved PES and high harmonic femtosecond XUV pulses with a photon energy of 43 eV [5]. However, the limitation of high harmonic radiation sources to photon energies below 100 eV with adequate pulse intensities, discrete multiples of the fundamental photon energy and low intensities can not be overcome at the moment for laboratory sources. In terms of ARPES, high k–values in order to map higher Brillouin zones are not reachable, and in terms of core level PES, only few levels can be reached. Furthermore, to achieve good energy resolution the pulses have to be further monochromatized. This lowers the already low pulse intensity, and makes many experiments impossible to perform.

The FEL in Hamburg is now able to resolve those restrictions in time–resolved ARPES and XPS. FLASH produces very intense ($\approx 10^{13}$ photons per pulse), ultra short (some ten fs) photon pulses in the VUV to EUV regime (wavelength range of the fundamental: 6.5 – 47 nm) with nearly total transverse coherence. The wavelength is continuously tunable, and with the fifth harmonics photon energies of up to 1000 eV are usable for spectroscopy. These parameters make FLASH an ideal candidate for time–resolved PES experiments overcoming the general limitations of laboratory laser sources.

During this thesis, a setup was developed realizing time–resolved PES experiments at FLASH (see chapter 5). The capability of this experimental setup will be shown in terms of time–resolved core level spectroscopy on a first physical example. As introduced in chapter 3.4, $1T$–TaS$_2$ in the Mott–insulating phase shows interesting dynamics of the electronic system after excitation with an intense optical fs–laser [55, 56, 70, 71] (see section 3.4). By now, these dynamics were only studied by time–resolved reflectivity measurements [70, 71] as well as time–resolved PES of the Fermi edge [55, 56]. In the latter, Perfetti *et al.* delivered 6 eV radiation from a higher–harmonic laser source. Taking advantage of the pulse parameters at FLASH and, especially, the higher photon energies, we studied the relaxation dynamics via time–resolved PES of the Ta $4f$ core levels. Pumping the Mott–insulating phase of $1T$–TaS$_2$ with a high intense laser pulse a phase transition into an intermediate metallic phase can be induced. Due to the fact that the CDW–splitting of the Ta 4*f* core levels are directly connected with the CDW amplitude [43] (see chapter 3.4), the dynamics supposed to be found here as well. On the one hand, one would suppose a similar shift of the peaks in the spectrum towards higher kinetic energies. On the other hand, a periodic modulation of the CDW–splitting of the Ta 4*f* levels (Δ_{CDW}) due to coherent phonons ("breathing mode of the star of David" [70, 71]) and the concomitant oscillation of the Ta atoms might be observed.

The results of the first experiment with this new setup will be presented in the following. The general functionality will be shown, occurring problems will be revealed, and solutions for upcoming beamtimes will be given.

8.2 Experimental aspects and strategy of time–resolved PES at FLASH

In order to perform time–resolved core level PES experiments on $1T$–TaS$_2$ the experimental setup as described in chapter 5.3.3 was used at beamline PG2 at FLASH. The IR burstmode laser served as pump source delivering 200 single pulses within one pulse train. The single pulses were separated by 1 μs, and photons with a wavelength of 800 nm ($\approx$ 1.5 eV), a pulse length of 150 fs and a maximum pulse energy of 14 μJ per pulse hit the sample on an area with a diameter of 1.5 mm. This approximately corresponded to the experimental pump parameters in [55, 56]. The FEL produced pulse trains containing 100 pulses separated by 2 μs with a repetition rate of 5 Hz. The fundamental FEL wavelength was set to 7 nm. Monochromatized FEL radiation resulted in a photon energy of 174.4 eV and a pulse elongation to 1.2 ps [100] (first order of the monochromator, c_{ff} value of 1.6, 1200 lines/mm high resolution grating). The overall energy resolution of the PES experiment was $\approx$ 100 meV and the temporal resolution was 1.6 ps due to the FEL pulse elongation, temporal jitter of the FEL, and the temporal resolution of the streak camera. The $1T$–TaS$_2$ sample was cooled down via a manipulator cryostat and liquid Nitrogen in order to reach the Mott–insulating phase below 190 K.

The strategy for performing time–resolved PES at FLASH with the introduced setup contains four main steps including the data analysis afterwards:

- In the first step, the high **pulse intensities of the FEL radiation** ($\approx$ 20 μJ per pulse) are strongly **attenuated** in order to suppress SCEs in the PE spectra. An attenuation of four orders of magnitude was realized via metal filter foils located between monochromator and experimental chamber until no SCEs were visible any longer in the core level spectrum. Fig. 8.1 depicts the Ta 4*f* spectra measured at two different beamtimes, the basic core level spectrum after attenuation (red curve) and the result from the intensity dependent experiments (from chapter 7.5, Fig. 7.5) with lowest pulse intensities (blue curve). The direct comparison of both graphs shows two main points. The SCEs seems to be successfully suppressed in both of them because the low binding energy edges are comparably sharp ($\approx$ 500 meV). Though, the CDW–splitting of the Ta 4*f* levels in our time–resolved experiment is significantly smaller. This is an indication of an insufficient cooling of the sample and, thus, lower CDW amplitude.

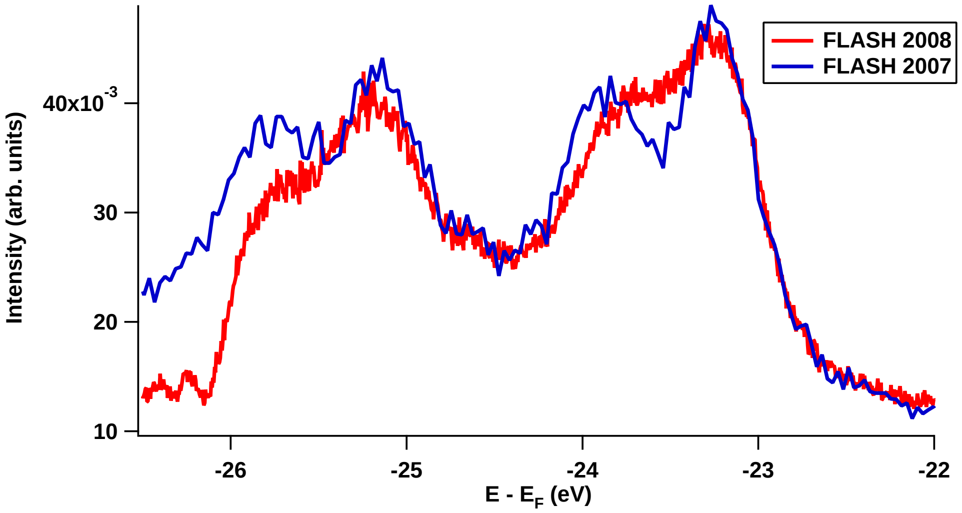

Figure 8.1: Comparison of Ta 4*f* spectra measured at two different beamtimes, the basic core level spectrum after final attenuation for the time–resolved PES experiments (red curve), and the result from the intensity dependent experiments (from chapter 7.5 Fig. 7.5) with lowest pulse intensities (blue curve). In both spectra the SCE's are successfully suppressed. Though, the CDW–splitting of the red curve is significantly smaller.

- The second preparatory step for time–resolved PES experiments lies in the adjustment of the **spatial as well as temporal overlap of the FEL and IR laser pulses** at the sample position. For this, the collinear laser injection and the timing tool as described in chapters 5.2.1 and 5.2.2 were used.
  Fig. 8.2 depicts the result of the reflectivity measurement of the GaAs crystal attached to the timing tool. Here, negative delay means, that the IR probe laser pulse arrived before the FEL pump pulse. The offset of ≈ 0.13 % was mainly due to photo diodes with different rising times and can be neglected. The change in the reflectivity of the GaAs crystal was in the 0.1 % regime, other than in [96], where the reflectivity changes were in the 1 % regime. Furthermore, no drop but an increase in reflectivity was measured contrary to the expectations of [96]. This could be explained by the significantly different photon energy of 174.4 eV against 39.5 eV in [96] used in this setup and, thus, different excitation dynamics. The temporal overlap between IR and FEL laser pulse was defined as the maximum of the second derivation of the Sigmoid function fitted to the data in Fig. 8.2. With the timing tool, the temporal overlap between pump and probe pulses could be determined with an accuracy of approximately 1 ps (see grey box in Fig. 8.2).

- After attenuation of the FEL intensity and identification of the temporal and spatial overlap, the **pump–probe experiment of probing the Ta 4*f* core level as a function of delay** between pump and probe pulse was performed. For this the delay was varied in the interval from -10 ps to 20 ps around the temporal overlap in steps of 200 fs.

- The relevant data, consisting of PE spectra, laser intensities and delay as well machine parameters were stored with the related timestamp via DOOCS. The data

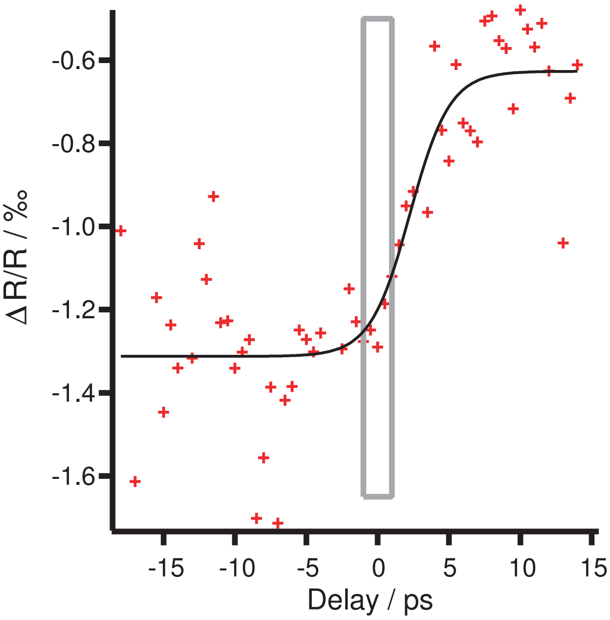

Figure 8.2: Determination of the temporal overlap between pump and probe pulses (from [114]): The graph shows the relative change of the reflectivity of the GaAs crystal as a function of the delay between IR laser and FEL pulses. The black curve depicts a fit with a Sigmoid function to reflectivity data points. The temporal overlap was defined as the maximum of the second derivation of the Sigmoid function. The temporal accuracy of ≈ 1 ps is indicated by the bar around zero delay.

analysis was performed afterwards. For this, a special software was programmed for sorting the data with respect to the FEL pulse intensity (corresponding with events on the CCD image), IR pump laser intensity, and delay measured by the streak camera.

8.3 Results of time–resolved PES of Ta 4*f* core levels of 1*T*–TaS$_2$

The time–resolved PES of the Ta 4*f* core levels was performed in the interval of -10 ps and 20 ps around the temporal overlap in steps of 200 fs. Negative delays indicate that the FEL pulse arrived before the exciting IR laser pulse at the sample surface. The results are summarized in Fig. 8.3. The gray–scale image in Fig. 8.3(a) shows the measured PE intensities as a function of binding energy E-E$_F$ and the temporal delay in steps of 500 fs. Due to insufficient statistics in the single delay channels, further binning was necessary. Thus, each spectrum is averaged over a 5 ps interval, drastically reducing the temporal resolution.

No change in the CDW–splitting of the Ta 4*f* as a function of the delay was found. This can be mainly explained by the intrinsically low splitting due to insufficient cooling of the sample via the cryostat. However, in order to find a possible shift of the spectrum due to the excitation of the electronic system and the proposed phase transition from the Mott insulating into the intermediate metallic state, a Sigmoid function was fit to the low energy edge of the Ta 4*f* core levels (blue box in Fig. 8.3(a)). Its position is plotted as a function of the delay together with the standard deviation in Fig. 8.3(b). In total, a

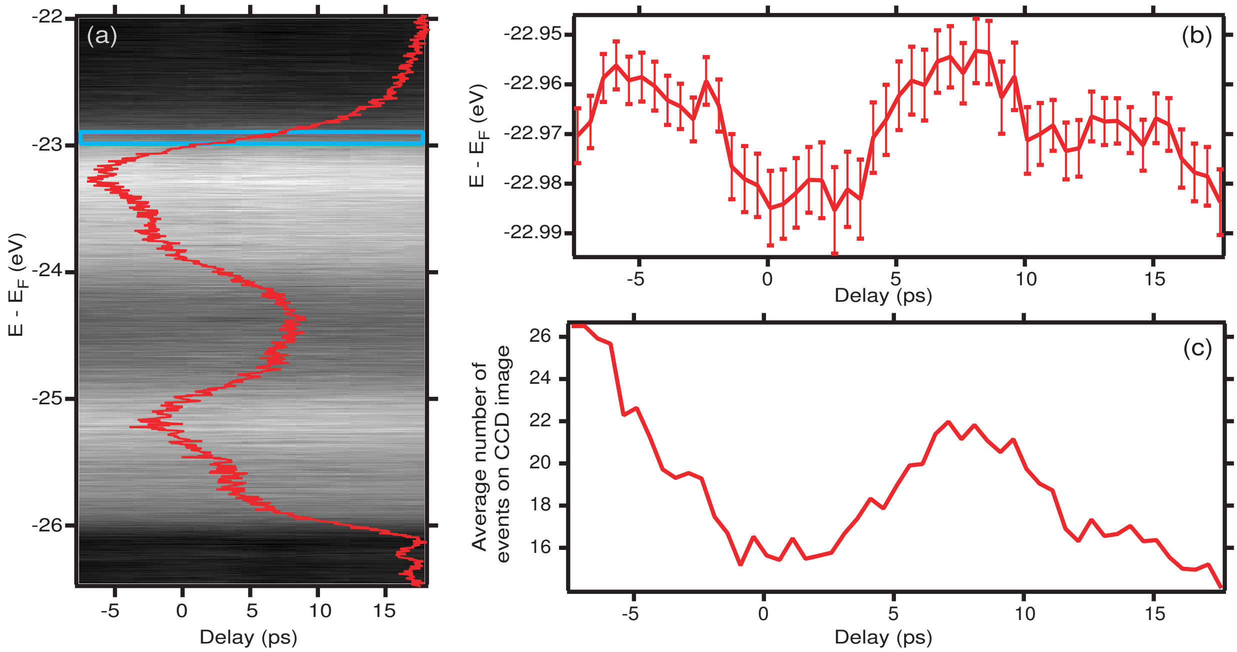

Figure 8.3: Results of the first time–resolved PES experiment of Ta 4*f* core levels on TaS$_2$ as a function of delay between IR excitation pulse (hν=1.5 eV, 150 fs pulse duration, 14 μJ pulse energy) and FEL probe pulse (hν=174.4 eV, 1.2 ps pulse duration). Negative delays mean that the FEL pulse arrived before the IR laser pulse. (a) Gray–scale image of the Ta 4*f* core levels as a function of delay. The blue box indicates the low energy edge of the Ta 4*f* core levels. Its position is plotted as a function of delay in (b) (fitted with a sigmoid function). (c) Average number of events on the CCD detector per photon pulse train contributing to the PE spectra in (a). In order to get better statistics, the time channels were binned up to 5 ps.

maximum variation of the edge position was found to be ≈ 20 meV. At negative delays, the edge position kept almost constant, while at the position of overlapping pump and probe pulse a change of the edge position of about 20 meV towards higher binding energies was observed. In the regime, where the IR pump pulse arrived before the FEL pulse, the coherent phonons observed in [55, 56] was not resolved due to the insufficient temporal resolution. However, a relaxation of the edge position towards the original position was found.

Now, the question is whether this observed effect (the edge shift towards higher binding energies and subsequent relaxation towards initial energetic position in Fig. 8.3(b)) is directly connected with the excitation of the TaS_2 surface, or whether it has a different reason. The graph in Fig. 8.3(c) shows the average number of events on the CCD image per pulse train as a function of the delay between the FEL and IR pulse. This is a rough estimate for the average pulse intensities of the FEL. With such an intensity–fluctuating photon source as the FEL, it can not be excluded that the observed shift is caused by SCEs. And indeed, the curve in Fig. 8.3 (c) shows a similar - though not identical - trend like the edge position of the Ta $4f$ peak in Fig. 8.3 (b). Thus the observed, apparently time–dependent SCE–induced spectral shift seems to interfere with the possibly existent physical effects.

However, the same time–resolved core level PES experiment was carried out by our group using the same experimental setup during a later beamtime [4]. With the experience from the presented first beamtime, improvements were done in terms of temporal resolution (≈ 700 fs) and attenuation of the FEL intensities (no more SCEs due to FEL). This time, a drop in the CDW–splitting of the Ta $4f$ could be observed from an original value of 0.62 eV to 0.47 eV and a recovery to a quasi–equilibrium value (dependent on the excitation energy of the pump laser) with a time constant of ≈ 900 fs.

Again, the optical pump laser was used with a photon energy of 1.55 eV. Two different excitation fluences were used: $F_1 = 1.8$ mJ/cm^2 and $F_2 = 2.5$ mJ/cm^2 corresponding to absorbed energy density of approximately 120 meV per Ta atom and 165 meV per Ta atom, respectively. Both energies are larger than the required energy to heat the the sample above the CCDW–NCCDW temperature of ≈ 110 meV. Figure 8.4 summarizes the results of this beamtime. In Fig. 8.4(a) the measured time–resolved ta $4f$ photoemission spectra are shown in the false–color immage. The experimental temporal resolution was determined to be ≈ 700 fs via analyzing the photoemission intensity in the regime were side bands of the c peak of the Ta $4f_{1/2}$ were expected, generated by the absorption of optical laser photons during the ionization process. In Figure 8.4(c) the behavior of the CDW splitting Δ_{CDW} of the Ta $4f$ core levels is plotted as a function of pump–probe delay. This time, a strong influence of the optical pump laser on Δ_{CDW} is found: As expected, Δ_{CDW} decreases on a subpicosecond time scale, followed by a partial recovery with a time constant of ≈ 900 fs and relaxation into a quasiequilibrium state with time scale of more than 10 ps. Fig. 8.4(d) shows the development of the electron temperature during the excitation process calculated by a two temperature model [4]. The electron temperature strongly exceeded the equilibrium CCDW–NCDW transition temperature on a subpicosecond time scale leading the nearly immediate drop in Δ_{CDW}, followed by a drop to the transition temperature due to electron–phonon coupling and the energy transfer to the lattice. This anticorralation between the electron temperature and Δ_{CDW} indicates that the charge–order parameter in the CDW system $1T$–TaS_2 is mainly bound on the electron temperature.

To conclude, in this experiment the direct measurement of charge–order dynamics in a complex material with femtosecond resolution and atomic–site sensitivity was realized for the first time. This encourages to further improve the available setup in order to get novel insights into the noneqilibrium behavior of strongly correlated materials or even into the dynamics of chemical reactions on solid surfaces.

8.4 Conclusion and outlook

Our first experiments with this new setup for time–resolved PES showed its general functionality. Furthermore, with the presented setup, in [4] the direct measurement of charge–order dynamics in the complex material $1T$–TaS$_2$ with femtosecond resolution and atomic–site sensitivity was realized for the first time. Even though the temporal resolution was not high enough to resolve the coherent phonons described in the literature [55, 56, 70, 71], this encourages to further improve the available setup in order to get novel insights into the noneqilibrium behavior of strongly correlated materials.

However, a few challenges have to be met and some problems have to be solved before time–resolved PES at FLASH will be competitive to experiments with fs–laser sources, especially in terms of temporal resolution as well as constant pulse intensities.

A nominal temporal resolution of 1.6 ps due to pulse elongation within the monochromator, temporal jitter of the FEL, and temporal resolution of the streak camera is far too bad in order to resolve the proposed dynamics of the Ta $4f$ core levels. This temporal resolution was further decreased by binning of time channels to a total length of 5 ps due to insufficient statistics within the original 200 fs delay intervals. In future experiments, the nominal temporal resolution can be significantly increased by using the EOS instead of the streak camera for determining the delay between pump and probe with a temporal resolution of $\approx$ 100 fs. Together with the usage of the 200 lines/mm–grating of the PG2 beamline (resulting in a reduced pulse elongation at the expense of energy resolution) a total nominal temporal resolution of better than 300 fs is likely to be achieved.

The pulse–to–pulse intensity fluctuations at FLASH may play a role in the observed energetic shift of the edge position in Fig. 8.3(b). The histogram in Fig. 8.5 makes this even more obvious. Here, for each time channel the relative amount of different pulse train intensities (represented by the number of events in the CCD image) is shown (gray–scale image), as well as the associated average pulse train intensities (red crosses). Additionally, as described in section 7.5, every CCD image in the multi pulse mode contains of mixture of PE spectra generated by single photon pulses with varying pulse intensities.

There are two possible methods to overcome this problem with pulse fluctuations:

On the one hand, "seeding" of the FEL (see section 4.1) with a fundamental wavelength will deliver maximum amplification of only this mode. Therefore, photon energy fluctuations in front of the monochromator are excluded as well as the resulting pulse intensity fluctuations. This technique is planned at FLASH for wavelengths from 13 – 30 nm. Hence, this will not be the method of choice for our time–resolved core level PES experiments because of the restricted photon energy.

On the other hand, modern time–of–flight (ToF) photoelectron spectrometers are able to resolve the PE signals of each single pulse within one pulse train. This ToF spectrometer consists of a flight tube with integrated electron optics imaging the photoelectrons on a two–dimensional delay–line detector in the exit plane. The temporal resolution of this

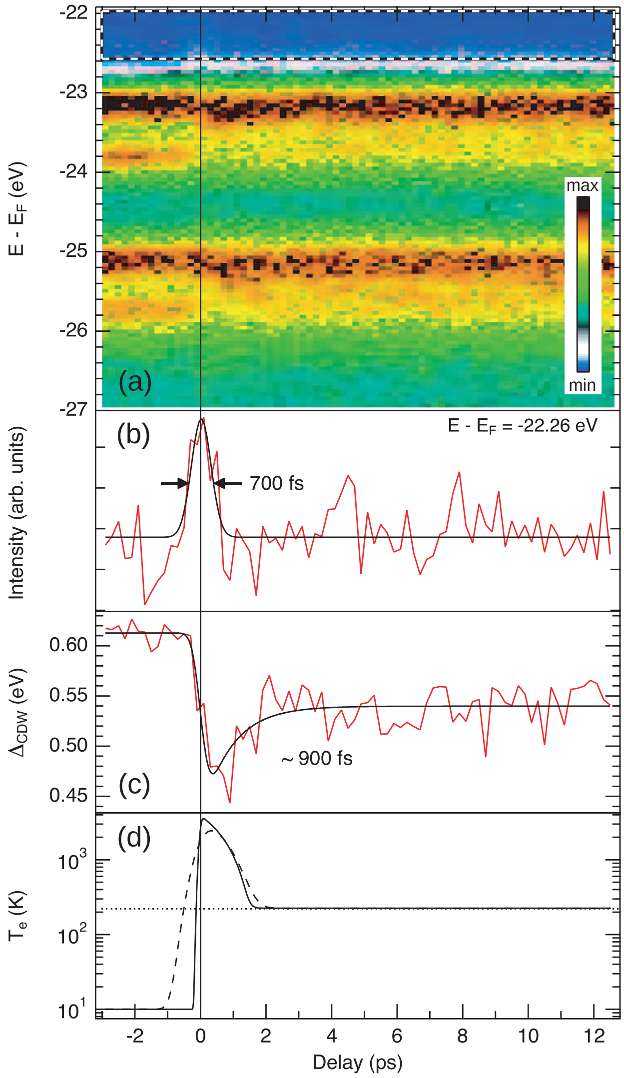

Figure 8.4: Charge–order dynamics in $1T$–TaS$_2$ (from Ref. [4]): (a) False–color image illustrates the measured time–resolved Ta $4f$ photoemission spectra of $1T$–TaS$_2$ as a function of the dely between optical pump (hν =1.55 eV, F = 1.8 mJ/cm^2) and FEL probe (hν =156 eV) pulse. Within the dashed box first–order sideband intensity of the c peak of the Ta $4f_{7/2}$ level (see Fig. 3.4(c)) is measured. (b) Integrated photoemission intensity over the energy interval marked in (a). The red curve shows the cross correlation between pump and probe pulse generated by the laser–assisted photoelectric effect. These data are fit by a Gaussian in order to determine the temporal resolution of the experiment. (c) The induced change of the CDW splitting Δ_{CDW} of the Ta $4f$ core levels as a function of pump–probe delay obtained by line shape fitting. The black curve represents an exponential fit to the red curve starting at zero delay convoluted with a Gaussian due to the effective temporal resolution. (d) Electron temperature calculated from a two–temperature model as a function of temporal delay (solid curve). The dashed curve depicts the convolution with the Gaussian determined by the temporal resolution in (b). The dotted line indicates the transition temperature between CCDW and NCCDW phase.

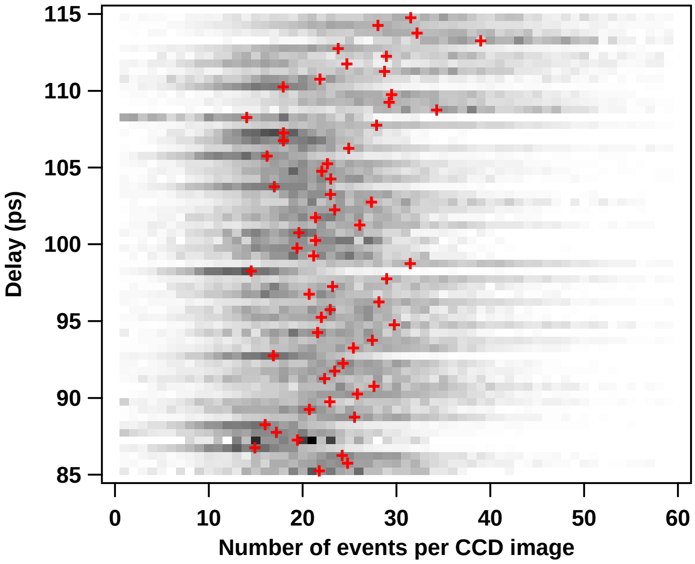

Figure 8.5: Gray–scale image of the relative amount of different pulse train intensities (represented by the number of events in the CCD image), as well as the associated average pulse train intensities (red crosses) as a function of the delay between pump and probe laser. The intensity fluctuations of the FEL are clearly visible.

system is good enough to separate the electron signals from every single pulse. With this system, the intensity fluctuations of the FEL are not suppressed, but together with an accurate photon pulse intensity measurement of every single pulse (see subsection 5.1.2 and 5.1.3) a more efficient sorting of the PE data will be possible and the PE spectra for every delay channel in our time–resolved PES experiments will be comparable. Furthermore, ToF photoelectron spectrometers are able to measure the electron emission angle in parallel, making this spectrometer type an ideal instrument for time–resolved ARPES at FLASH. Our group intensively follows this possibility and will integrate a ToF spectrometer in the experimental setup for future PE measurements at FLASH.

9 Conclusions and perspectives

The free–electron laser (FEL) in Hamburg (FLASH) [10–12] with its outstanding characteristics in terms of photon pulse intensities (up to 100 μJ/pulse), reachable photon energy range (30 eV to 1500 eV), transverse coherence as well as pulse durations (some ten femtoseconds) is a very interesting light source to perform photoelectron spectroscopy (PES) experiments with. However, before this photon source could be used for different PES experiments, i.e. angle–resolved (ARPES), core–level (XPS) and time–resolved (TRPES) photoelectron spectroscopy, the FEL parameters considerably differing from other photon sources have to be controlled via a new experimental setup. In this thesis, different experimental setups were built up in order to realize ARPES, XPS and TRPES experiments at the plane grating monochromator beamline PG2 at the FEL in Hamburg (FLASH) and the "proof of principle" of these experiments at FLASH is presented. Existing as well as newly developed systems for online monitoring of FEL pulse intensities and generating spatial and temporal overlap of FEL and optical laser pulses for time–resolved experiments are successfully integrated into the experimental setups for PES. The main parts of this thesis were the following:

- The existing MCP detector for online intensity monitoring is originally calibrated for photon energies of 38.5 eV. A conversion relation in order to calculate the number of photons per pulse for the photon energy range from 38.5 to 120 eV is determined in this thesis. So, this monitoring system can be used for a wider energy range, though, the relative error exceeds 50 % even at the calibrated photon energy of 38.5 eV mainly due to the inaccuracy in the beamline transmission of PG2.

- For the investigation and particularly the understanding of space–charge effects (SCEs) in PES, the knowledge of exact photon pulse intensity is essential. Therefore, an own intensity monitoring system was developed, built and tested during this thesis, the I–tube. With this a more precise intensity calibration for the currently used photon energy directly before performing the experiment is possible in future experiments, no inaccurate conversion relation is needed, and it is applicable for a wider photon energy range.

- A system for collinear injection of an optical and pulsed laser into the FEL beam was developed and built up for time–resolved experiments. Together with the "timing tool" developed by the research group of Wurth *et al.*, this setup was successfully operated in time–resolved experiments at FLASH.

In order to understand SCEs in PES and, therefore, being able to handle those effects in future experiments with highly intense and pulsed photon sources, the origin of energetic broadenings and shifts in photoelectron spectra are studied by means of a molecular dynamic N–body simulation using a modified Treecode Algorithm [26] for sufficiently fast and accurate calculations:

- The variation of various PES relevant parameters such as the number of emitted electrons, photon pulse duration, spotsize, kinetic energy distribution, etc. showed that the magnitude of SCEs is mainly dependent on the electron density in phase space. Here, the most influencing parameter is the linear electron density, defined as the ratio between the electron number and the spot diameter. Less influencing are the pulse duration – as long as shorter than 100 ps – and the kinetic energy distribution.

- The parameters of three chosen PES experiments from the literature using completely different photon sources (modern synchrotron radiation source, ultra fast higher harmonic laser source and FEL) and studying space–charge induced energetic broadenings and shifts of pronounced features in the PE spectra as a function of emitted electrons were taken for simulations with the modified Treecode Algorithm. The simulation results reproduced the experimental results fairly well. Appearing discrepancies could be attributed to uncertainties in the underlying experimental parameters.

- In a more general analysis, the focus was laid on simulating the influence of the linear electron density on spectral features in typical core–level as well as valence band spectroscopy experiments. The results are compared with two analytical models from the literature. The model of Long *et al.* proposing a linear dependence of spectral broadening effects as a function of the electron number proved to be accurate, while the mean–field model of Siwick *et al.* resulting in a square root dependency from the linear electron density could only match the simulations for low kinetic energies below 1 eV.

- Finally, some rules of thumb for XPS and ARPES measurements are deduced from the simulations:

    1. For XPS experiments and a desired energy resolution of better than 50 meV, the linear electron density generated at the sample surfaces may not exceed 10000 electrons/mm.
    2. To achieve a better energy resolution of 5 meV in ARPES experiments, the limit of linear electron density lies at approximately 3000 electrons/mm.
    3. The space charge induced momentum broadening is less critical and can be compensated by using higher photon energies due to a $\sqrt{E_{kin}}$–dependency. However, to achieve a momentum resolution of better than 0.01 $\mathring{A}^{-1}$, less than 10000 electrons/$\sqrt{E_{kin}}$ have to be emitted.

Experimentally, SCEs are investigated by means of ARPES as well as XPS measurements as a function of FEL pulse intensities and the question of radiation damages to the solid surface is answered in this thesis:

- Exposed to highly intense photon pulses (zero order FEL radiation with up to 10 μJ pulse energy) and using pulse trains containing 20 single pulses separated by 1 μs, the surface of the transition metal dichalcogenide $1T$–TiTe$_2$ showed triangular structures oriented with regard to the crystal structure. For the generation of these triangular structures, two possible mechanisms are discussed. On the one hand, field–assisted evaporation supported by successive heating of the surface during the pulse trains, and on the other hand, superheating by single, very intense photon pulses followed by transient melting and recrystallization are candidates for this mechanism. However, monochromatized and strongly attenuated FEL intensities, anyway necessary for a good energy resolution and to significantly suppress SCEs, result in unmodified surfaces.

- Intensity dependent ARPES measurements with ultra short ($\Delta \approx 100$ fs) photon pulses were performed and showed that ARPES at FLASH is in principle feasible below the SCE limit. With increasing photoelectron densities, increasing energetic shifts and broadenings in the range of several eV have been observed. For performing ARPES near or even above the SCE limit a better description and understanding of those effects is essential.

- The XPS measurements on the Ta4*f* core levels of $1T$–TaS$_2$ in the CDW–insulating phase were performed as a function of photon pulse intensity with pulse trains containing 20 single pulses. Pulse–to–pulse intensity fluctuations were dominant – even within each pulse train – and the resulting spectra sorted with respect to average pulse energies consisted of a mixture of single spectra with different intensities. Though, a specially developed fit routine could reproduce those mixed spectra quite accurately out of SCE simulations with the newly developed simulation algorithm. This excellent description of the experimental results may lead to the possibility of performing PES even beyond the SCE limit and, therefore, identifying occurring high–field effects in PES experiments using highly intense radiation sources in the near future.

- The space–charge induced energy broadening and shift of the initial spectrum showed a linear behavior as a function of the electron number N_C: $\Delta\mathrm{E}_{broad} = (9.81 \pm 0.11)$ $\mu\mathrm{eV} \cdot \mathrm{N}_C$, $\Delta\mathrm{E}_{shift} = (12.57 \pm 0.02)$ $\mu\mathrm{eV} \cdot \mathrm{N}_C$.

In this thesis, the results of first time–resolved XPS measurements on the Ta4*f* core levels of $1T$–TaS$_2$ in the CDW–insulating phase using a – in comparison with HHG sources – high photon energy of ≈ 175 eV are presented:

- The first test of the experimental setup for time–resolved XPS showed its general functionality. Though, the temporal resolution of 1.6 ps was not competitive with HHG sources.

- A time–dependent evolution of the low binding energy edge of the Ta4*f* core levels was observed. This effect could almost certainly be attributed to varying FEL intensities and, therefore, induced SCEs interfere with possibly existing physical effects.

However, with the same setup, our research group repeated the experiment with significantly better temporal resolution and could directly measure the charge order dynamics in the complex material $1T$–TaS$_2$ with a temporal resolution of 700 fs and atomic–site sensitivity for the first time [4].

To conclude, the results of this thesis strongly encourage to further improve the possibility to perform PES experiments at FLASH. Further improvements of the FEL with regard to stable photon pulse intensities as well as an increase in the number of pulses per second will help to establish ARPES and XPS experiments and, particularly, time–resolved PES experiment below the SCE limit. The integration of modern time–of–flight analyzers will further increases the temporal resolution due to the detection of every single pulse and accurate determination of the delay between optical pump and FEL probe pulse via the electro–optical sampling system with a temporal resolution of 100 fs.
The occurring SCEs effects are well described by the developed SCE simulation algorithm. Therefore, PES experiments even beyond the SCE limit will be possible in order to detect and study possibly occurring high–field effects in the measured spectra. For this, the experimental parameters have to be known as accurate as possible. This can be achieved

by performing reference measurements at conventional synchrotron radiation sources, predicting SCE in the spectra using FEL parameters and the newly developed simulation algorithm and compare the measured SC influenced spectra with the simulated ones.

Finally, the highly intense and coherent FEL radiation can be used for focusing the radiation via diffraction optics such as reflective photon sieve [20, 21] or Fresnel zone plates [19] to a nanometer scale in order to combine good spatial (10 nm), momentum (0.01 $\AA^{-1}$), energy (1 meV) and temporal (100 fs) resolution in one experiment.

With the usage of FEL radiation – and later with the X–ray FEL in Hamburg delivering photon pulses with wavelengths down to 0.1 nm – ultra–fast (some ten fs) dynamical processes on the atomic length scale will be able to be investigated element specifically. These are for example dynamics of chemical reactions on surfaces such as cathalytical processes, charge order dynamics in correlated materials, spin dynamics in magnetic materials or systems interesting for spin–electronics, and a lot more.

References

[1] S. Hüfner, in *Photoelectron Spectroscopy: Principles and Applications* (Springer, Berlin, 2003).

[2] J. P. Callen, Ph.D. thesis, The Department of Physics (Harvard University), 2000.

[3] M. Lisowski, P. A. Loukakos, A. Melnikov, I. Radu, L. Ungureanu, M. Wolf, U. Bovensiepen, Phys Rev Lett. **95**, 137402 (2005).

[4] S. Hellmann, M. Beye, C. Sohrt, T. Rohwer, F. Sorgenfrei, H. Redlin, M. Kalläne, M. Marczynski-Bühlow, F. Hennies, M. Bauer, A. Föhlisch, L. Kipp, W. Wurth, K. Rossnagel, Phys. Rev. Lett. **105**, 187401 (2010).

[5] T. Rohwer, S. Hellmann, M. Wiesenmayer, C. Sohrt, A. Stange, B. Slomski, A. Carr, Y. Liu, L. M. Avila, M. Kalläne, S. Mathias, L. Kipp, K. Rossnagel, M. Bauer, Nature **471**, 490 (2011).

[6] A. L'Huillier, P. Balcou, Phys. Rev. Lett. **70**, 774 (1993).

[7] J. J. Macklin, J. D. Kmetec, C. L. Gordon, Phys. Rev. Lett. **70**, 766 (1993).

[8] Ch. Spielmann, N. H. Burnett, S. Sartania, R. Koppitsch, M. Schnürer, C. Kan, M. Lenzner, P. Wobrauschek, F. Krausz, Science **278**, 661 (1997).

[9] A. Rundquist, Ch. G. Durfee III, Z. Chang, C. Herne, S. Backus, M. M. Murnane, H. C. Kapteyn, Science **280**, 1412 (1998).

[10] E.L. Saldin, E.A. Schneidmiller, M.V. Yurkov, Nucl. Instrum. Methods Phys. Res., Sect. A **562**, 472 (2006).

[11] W. Ackermann et al., Nature Photonics **1**, 336 (2007).

[12] http://flash.desy.de.

[13] A. Barty et al., Nature Photonics **2**, 415 (2008).

[14] H. N. Chapman et al., Nature Physics **2**, 839 (2006).

[15] A.R.B. de Castro, C. Bostedt, E. Eremina, M. Hoener, H. Thomas, T. Laarmann, T. Fennel, K.H. Meiwes–Broer, E. Plönjes, M. Kuhlmann, H. Wabnitz, T. Möller, J. Electron Spectrosc. Relat. Phenom. **156–158**, 25 (2007).

[16] N. Stojanovic et al., Appl. Phys. Lett. **89**, 241909 (2006).

[17] A.A.Sorokin, S.V.Bobashev, K.Tiedtke, M.Richter, J. Phys. B: At. Mol. Opt. Phys. **39**, (2006).

[18] A. A. Sorokin, S.V. Bobashev, T. Feigl, K. Tiedtke, H. Wabnitz, M. Richter, Phys. Rev. Lett. **99**, 213002 (2007).

[19] W. Chao, B. D. Harteneck, J. A. Liddle, E. H. Anderson, D. T. Attwood, Nature **435**, 1210 (2005).

[20] L. Kipp, M. Skibowski, R. L. Johnson, R. Berndt, R. Adelung, S. Harm, R. Seemann, Nature **414**, 184 (2001).

[21] M. Kalläne, J. Buck, S. Harm, R. Seemann, K. Rossnagel, L. Kipp, Opt. Lett. **36**, 2405 (2011).

[22] X.J. Zhou, B. Wannberg, W.L. Yang, V. Brouet, Z. Sun, J.F. Douglas, D. Dessau, Z. Hussain, Z.–X. Shen, J. Electron Spectrosc. Relat. Phenom. **142**, 27 (2005).

[23] S. Passlack, S. Mathias, O. Andreyev, D. Mittnacht, M. Aeschlimann, M. Bauer, J. Appl. Phys. **100**, 024912 (2005).

[24] A. Pietzsch, A. Föhlisch, M. Beye, M. Deppe, F. Hennies, M. Nagasono, E. Suljoti, W. Wurth, C. Gahl, K. Döbrich, A. Melnikov, New Journal of Physics **10**, 33004 (2008).

[25] S. Hellmann, K. Rossnagel, M. Marczynski–Bühlow, L. Kipp, Phys. Rev. B **79**, 035402 (2009).

[26] J. Barnes, P. Hut, Nature **324**, 446 (1986).

[27] M. Kalläne, Ph.D. thesis, Institut für Experimentelle und Angewandte Physik (Universität Kiel), 2007.

[28] H. Hertz, Ann. Phys. **31**, 983 (1887).

[29] W. Hallwachs, Ann. Phys. **31**, 301 (1888).

[30] A. Einstein, Ann. Phys. **17**, 132 (1905).

[31] M. Grass, J. Braun, G. Borstel, Phys. Rev. B **47**, 15487 (1992).

[32] W. E. Spicer, Phys. Rev. **112**, 114 (1958).

[33] C. N. Berglund, W. E. Spicer, Phys. Rev. A **136(4)**, 1030 (1964).

[34] M. P. Seah, W. A. Dench, Surface and Interface Analysis **1**, 2 (1979).

[35] C. Sohrt, Diploma thesis, Institut für Experimentelle und Angewandte Physik (Universität Kiel), 2009.

[36] J. Iwicki, Ph.D. thesis, Institut für Experimentelle und Angewandte Physik (Universität Kiel), 2009.

[37] N. Martensson, P. Baltzer, P. A. Brühwiler, J.-O. Forsell, A. Nilsson, A. Stenborg, B. Wannberg, J. Electron Spectrosc. Relat. Phenom. **70**, 117 (1994).

[38] T. Kiss, T. Shimojima, K. Ishizaka, A. Chainani, T. Togashi, T. Kanai, X.-Y. Wang, C.-T. Chen, S. Watanabe, S. Shin, Rev. Sci. Instrum. **79**, 23106 (2008).

[39] T. Riedel, private communication.

[40] http://vgscienta.com.

[41] J. A. Wilson, A. D. Yoffe, Advances in Physics **18**, 193 (1969).

[42] J. A. Wilson, F. J. Di Salvo, S. Mahajan, Advances in Physics **24**, 117 (1974).

[43] H. P. Hughes, R. Pollak, Philos. Mag. **34**, 1025 (1976).

[44] P. Fazekas, E. Tosatti, Philos. Mag. B **39**, 229 (1979).

[45] R. Brouwer, F. Jellinek, Physica B **99**, 51 (1980).

[46] R. A. Pollak, D. E. Eastman, F. J. Himpsel, P. Heimann, B. Reihl, Phys. Rev. B **24**, 7435 (1981).

[47] S. C. Bayliss, A. M. Ghorayeb, D. R. P. Guy, J. Phys. C **17**, (1984).

[48] N. V. Smith, S. D. Kevan, F. J. DiSalvo, J. Phys. C **18**, 3175 (1985).

[49] B. Giambattista, C. G. Slough, W. W. McNairy, R. V. Coleman, Phys. Rev. B **41**, 10082 (1990).

[50] B. Burk, R. E. Thomson, J. Clarke, A. Zettl, Science **257**, 362 (1992).

[51] J.J. Kim, W. Yamaguchi, T. Hasegawa, K. Kitazawa, Phys. Rev. Lett. **73**, 2103 (1994).

[52] K. Rossnagel, N. V. Smith, Phys. Rev. B **73**, 073106 (2006).

[53] K. Rossnagel, J. Phys.: Condens. Matter **23**, 213001 (2011).

[54] K. Rossnagel, E. Rotenberg, H. Koh, N.V. Smith, L. Kipp, Phys. Rev. Lett. **95**, 126403 (2005).

[55] L. Perfetti, P. A. Loukakos, M. Lisowski, U. Bovensiepen, H. Berger, S. Biermann, P. S. Cornaglia, A. Georges, M. Wolf, Phys. Rev. Lett. **97**, 67402 (2006).

[56] L. Perfetti, P. A. Loukakos, M. Lisowski, U. Bovensiepen, M. Wolf, H. Berger, S. Biermann, A. Georges, New Journal of Physics **10**, 53019 (2008).

[57] K. Rossnagel, N. V. Smith, New J. Phys. **12**, 125018 (2010).

[58] A. S. Woedtke, Ph.D. thesis, Institut für Experimentelle und Angewandte Physik (Universität Kiel), 2002.

[59] K. Rossnagel, Ph.D. thesis, Institut für Experimentelle und Angewandte Physik (Universität Kiel), 2001.

[60] D. K. G. de Boer, C. F. van Bruggen, G. W. Bus, R. Coehoorn, C. Haas, G. A. Sawatzky, H. W. Myron, D. Norman, H. Padmore, Phys. Rev. B **29**, 6797 (1984).

[61] R. Claessen, R. O. Anderson, J. W. Allen, W. P. Ellis, S. Harm, M. Kalning, R Manzke, M. Skibowski, Phys. Rev. Lett. **69**, 808 (1992).

[62] J. W. Allen, G. H. Gweon, R. Claessen, K. Matho, J. Phys. Chem. Solids **56**, 1849 (1995).

[63] R. Claessen, R. O. Anderson, G.–H. Gweon, J. W. Allen, W. P. Ellis, C. Janowitz, C. G. Olson, Z. X. Shen, V. Eyert, M. Skibowski, K. Friemelt, E. Bucher, S. Hüfner, Phys. Rev. B **54**, 2453 (1996).

[64] L. Perfetti, C. Rojas, A. Reginelli, L. Gavioli , H. Berger, G. Margaritondo, M. Grioni, R. Gaál, L. Forró, F. Rullier Albenque, Phys. Rev. B **64**, 115102 (2001).

[65] K. Rossnagel, L. Kipp, M. Skibowski, C. Solterbeck, T. Strasser, W. Schattke, D. Voss, P. Krüger, A. Mazur, J. Pollmann, Phys. Rev. B **63**, 125104 (2001).

[66] V. N. Strocov, E. E. Krasovskii, W. Schattke, N. Barrett, H. Berger, D. Schrupp, R. Claessen, Phys. Rev. B **74**, 195125 (2006).

[67] B. Sipos, A. F. Kusmartseva, A. Akrap, H. Berger, L. Forro, E. Tutis, Nature Materials **7**, 960 (2008).

[68] H. P. Hughes, J. A. Scarfe, Phys. Rev. Lett. **74**, 3069 (1995).

[69] R. Inada, Y. Onuki, S. Tanuma, J. Phys. Soc. Jpn. **52**, 3536 (1983).

[70] J. Demsar, L. Forró, H. Berger, D. Mihailovic, Phys. Rev. B **66**, 41101 (2002).

[71] Y. Toda, K. Tateishi, S. Tanda, Phys. Rev. B **70**, 33106 (2004).

[72] S. I. Anisimov, B. L. Kapeliovich, T. L. Perelman, Soviet Physics–JETP **39**, 375 (1974).

[73] G. Brown, K. Halback, J. Harris, H. Winick, Nucl. Instrum. Meth. **208**, 65 (1983).

[74] L. H. Yu, M. Babzien, I. Ben–Zvi, L. F. DiMauro, A. Doyuran, W. Graves, E. Johnson, S. Krinsky, R. Malone, I. Pogorelsky, J. Skaritka, G. Rakowsky, L. Solomon, X. J. Wang, M. Woodle, V. Yakimenko, S. G. Biedron, J. N. Galayda, E. Gluskin, J. Jagger, V. Sajaev, I. Vasserman, Science **289**, 932 (2000).

[75] L. H. Yu, L. DiMauro, A. Doyuran, W. S. Graves, E. D. Johnson, R. Heese, S. Krinsky, H. Loos, J. B. Murphy, G. Rakowsky, J. Rose, T. Shaftan, B. Sheehy, J. Skaritka, X. J.Wang, and Z.Wu, Phys. Rev. Lett. **91**, 074801 (2003).

[76] L. DiMauro, A. Doyuran, W. Graves, R. Heese, E.D. Johnson, S. Krinsky, H. Loos, J.B. Murphy, G. Rakowsky, J. Rose, T. Shaftan, B. Sheehy, J. Skaritka, X.J. Wang, L.H. Yu, Nucl. Instr. and Meth. A **507**, 15 (2003).

[77] D. Garzella, T. Hara, B. Carré, P. Salières, T. Shintake, H. Kitamura, M.E. Couprie, Nucl. Instr. and Meth. A **582**, 502 (2004).

[78] M. Wellhöfer, Ph.D. thesis, Institut für Experimentalphysik (Universität Hamburg), 2007.

[79] M. Wellhöfer, M. Martins, W. Wurth, M. Braune, J. Viefhaus, K. Tiedtke, M. Richter, J. Opt. A: Pure Appl. Opt. **9**, 1 (2007).

[80] A. Azima, S. Düsterer, P. Radcliffe, H. Redlin, N. Stojanovic, W. Li, H. Schlarb, J. Feldhaus, D. Cubaynes, M. Meyer, J. Dardis, P. Hayden, P. Hough, V. Richardson, E. T. Kennedy, J. T. Costello, Appl. Phys. Lett. **94**, 144102 (2009).

[81] H. N. Chapman et al., Nature **448**, 676 (2007).

[82] S. P. Hau–Riege et al., Phys. Rev. Lett. **98**, 145502 (2007).

[83] A. Föhlisch, M. Nagasono, M. Deppe, E. Suljoti, F. Hennies, A. Pietzsch, W. Wurth, Phys. Rev. A **76**, 13411 (2007).

[84] M. Meyer, D. Cubaynes, P. OKeeffe, H. Luna, P. Yeates, E. T. Kennedy, J. T. Costello, P. Orr, R. Taeb, A. Maquet, S. Düsterer, P. Radcliffe, H. Redlin, A. Azima, E. Plnjes, J. Feldhaus, Phys. Rev. A **74**, 011401 (2006).

[85] K. Tiedtke, J. Feldhaus, U. Hahn, U. Jastrow, T. Nunez, T. Tschentscher, S. V. Bobashev, A. A. Sorokin, J. B. Hastings, S. Möller, L. Cibik, A. Gottwald, A. Hoehl, U. Kroth, M. Krumrey, H. Schöppe, G. Ulm, M. Richter, J. Appl. Phys. **103**, 094511 (2008).

[86] K. Tiedtke, A. Azima, N. von Bargen, L. Bittner, S. Bonfigt, S. Düsterer, B. Faatz, U. Frühling, M. Gensch, Ch. Gerth, N. Guerassimova, U. Hahn, T. Hans, M. Hesse, K. Honkavaar, U. Jastrow, P. Juranic, S. Kapitzki, B. Keitel, T. Kracht, M. Kuhlmann, W. B. Li, M. Martins, T. Nunez, E. Plnjes, H. Redlin, E. L. Saldin, E. A. Schneidmiller, J. R. Schneider, S. Schreiber, N. Stojanovic, F. Tavella, S. Toleikis, R. Treusch, H. Weigelt, M. Wellhöfer, H. Wabnitz, M. V. Yurkov, J. Feldhaus, New Journal of Physics **11**, 023029 (2009).

[87] M. Richter, A. Gottwald, U. Kroth, A. A. Sorokin, S. V. Bobashev, L. A. Shmaenok, J. Feldhaus, Ch. Gerth, B. Steeg, K. Tiedtke, R. Treusch, Appl. Phys. Lett. **83**, 2970 (2003).

[88] A. Bytchkov, A. A. Fateev, J. Feldhaus, U. Hahn, M. Hesse, U. Jastrow, V. Kocharyan, N. I. Lebedev, E. A. Matyushevskiy, E. L. Saldin, E. A. Schneidmiller, A. V. Shabunov, K. P. Sytchev, K. Tiedtke, R. Treusch, M. V. Yurkov, Nucl. Instrum. Methods A **528**, 254 (2004).

[89] A. Pietzsch, Ph.D. thesis, Institut für Experimentalphysik (Universität Hamburg), 2008.

[90] M. Beye, private communication 2008.

[91] B. L. Henke, http://henke.lbl.gov/opticalconstants/mirror2.html.

[92] M. P. Kowalski, G. G. Fritz, R. G. Cruddace, A. E. Unzicker, N. Swanson , Applied Optics **25**, 2440 (1986).

[93] C. Thede, Diploma thesis, Institut für Experimentelle und Angewandte Physik (Universität Kiel), 2007.

[94] M. Beye, F. Sorgenfrei, W. Schlotter, W. Wurth, A. Föhlisch, Proc Natl Acad Sci USA **107(39)**, 16772 (2010).

[95] H. Meyer, private communication 2008.

[96] C. Gahl, A. Azima, M. Beye, M. Deppe, K. Döbrich, U. Hasslinger, F. Hennies, A. Melnikov, M. Nagasono, A. Pietzsch, M. Wolf, W. Wurth, A. Föhlisch, Nature Photonics **2**, 165 (2008).

[97] L. Kipp, private communication.

[98] http://tesla.desy.de/doocs/doocs.html.

[99] http://root.cern.ch.

[100] N. Guerassimova, private communication 2008.

[101] S. Collin, M. Merano, M. Gatri, S. Sonderegger, P. Renucci, J.–D. Ganiere, B. Deveaud, J. Appl. Phys. **98**, 94910 (2005).

[102] A. M. Michalik, J. E. Sipe, J. Appl. Phys. **99**, 54908 (2006).

[103] B. W. Reed, J. Appl. Phys. **100**, 34916 (2006).

[104] B. Qian, H. E. Elsayed-Alia, J. Appl. Phys. **91**, 462 (2001).

[105] B. J. Siwick, J. R. Dwyer, R. E. Jordan, R. J. Dwayne Miller, J. Appl. Phys. **92**, 1643 (2002).

[106] G. A. Massey, M. D. Jones, B. P. Plummer, J. Appl. Phys. **52**, 3780 (1981).

[107] T. Srinivasan–Rao, J. Fischer, T. Tsang, J. Appl. Phys. **69**, 3291 (1991).

[108] T. L. Gilton, J. P. Cowin, G. D. Kubiak, A. V. Hamza, J. Appl. Phys. **68**, 4802 (1990).

[109] D. M. Riffe, X. Y. Wang, M. C. Downer, D. L. Fisher, T. Tajiama, J. L. Erskine, R. M. More, J. Opt. Soc. Am. B **10**, 1424 (1993).

[110] P. Siffalovic, M. Drescher, U. Heinzmann, Europhys. Lett. **60**, 924 (2002).

[111] J. P. Long, B. S. Itchkawitz, M. N. Kabler, J. Opt. Soc. Am. B **13**, 201 (1996).

[112] G. W. E. Hairer, C. Lubich, Acta Numerica **12**, 399 (2003).

[113] L. Hernquist, ApJS **64**, 715 (1987).

[114] S. Hellmann, Diploma thesis, Institut für Experimentelle und Angewandte Physik (Universität Kiel), 2008.

[115] F. Reinert, G. Nicolay, S. Schmidt, D. Ehm, and S. Hüfner, Phys. Rev. B **63**, 115415 (2001).

[116] M. V. Ammosov, J. Opt. Soc. Am. B **8**, 2260 (1991).

[117] J. Bokor, R. Haight, R. H. Storz, J. Stark, R. R. Freeman, P. H. Bucksbaum, Phys. Rev. B **32**, 3669 (1985).

[118] R. Clauberg, A. Blacha, J. Appl. Phys. **65**, 4095 (1989).

[119] S. D. Kevan, in *Angle–resolved Photoemission: Theory and Current Applications* (Elsevier, Amsterdam, 1992).

[120] A. Damascelli, Z. Hussain, Z.–X. Shen, Rev. Mod. Phys. **75**, 473 (2003).

[121] E. Rotenberg, H. Koh, K. Rossnagel, H. W. Yeom, J. Schäfer, B. Krenzer, M. P. Rocha, and S. D. Kevan, Phys. Rev. Lett. **91**, 246404 (2003).

[122] J. D. Koralek, J. F. Douglas, N. C. Plumb, Z. Sun, A. V. Fedorov, M. M. Murnane, H. C. Kapteyn, S. T. Cundiff, Y. Aiura, K. Oka, H. Eisaki, D. S. Dessau, Phys. Rev. Lett. **96**, 017005 (2006).

[123] H. Petek, S. Ogawa, Prog. Surf. Sci. **56**, 239 (1997).

[124] M. Bauer, J. Phys. D **38**, (2005).

[125] G. Margaritondo, F. Cerrina, Nucl. Instrum. Meth. Phys. Res. A **291**, 26 (1990).

[126] M. Marsi, L. Casalis, L. Gregoratti, S. Günther, A. Kolmakov, J. Kovac, D. Lonza, M. Kiskinova, J. Electron Spectrosc. Relat. Phenom. **84**, 73 (1997).

[127] B. McNeil, Nature Photonics **2**, 522 (2008).

[128] E.L. Saldin, E.A. Schneidmiller, M.V. Yurkov, Opt. Commun. **148**, 383 (1998).

[129] E.L. Saldin, E.A. Schneidmiller, M.V. Yurkov, in *The Physics of Free Electron Lasers* (Springer, Berlin, 1999).

[130] J. Andruszkow et al., Phys. Rev. Lett. **85**, 3825 (2000).

[131] R. Haight, D. R. Peale, Rev. Sci. Instrum. **65**, 1853 (1994).

[132] P. Siffalovic, M. Drescher, M. Spieweck, T. Wiesenthal, Y. C. Lim, R. Weidner, A. Elizarov, U. Heinzmann, Rev. Sci. Instrum. **72**, 30 (2001).

[133] M. Bauer, C.–F. Lei, K. Read, R. Tobey, J. Gland, M. M. Murnane, H. C. Kapteyn, Phys. Rev. Lett. **87**, 025501 (2001).

[134] A. L. Cavalieri, N. Müller, Th. Uphues, V. S. Yakovlev, A. Baltuska, B. Horvath, B. Schmidt, L. Blümel, R. Holzwarth, S. Hendel, M. Drescher, U. Kleineberg, P. M. Echenique, R. Kienberger, F. Krausz, U. Heinzmann, Nature **449**, 1029 (2007).

[135] L. Miaja–Avila, G. Saathoff, S. Mathias, J. Yin, C. La–o–vorakiat, M. Bauer, M. Aeschlimann, M. M. Murnane, H. C. Kapteyn, Phys. Rev. Lett. **101**, 046101 (2008).

[136] K. Flöttmann, Astra users manual.

[137] M. Martins, M. Wellhöfer, J. T. Hoeft, W. Wurth, J. Feldhaus, R. Follath, Rev. Sci. Instrum. **77**, 115108 (2006).

[138] M. Boehme, Ph.D. thesis, Institut für Experimentelle und Angewandte Physik (Universität Kiel), 1998.

[139] M. Böhmisch, F. Burmeister, J. Boneberg, and P. Leiderer, Appl. Phys. Lett. **69**, 1882 (1996).

[140] B. Parkinson, J. Am. Chem. Soc. **112**, 7498 (1990).

[141] Th. Schimmel, H. Fuchs, S. Akari, K. Dransfeld, Appl. Phys. Lett. **58**, 1039 (1991).

[142] S. Akari, K. Möller, K. Dransfeld, Appl. Phys. Lett. **59**, 243 (1991).

[143] J. Boneberg, M. Lohrmann, M. Böhmisch, F. Burmeister, M. Lux–Steiner, P. Leiderer, Z. Phys. B **99**, 567 (1996).

[144] C. Enss, R.Winters, M. Reinermann, G. Weiss, S. Hunklinger, M. Lux–Steiner, Z. Phys. B **99**, 561 (1996).

[145] F. Flores, P. M. Echenique, R. H. Ritchie, Phys. Rev. B **34**, 2899 (1986).

[146] T. T. Tsong, in *Atom Probe Field Ion Microscopy* (Cambridge University, Cambridge, 1990).

[147] T. Ono, K. Hirose, J. Appl. Phys. **95**, 1568 (2004).

[148] T. Ono, T. Sasaki, J. Otsuka, K. Hirose, Surface Science **577**, 42 (2005).

[149] Z. A. Munir, T. Nguyen, J. Crystal Growth **57**, 449 (1982).

[150] S. Arrhenius, Z. Phys. Chem. **Neue Folge 4**, 226 (1889).

[151] J. J. Yeh, I. Lindau, At. Data Nucl. Data Tables **32**, 1 (1985).

[152] H. Cordes, R. Schmid–Fetzer, J. Alloys Comp. **216**, 197 (1995).

[153] S. Tanuma, C. J. Powell, D. R. Penn, Surf. Interf. Anal. **21**, 165 (1994).

[154] W. S. Fann, R. Storz, H. W. K. Tom, J. Bokor, Phys. Rev. B **46**, 13592 (1992).

[155] S. K. Sundaram, E. Mazur, Nature Materials **1**, 217 (2002).

[156] D. von der Linde, K. Sokolowski–Tinten, J. Bialkowski, Appl. Surf. Sci. **109/110**, 1 (1997).

[157] K. Sokolowski–Tinten, J. Bialkowski, A. Cavalleri, D. von der Linde, A. Oparin, J. Meyer-ter-Vehn, S. I. Anisimov, Phys. Rev. Lett. **81**, 224 (1998).

List of abbreviations

AFM	**a**tomic–**f**orce **m**icroscopy
ARPES	**a**ngle–**r**esolved **p**hotoelectron **s**pectroscopy
BESSY	**B**erliner **E**lektronen–**S**peicherring Gesellschaft fr **Sy**nchrotronstrahlung
BT	**b**eamline **t**ransmission
BZ	**B**rillouin **z**one
CCD	**c**harge–**c**oupled–**d**evice
CCDW	**c**ommensurate **c**harge–**d**ensity **w**ave
CDW	**c**harge–**d**ensity **w**ave
CFS	**c**onstant **f**inal state **s**pectroscopy
CIS	**c**onstant **i**nitial state **s**pectroscopy
DESY	**D**eutsches **E**lektronen–**Sy**nchrotron
DOOCS	**d**istributed **o**bject **c**ontrol **s**ystem
EDC	**e**nergy **d**istribution **c**urve
EOS	**e**lectro–**o**ptical **s**ampling
EUV	**e**xtreme **u**ltra**v**iolet
FEL	**f**ree–**e**lectron **l**aser
FLASH	**f**ree–electron **las**er in **H**amburg
FWHM	**f**ull **w**idth at **h**alf **m**aximum
GMD	**g**as–**m**onitor **d**etector
ICCDW	**inc**ommensurate **c**harge–**d**ensity **w**ave
IR	**i**nfra**r**ed
I–tube	**i**ntensity–**tube**
LEED	**l**ow **e**nergy **e**lectron **d**iffraction
LINAC	**Lin**ear **ac**celerator
MCP	**m**ulti–**c**hannel **p**late
NCCDW	**n**early **c**ommensurate **c**harge–**d**ensity **w**ave
PAD	**p**hotoelectron **a**ngular **d**istribution
PC	**p**ersonal **c**omputer
PE	**p**hoto**e**lectron
PES	**p**hoto**e**lectron **s**pectroscopy
PG2	**p**lane **g**rating monochromator beamline **2**
PLD	**p**eriodic **l**attice **d**istortion
RF	**r**adio **f**requency
SASE	**s**elf **a**mplified **s**pontaneous **e**mission
SC	**s**pace–**c**harge
SCE	**s**pace–**c**harge **e**ffect
SHG	**s**econd–**h**armonic **g**eneration
STM	**s**canning–**t**unneling **m**icroscopy
HHG	**h**igher–**h**armonic **g**eneration
ToF	**t**ime–**of**–**f**light

TRPES	**t**ime–**r**esolved **p**hoto**e**lectron **s**pectroscopy
TRXPS	**t**ime–**r**esolved **X**–ray **p**hotoelectron **s**pectroscopy
TMDC	**t**ransition **m**etal **d**ichal**c**ogenide
UHV	**u**ltra**h**igh **v**acuum
UV	**u**ltra**v**iolet
vdW	**v**an **d**er **W**aals
VUV	**v**acuum **u**ltra**v**iolet
XFEL	**X**–ray **f**ree–**e**lectron **l**aser
XPS	**X**–ray **p**hotoelectron **s**pectroscopy

List of publications

International journals

1. M. Kalläne, K. Rossnagel, M. Marczynski-Bühlow, L. Kipp, H. I. Starnberg, and S. E. Stoltz
   Metal cross–substitution in the misfit layer compound $(PbS)_{1.13}TaS_2$,
   Physical Review Letters **100**, 065502, (2008).

2. S. Hellmann, K. Rossnagel, M. Marczynski-Bühlow, and L. Kipp,
   Vacuum space–charge effects in solid–state photoemission,
   Phys. Rev. B **79**, 035402 (2009).

3. S. Hellmann, M. Beye, C. Sohrt, T. Rohwer, F. Sorgenfrei, H. Redlin, M. Kalläne, M. Marczynski-Bühlow, F. Hennies, M. Bauer, A. Föhlisch, L. Kipp, W. Wurth, and K. Rossnagel,
   Ultrafast melting of a charge-density wave in the Mott insulator $1T$–TaS_2,
   Physical Review Letters **105**, 187401, (2010).

4. K. Iino, L. Lozonschi, A. Metzner, M. Marczynski–Bühlow, J. Renner, J. Cremer, and G. Lutter,
   Tricuspid valved stent implantation: novel stent with a self-expandable super-absorbent polymer,
   Eur J Cardiothorac Surg. **40(2)**, 503, (2011).

5. T. Attmann, S. Pokorny, L. Lozonschi, A. Metzner, M. Marcynski–Bühlow, J. Schoettler, J. Cremer, and G. Lutter *Mitral valved stent implantation: An overview*,
   Minim. Invasive Ther. Allied Technol. **20(2)**, 78, (2011).

6. D. J. Rahn, E. Ludwig, J. Buck, F. Kronast, M. Marcynski–Bühlow, E. Kröger, L. Kipp, and K. Rossnagel,
   Laterally confined metal–to–insulator and quasi–two–dimensional-to-two–dimensional transition by focused Rb intercalation of $1T$–TaS_2,
   Phys. Rev. B **84**, 233105 (2011) .

7. S. Hellmann, C. Sohrt, M. Beye, F. Sorgenfrei, M. Marczynski–Bühlow, M. Kalläne, T. Rohwer, H. Redlin, F. Hennies, M. Bauer, A. Föhlisch, L. Kipp, W. Wurth, and K. Rossnagel,
   Time–resolved X–ray photoelectron spectroscopy at FLASH,
   New J. Phys., submitted.

8. M. Marczynski–Bühlow, M. Leester–Schädel, J. Cremer, G. Lutter, L. Lozonschi, T. Koeppel, and R. Bombien,
   Transcatheter aortic valve replacement: Transapical Resection of the Aortic Valve in vivo,
   Eur J Cardiothorac Surg., submitted.

Research reports

1. M. Marczynski, M. Kalläne, S. Harm, K. Rossnagel, L. Kipp,
A multichannel detection photoemission experiment,
HASYLAB Annual Report 2004.

2. M. Marczynski, M. Kalläne, T. Riedel, S. Harm, K. Rossnagel, L. Kipp,
Angle resolved photoemission at the VUV–FEL,
HASYLAB Annual Report 2005.

3. M. Marczynski, M. Helle, K. Rossnagel, P. Stojanov, A. Tadich, E. Huwald, N. Janke–Gilman, R. Leckey, J. Riley, L. Kipp,
Valence Band Structure of Intercalated Layered Transition Metal Dichalcogenides,
BESSY Annual Report 2005.

4. M. Kalläne, D. Rahn, S. Harm, J. Buck, M. Marczynski–Bühlow, T. Riedel, K. Rossnagel, L. Kipp,
First spatially resolved photoemission measurements at BW3 using reflective photon sieves,
HASYLAB Annual Report 2006.

5. M. Marczynski-Büuhlow, J. Buck, K. Rossnagel, N. Janke–Gilman, A. Walter, L. Broekman, J. Riley, L. Kipp,
Matrix–Element Effects in Valence Band Photoemission on Fe_xTiS_2 *Using Circularly Polarized Light*,
BESSY Annual Report 2006.

6. D. Rahn, M. Marczynski–Bühlow, J. Buck, T. Riedel, K. Rossnagel, L. Kipp,
Photoelectron spectroscopy on inhomogeneously Rb adsorbed $1T$–TaS_2,
HASYLAB Annual Report 2007.

7. M. Marczynski–Bühlow, M. Kalläne, S. Hellmann, S. Lang, C. Thede, T. Riedel, S. Harm, K. Rossnagel, L. Kipp,
Core–level Spectroscopy at FLASH and Investigation of Space Charge Effects,
BESSY Annual Report 2007.

List of presentations

National conferences

1. M. Marczynski, K. Rossnagel, M. Kalläne, E.E. Krasovskii, M. Skibowski, W. Schattke, L. Kipp,
High energy conduction band states in layered materials,
DPG spring meeting, Regensburg 2004, poster presentation.

2. M. Helle, M. Marczynski, M. Kalläne, S. Harm, K. Rossnagel, L. Kipp,
A multichannel detection photoemission experiment,
DPG spring meeting, Berlin 2005, poster presentation.

3. M. Marczynski, M. Kalläene, T. Riedel, S. Harm, K. Rossnagel, L. Kipp,
   Angle Resolved Photoemission Spectroscopy at VUV-FEL,
   DPG spring meeting, Dresden 2006, poster presentation.

4. M. Helle, M. Frank, M. Marczynski, K. Rossnagel, A. Tadich, P. Stojanov, E. Huwald, N. Janke–Gilman, J. Riley, R. Leckey, L. Kipp,
   Electronic structure of pristine and Rb adsorbed VSe_2,
   DPG spring meeting, Dresden 2006, poster presentation.

5. M. Marczynski, M. Kalläne, T. Riedel, S. Harm, K. Rossnagel, L. Kipp,
   Angle Resolved Photoemission Spectroscopy at VUV–FEL,
   Deutsche Tagung für Forschung mit Synchrotronstrahlung, Neutronen und Ionenstrahlen an Großgeräten, Hamburg 2006, poster presentation.

6. M. Kalläne, T. Riedel, D. Rahn, S. Harm, K. Roßnagel, J. Buck, M. Marczynski–Bühlow, C. Thede, L. Kipp
   Spatially resolved photoemission measurements using reflective photon sieves,
   DPG spring meeting, Regensburg 2007, poster presentation.

7. M. Marczynski–Bühlow, S. Lang, J. Buck, K. Rossnagel, N. Janke–Gilman, A. Walter, J. Riley, L. Kipp,
   Matrix–Element Effects in Valence–Band Photoemission of Fe_xTiS_2 *Using Circularly Polarized Light*,
   DPG spring meeting, Regensburg 2007, poster presentation.

8. D. Rahn, H. Starnberg, M. Marczynski–Bühlow, T. Riedel, J. Buck, K. Rossnagel, L. Kipp,
   Photoelectron microscopy of the Mott–Hubbard transition at inhomogeneously Rb adsorbed 1T–TaS_2 *surfaces*,
   DPG spring meeting, Berlin 2008, oral presentation by D. Rahn.

9. M. Marczynski–Bühlow, M. Kalläne, S. Hellmann, S. Lang, C. Thede, T. Riedel, S. Harm, K. Rossnagel, L. Kipp,
   Photoelectron Spectroscopy at FLASH: Limits and Perspectives,
   DPG spring meeting, Berlin 2008, poster presentation.

10. M. Marczynski–Bühlow, M. Kalläne, S. Hellmann, S. Lang, C. Thede, T. Riedel, S. Harm, K. Rossnagel, L. Kipp,
    Space–Charge Effects in Photoelectron Spectroscopy at FLASH,
    DPG spring meeting, Berlin 2008, oral presentation.

11. M. Kalläne, H. Starnberg, K. Rossnagel, M. Marczynski-Bühlow, S. Stoltz, L. Kipp,
    Metal cross–substitution in the misfit layer compound $(PbS)_{1.13}TaS_2$,
    DPG spring meeting, Berlin 2008, oral presentation by M. Kalläne.

12. M. Marczynski–Bühlow, G. Lutter, T. Hümme, L. Lozonschi, J. Cremer, R. Bombien,
    Transkatheter Herzklappen–Ersatz: Resektion und Herzklappenstent–Implantation am schlagenden Herzen,
    Experimentelle Radiologie 2010, oral presentation.

13. S. Pokorny, L. Lozonschi, T. Hümme, A. Metzner, M. Marczynski–Bühlow, J. Cremer, G. Lutter,
    Transapical mitral valved stent implantation: an off-pump technique,
    Experimentelle Radiologie 2010, oral presentation by S. Pokorny.

International conferences

1. M. Marczynski-Bühlow, M. Kalläne, K. Rossnagel, L. Kipp, T. Riedel, S. Harm,
   Photoelectron spectroscopy at FLASH,
   15^{th} International Conference on Vacuum Ultraviolet Radiation Physics, Berlin 2007, poster presentation.

Acknowledgement

First, I would like to thank my thesis advisor Prof. Dr. Lutz Kipp for his generous support and advice throughout the preparation of this thesis. I am very grateful for the opportunity to work in his well–organized and productive group, for his encouragement to persue my own ideas and the many fruitful discussions that contributed to this thesis.

My special thanks go to Dr. Kai Rossnagel for the encouraging and productive discussions as well as his expert knowledge of photoelectron spectroscopy methods. The development of this thesis would not have been possible without his tremedous expericence and expert knowledge in the field of photoemission.

I am deeply grateful to Dr. Matthias Kalläne, who helped to establish the first photoemission experiments at FLASH. His careful reading of this thesis, the uncountable beamtimes at the free–electron, and the many productive discussions in the field of photoemission have been invaluable.

I would like to thank Dipl. Phys. Stefan Hellmann and Dipl. Phys. Christian Sohrt for their great teamwork during the first intensity dependent as well as time–resolved photoemission beamtimes at FLASH, and the fruitful discussions in order to understand space–charge effects in PES.

Furthermore, I would like to thank Dipl. Ing. Tim Riedel for his tremendous ideas in the construction of the complex mechanical equipment indispensable to the realization of PES experiments at FLASH. I also thank him for the good atmosphere and inspriring discussions we had while sharing an office during most the time I was working on this thesis.

I am grateful to Dr. Sönke Harm who aroused my interest in photoemission spectroscopy, guided my way into Prof. Kipp's group and supervised me during my diploma thesis. His continuous advice in all technial matters were invaluable.

I am indebted to my fellow PhD studens of the Kiel surface science group. They accompanied me during most of this thesis and shared many memorable beamtimes at the the different synchrotron radiation sources.

For the great support with all kinds of electronics and mechanics questions, I would like to thank Manfred Stiller, Jörg Neubauer and Wilfried Krüger.

I would like to thank my parents for their support throughout my studies. From secondary school until today, they have given me the opportunity to focus on my interests in physics.

Shortly before submitting this thesis, my son Jonathan was born. The anticipation of his birth was a powerful motivation for me during the final months of this project.

Most of all, I would like to thank my wife So-Nyeo for her constant support, encouragement and tolerance of my work. To her, I dedicate this thesis.

Lebenslauf

	Martin Marczynski–Bühlow geboren am 09. Februar 1979 in Kiel deutsche Staatsangehörigkeit
1985 – 1989	Grundschule in Kiel
1989 – 1998	Gymnasium in Kiel
Juni 1998	Allgemeine Hochschulreife
1998 – 1999	Zivildienst
1999 – 2005	Studium der Physik an der Christian–Albrechts–Universitt zu Kiel
Oktober 2001	Vordiplom in Physik
Januar 2005	Diplom in Physik Diplomarbeit bei Prof. Dr. Lutz Kipp zum Thema: *Inbetriebnahme eines Experimentes für winkelaufgelöste Photoemission mit Vielkanaldetektion*
Februar 2005	Beginn der Dissertation bei Prof. Dr. Lutz Kipp
2005 – 2009	wissenschaftlicher Angestellter am Institut für Experimentelle und Angewandte Physik der Universitt Kiel
seit Juni 2009	wissenschaftlicher Angestellter in der Klinik für Herz– und Gefäßchirurgie des Uniklinikums Kiel

Eidesstattliche Erklärung

Hiermit erkläre ich an Eides Statt, daß ich diese Arbeit selbständig unter der Beratung meiner wissenschaftlichen Lehrer und nur mit den angegebenen Hilfsmitteln erstellt habe.
Diese Arbeit wurde weder ganz noch in Teilen an anderer Stelle im Rahmen eines Prüfungsverfahrens vorgelegt.
Frühere Promotionsversuche wurden von mir nicht vorgenommen.
Diese Arbeit ist unter Einhaltung der Regeln guter wissenschaftlicher Praxis der Deutschen Forschungsgemeinschaft entstanden.

Kiel, den